

SEARCH FOR PAIR-PRODUCED RESONANCES  
DECAYING TO TOP QUARKS AND JETS IN  
PROTON-PROTON COLLISIONS AT 8 TEV WITH  
THE CMS DETECTOR AT THE LHC

A Dissertation  
Presented to the Faculty of the Graduate School  
of Cornell University  
in Partial Fulfillment of the Requirements for the Degree of  
Doctor of Philosophy

by  
Gala Nicolas Kaufman  
August 2014

© 2014 Gala Nicolas Kaufman

ALL RIGHTS RESERVED

SEARCH FOR PAIR-PRODUCED RESONANCES DECAYING TO TOP  
QUARKS AND JETS IN PROTON-PROTON COLLISIONS AT 8 TEV WITH  
THE CMS DETECTOR AT THE LHC

Gala Nicolas Kaufman, Ph.D.

Cornell University 2014

We present a search for pair production of new physics resonances decaying into a top quark and a light parton in final states with two leptons, interpreting the results in the context of an  $R$ -parity violating supersymmetric model. We use  $19.5 \text{ fb}^{-1}$  of data collected by the CMS experiment at the LHC from proton-proton collisions at  $\sqrt{s} = 8 \text{ TeV}$  in 2012. The experimental signature consists of two leptons ( $e$  or  $\mu$ ), two jets identified as originating from the decay of a  $b$  quark, and two jets identified as coming from light flavor quarks or gluons. We reconstruct and analyze potential resonant decays. The dominant standard model background is top quark pair production with additional jets from initial- or final-state radiation. We perform an extended unbinned maximum likelihood fit to the transverse momenta of the two leading light jets and the reconstructed resonance mass. The observation is consistent with the standard model expectation, and we set upper limits on the signal cross section for  $R$ -parity violating bottom squarks with masses between 250 and 600 GeV. We exclude  $R$ -parity violating bottom squark pair production at the 95% confidence level between 250 GeV and 326 GeV.

## BIOGRAPHICAL SKETCH

Gala Nicolas Kaufman attended the Lycée Condorcet in Paris, France and obtained a Baccalauréat Scientifique in 2005. She spent an additional two years there in “prépa” (Classes Préparatoires aux Grandes Écoles), studying physics, chemistry, and mathematics. Gala then attended Université Paris VII – Diderot, from which she received a B.S. in physics in 2008. After beginning a M.S. in Paris, she moved to Ithaca, NY to pursue a graduate degree in physics at Cornell.

To new physics, whatever it may be.

## ACKNOWLEDGEMENTS

The work resulting in this thesis has been a group effort, and I owe many thanks to many different people.

I am profoundly grateful to my advisor, Julia Thom, for introducing me to physics at the CMS experiment. You have been an exceptional instructor and mentor, and your support has been essential to my success as a graduate student. I am immensely fortunate to have worked closely with such an amazing scientist and person.

Thank you also to my committee members, Lawrence Gibbons and Maxim Perelstein. Through classes and other interactions with you I have learned a great deal.

Across the years and research projects I was extremely lucky to work with Luke Winstrom, who has been an invaluable teacher, mentor, and friend. Your patience and willingness to answer every single one of my questions, physics-related and otherwise, are incredibly appreciated and valued. Thank you for being a fantastic collaborator.

I must also express my utmost appreciation for the numerous opportunities I have had to learn from the rest of the Cornell CMS group. Thank you all for your kindness and willingness to answer my questions.

Josh Thompson, thank you for being an excellent guide through the intricacies of data processing and analysis. I tremendously benefited from, and enjoyed, discussions with you. I am also extremely grateful to you and Evonne Leeper for being such wonderful hosts during my visits to CERN.

Thank you Yao Weng for introducing me to data analysis in CMS, and Ben Kreis and Don Teo for your help in understanding the RA2b analysis and framework.

Thank you to CERN, the LHC, and CMS for their momentous achievements in the design, construction, and operation of an exciting and ground-breaking experiment. I am deeply indebted to the countless people who made this work possible.

I am thankful as well to the National Science Foundation for providing funding support during my graduate career.

The Cornell Physics Department has been a great place to pursue a graduate degree. Thank you especially to Kacey Bray and Deb Hatfield for their administrative help.

Throughout graduate school I was lucky to be surrounded by amazing friends, whose support has been instrumental to my success.

Zach Lamberty, my constant, thank you for understanding me to such an extraordinary degree, for listening to me in good times and in bad, and for sharing (but mostly not) my taste in movies. Without your wisdom and unfailing support I would not have made it through grad school.

Thank you Sergei Dyda for always making me laugh while at the same time providing such profound insight, and also for indulging my taste in hamburgers, pizza, and ice cream – sorry about your diet. You are a truly unique individual and I am so glad we met.

Dusty Madison and Jenn Boggs, I am incredibly privileged to be your friend. Thank you Dusty for expanding my literary horizons, and Jenn for exerting a much-needed outside influence on our group of physicist friends. And thank you both for introducing me to your awesome cats.

Mike Saelim, thank you for complementing my experimentalist's point of view with your theoretical one. I am grateful for the many discussions we had, and have learned a lot from you.

Thank you Julia Mundy for helping me to achieve a balance between work and home. You have been an outstanding roommate, co-chef, and couch buddy, as well as a great source of advice and support. Thank you also to your family for welcoming me and providing such a wonderful home away from home.

Finally, thank you Mom, merci Papa. Your love, unwavering support, and continued belief, spanning an ocean, that I could achieve anything I set out to do, bring me here today. And, last but not least, thank you to my sister, Naomi, for being a constant source of encouragement, inspiration, motivation, entertainment, and awe.

## TABLE OF CONTENTS

Biographical Sketch . . . . .	iii
Dedication . . . . .	iv
Acknowledgements . . . . .	v
Table of Contents . . . . .	viii
List of Tables . . . . .	xi
List of Figures . . . . .	xii
<b>1 Theoretical Framework</b>	<b>1</b>
1.1 Motivation . . . . .	1
1.2 The standard model Lagrangian . . . . .	3
1.2.1 Gauge and fermion fields . . . . .	3
1.2.2 The Higgs field . . . . .	5
1.2.3 Gauge boson masses . . . . .	8
1.2.4 Fermion masses . . . . .	9
1.2.5 Limitations of the standard model . . . . .	11
1.2.6 Physics beyond the standard model: supersymmetry . . . . .	12
1.3 Components of a basic SUSY model . . . . .	14
1.3.1 Chiral and gauge fields . . . . .	14
1.3.2 Free supermultiplets . . . . .	16
1.3.3 Interaction terms . . . . .	18
1.3.4 SUSY model-building . . . . .	22
1.3.5 Soft SUSY breaking . . . . .	23
1.4 The Minimal Supersymmetric Standard Model . . . . .	25
1.4.1 Particle content . . . . .	25
1.4.2 Superpotential and interactions . . . . .	27
1.4.3 <i>R</i> -parity . . . . .	29
1.4.4 Naturalness . . . . .	30
1.4.5 Experimental signature . . . . .	31
1.5 <i>R</i> -parity violating SUSY with Minimal Flavor Violation . . . . .	33
1.5.1 Superpotential . . . . .	33
1.5.2 BNV vertices and coupling strengths . . . . .	34
1.5.3 Phenomenology . . . . .	35
<b>2 Accelerator and Detector</b>	<b>37</b>
2.1 The Large Hadron Collider . . . . .	37
2.1.1 Machine layout and operation . . . . .	38
2.1.2 Performance . . . . .	41
2.2 The Compact Muon Solenoid . . . . .	42
2.2.1 Tracking systems . . . . .	44
2.2.2 Calorimeter systems . . . . .	49
2.2.3 Superconducting solenoid . . . . .	57
2.2.4 Muon systems . . . . .	58
2.2.5 Trigger and data acquisition . . . . .	64

<b>3 Event Reconstruction</b>	<b>67</b>
3.1 Particle Flow . . . . .	68
3.2 Tracks and vertices . . . . .	69
3.2.1 Tracks . . . . .	69
3.2.2 Vertices . . . . .	71
3.3 Electrons . . . . .	72
3.4 Muons . . . . .	74
3.5 Jets and missing transverse energy . . . . .	76
3.5.1 Jets . . . . .	77
3.5.2 Missing transverse energy . . . . .	80
3.6 b-tagging . . . . .	80
<b>4 Analysis</b>	<b>85</b>
4.1 Introduction . . . . .	85
4.1.1 Motivation . . . . .	85
4.1.2 Analysis strategy . . . . .	86
4.2 Data and simulation samples . . . . .	88
4.2.1 Data . . . . .	88
4.2.2 Simulation . . . . .	89
4.3 Selections . . . . .	94
4.3.1 Object definitions . . . . .	94
4.3.2 Event selection . . . . .	97
4.3.3 Monte Carlo corrections . . . . .	98
4.4 Signal and background discrimination . . . . .	100
4.4.1 Light jet $p_T$ spectrum . . . . .	100
4.4.2 Resonance reconstruction . . . . .	110
4.5 Systematic uncertainties . . . . .	122
4.5.1 Background . . . . .	122
4.5.2 Signal . . . . .	123
4.6 Statistical model . . . . .	125
4.6.1 Background probability density function . . . . .	126
4.6.2 Signal probability density function . . . . .	127
4.6.3 Incorporating systematic uncertainties . . . . .	127
4.6.4 Signal plus background model . . . . .	128
4.6.5 Constructing confidence intervals . . . . .	129
4.7 Results and interpretation . . . . .	131
<b>5 Conclusion</b>	<b>140</b>
<b>A Object Reconstruction in Collider Events With Top Quarks</b>	<b>142</b>
A.1 Introduction . . . . .	142
A.1.1 Motivation . . . . .	142
A.1.2 Outline of the strategy . . . . .	143
A.2 Details of the algorithm . . . . .	144

A.2.1	Neutrino ellipse construction . . . . .	144
A.2.2	Light jet minimization . . . . .	149
A.2.3	Per-event $\chi^2$ minimization . . . . .	159
A.3	Results in simulation . . . . .	162
A.4	Conclusions and outlook . . . . .	171
	<b>Bibliography</b>	<b>172</b>

## LIST OF TABLES

1.1	Chiral Standard Model fermion fields and their quantum numbers.	5
1.2	Fermion and gauge fields of the Minimal Supersymmetric Standard Model and their quantum numbers. . . . .	26
2.1	Some LHC machine parameters and their values in 2012, compared to the design specifications. . . . .	42
4.1	Dataset names and integrated luminosities. . . . .	90
4.2	Simulation samples of SM background processes used for comparisons to data. . . . .	93
4.3	Efficiency of the mass reconstruction method, with and without integration over jet resolution (resampling procedure), and ratio of efficiencies, in signal simulation for different mass points. The efficiency in $t\bar{t}$ simulation is given for comparison. . . . .	117
4.4	Relative systematic uncertainty on the signal selection efficiency broken down by source of signal systematic uncertainty in the signal simulation of a 350 GeV $\tilde{b}$ squark. . . . .	126
4.5	Expected and observed 95% CL upper limits on the pair production cross section of $\tilde{b}$ squarks decaying to a top quark and light quark, as a function of the squark mass. . . . .	132

## LIST OF FIGURES

1.1	Leading order Feynman diagrams for $R$ -parity violating bottom squark pair production. . . . .	2
1.2	Distribution of the four-lepton invariant mass, in LHC Run I data and simulation, for the $H \rightarrow ZZ^* \rightarrow 4\ell$ channel. Left: ATLAS result; right: CMS result. . . . .	8
1.3	One-loop quantum corrections to the Higgs squared mass parameter $m_H^2$ , due to (a) a Dirac fermion $f$ , and (b) a scalar $S$ . . . . .	13
1.4	Left: summary of CMS limits on gluino pair production, with the gluino decaying to top anti-top neutralino, in the $m_{\tilde{g}} - m_{\text{LSP}}$ plane. Right: summary of CMS limits on stop squark pair production in the $m_{\tilde{t}} - m_{\text{LSP}}$ plane. . . . .	32
2.1	Schematic view, not to scale, of the Large Hadron Collider and accelerator complex at CERN. The different LHC experiments, ALICE, ATLAS, CMS, and LHCb, are denoted by black points around the circumference. . . . .	38
2.2	Layout of the CMS detector, showing the location of the different sub-detectors. . . . .	44
2.3	A view of the CMS tracking systems in the $r - z$ plane. These consist of the pixel detector, tracker inner and outer barrels (TIB and TOB), tracker inner disks (TID), and tracker endcaps (TEC). . . . .	45
2.4	Perspective view of the CMS pixel detector, the innermost tracking system. . . . .	46
2.5	Layout of one quarter of the CMS silicon microstrip tracker in the $r - z$ plane. . . . .	48
2.6	View of one quarter of the CMS electromagnetic calorimeter (ECAL) in the $r - z$ plane. . . . .	50
2.7	Layout of one quarter of the CMS hadronic calorimeter (HCAL) in the $r - z$ plane. . . . .	54
2.8	Layout of one quarter of the CMS muon systems: drift tubes (DT), cathode strip chambers (CSC), and resistive plate chambers (RPC), in the $r - z$ plane. . . . .	59
3.1	Electron reconstruction efficiency in data (black points) and simulation (blue points) in different super-cluster $\eta$ regions as a function of super-cluster $E_T$ . The bottom panel shows the corresponding data-to-simulation scale factors. The blue shaded area represents the total systematic uncertainty on the prediction in simulation. Left: $0 <  \eta  < 0.8$ . Right: $0.8 <  \eta  < 1.4442$ . . . . .	74
3.2	Reconstruction and identification efficiency of Particle Flow muons with a reconstructed tracker track in different $\eta$ ranges in data (black points) and simulation (red squares) as a function of muon $p_T$ . Left: $0 <  \eta  < 1.2$ . Right: $1.2 <  \eta  < 2.4$ . . . . .	76

3.3	Resolution on the transverse momentum of Particle Flow jets in data (black points) compared to the true resolution in simulation (red dashed line) and the resolution in simulation after applying a data-to-simulation correction factor (red line) in different $\eta$ ranges as a function of jet $p_T$ . Left: $0 <  \eta  < 0.5$ . Right: $1 <  \eta  < 1.5$ . . . . .	79
3.4	Missing transverse energy resolution, assuming a Gaussian distribution, as a function of the scalar sum over Particle Flow particles of transverse energies, for different $E_T^{\text{miss}}$ reconstruction algorithms. The blue points show the results for the PF algorithm in data while the blue line corresponds to the performance of the PF algorithm in simulation. . . . .	81
3.5	Efficiency to correctly identify b-quark jets with the medium working point of the Combined Secondary Vertex algorithm. Data are shown in red and simulation results in black. The bottom panel shows the corresponding data-to-simulation correction factors, with the shaded area representing the total statistical and systematic uncertainties and the dashed line showing the statistical uncertainty on the average scale factor values. . . . .	84
4.1	Leading order Feynman diagram for $R$ -parity violating sbottom squark pair production. . . . .	86
4.2	Variables used for discriminating signal from background in the search for $\tilde{b}$ squark pairs. Top row: transverse momentum of the leading (left) and second-leading (right) light flavor jets. Bottom: reconstructed $\tilde{b}$ resonance mass. . . . .	87
4.3	Leading-order Feynman diagrams for SM top quark pair production at a proton-proton collider, in association with an additional radiated jet. Top: initial-state radiation (ISR). Bottom: final-state radiation (FSR). . . . .	92
4.4	Distribution of the vertex multiplicity for vertices satisfying the selection requirements described in Section 4.3.1, in data and SM MC simulation. Left: before reweighting of the SM MC to match the distribution of vertex multiplicity in data. Right: after reweighting. . . . .	99
4.5	Light jet $p_T$ distributions in SM simulation (left) and the fit to SM simulation (right) in events where both light jets have $p_T$ above 50 GeV, shown in two dimensions. The distribution defined in Eq. 4.1 is used to fit the two-dimensional light jet $p_T$ shape. The same logarithmic $z$ scale is used in both plots. . . . .	103

4.6	Fit to the leading and second leading light jet $p_T$ spectra in SM simulation, in events where both light jets have $p_T$ below 50 GeV). The distribution defined in Eq. 4.1 is used to fit the two-dimensional light jet $p_T$ shape. The fit components are shown in pink, green, and blue, and the full fit function in red. The left (right) panel shows the $p_T$ of the leading (second leading) light jet. Top: linear scale; center: logarithmic scale; bottom: pull distribution. . . . .	104
4.7	Fit to the leading and second leading light jet $p_T$ spectra in SM simulation, in events where both light jets have $p_T$ above 50 GeV). The distribution defined in Eq. 4.1 is used to fit the two-dimensional light jet $p_T$ shape. The fit components are shown in pink, green, and blue, and the full fit function in red. The left (right) panel shows the $p_T$ of the leading (second leading) light jet. Top: linear scale; center: logarithmic scale; bottom: pull distribution. . . . .	105
4.8	Results of light jet fit to toy samples of the SM simulation. Left: yield predicted by the fit. Center: true yield in the toy sample. Right: difference of the two. From top to bottom, plots of the CR, SR1, SR2, and SR3 selections. . . . .	107
4.9	Two-dimensional light jet $p_T$ distributions for (left) the background-only hypothesis fit to data, and (right) the $\tilde{b}$ signal with a mass of 350 GeV. The diagonal line emphasizes the ordering of the jets by $p_T$ . . . . .	108
4.10	Light jet $p_T$ distributions in data with results of the background-only fit to data overlaid. The line represents the fitted function and the points represent the data. The ratio of the data to the fitted function is also shown. The top row shows the (left) leading light jet distribution and (right) second leading light jet distribution. The bottom row is restricted to events with second leading light jet $p_T > 50$ GeV. . . . .	109
4.11	Efficiency, after all kinematic selections defined in Section 4.3.2 have been applied, of reconstructing $\tilde{b}$ pair candidates. Top row: before (left) and after (right) the jet resampling technique has been applied. Bottom row: ratio of efficiencies with and without jet resampling. . . . .	115
4.12	Reconstructed resonance mass spectrum after full event selection in simulated $t\bar{t}$ (top left) and signal events for $\tilde{b}$ particle masses of 300 GeV (top right), 450 GeV (bottom left), and 600 GeV (bottom right). The blue histogram corresponds to events for which a real neutrino solution exists without having to sample over jet resolutions, and the red histogram represents events for which the sampling method was applied. Both histograms are normalized to unit area. . . . .	116

4.13	Reconstructed invariant mass $M_{t,\text{jet}}$ distribution in data with results of the background-only fit to data overlaid. The fitted function is the sum of a gamma distribution and a log-normal distribution that are forced to peak at the same value. The line represents this fitted function and the points represent the data. The ratio of the data to the fitted function is also shown. Top left: second leading jet $p_T$ between 30 GeV and 50 GeV. Top right: second leading jet $p_T$ between 50 GeV and 80 GeV. Bottom left: second leading jet $p_T$ between 80 GeV and 110 GeV. Bottom right: second leading jet $p_T$ greater than 110 GeV. . . . .	119
4.14	Reconstructed invariant mass $M_{t,\text{jet}}$ distribution in simulated signal events with $\tilde{b}$ squark mass of 300 GeV (right) and 600 GeV (left). Events are categorized using Monte Carlo truth to determine whether the b-quark jets and leptons have been correctly (red) or incorrectly (blue) paired in reconstructing the top quark candidates. Uncertainties are statistical only. Top: second leading light jet $p_T$ between 50 and 80 GeV (SR1). Middle: second leading light jet $p_T$ between 80 and 110 GeV (SR2). Bottom: second leading light jet $p_T$ above 110 GeV (SR3). . . . .	120
4.15	Signal selection efficiency and relative systematic uncertainty in the efficiency in each lepton flavor channel for the $\tilde{b}$ signal model, as a function of $\tilde{b}$ mass. This neglects correlations between the efficiencies, which are taken into account in the full analysis. Left: $e\mu$ channel, center: $ee$ channel, right: $\mu\mu$ channel. . . . .	125
4.16	Observed and expected 95% CL upper limits on the production cross section of $\tilde{b}$ squark pairs as a function of squark mass. . . . .	133
4.17	Reconstructed invariant mass distributions for results of the likelihood maximization with signal cross section set to the 350 GeV $\tilde{b}$ upper limit. The solid line shows the fitted function, the dashed line shows the signal component, and the points show the data. From left to right, these are for the CR, SR1, SR2, and SR3 regions. . . . .	134
4.18	Leading light jet $p_T$ distributions for results of the likelihood maximization with signal cross section set to the 350 GeV $\tilde{b}$ upper limit. The solid line shows the fitted function, the dashed line shows the signal component, and the points show the data. From left to right, these are for the CR, SR1, SR2, and SR3 regions. . . . .	135
4.19	Second leading light jet $p_T$ distributions for results of the likelihood maximization with signal cross section set to the 350 GeV $\tilde{b}$ upper limit. The solid line shows the fitted function, the dashed line shows the signal component, and the points show the data. From left to right, these are for the CR, SR1, SR2, and SR3 regions. . . . .	136

4.20	Distribution of p-values from the results of the scan over signal cross section hypotheses for the pair production of 350 GeV $\tilde{b}$ squarks. The vertical axis shows the fraction of toys with a test statistic (the profile likelihood ratio) value greater than that observed in data, as a function of the cross section hypothesis. Black points show the results for toys generated with the signal-plus-background hypothesis, while the dashed line shows results for toys generated using the background-only hypothesis. The green (yellow) band represents the fraction of background-only toys with a best-fit signal cross section within $\pm 1$ (2) standard deviations of the median value of the cross section corresponding to the global maximum of the likelihood, evaluated on the set of toys generated with the background-only hypothesis. The observed (expected) upper limit on the cross section for this mass point is found as the intersection of the observed (expected) curve with the red horizontal line at 5%, corresponding to a 95% CL. . . . .	137
4.21	Histogram of the signal cross section for the pair production of 350 GeV $\tilde{b}$ squarks corresponding to the global maximum of the likelihood evaluated on the set of toys generated with the background-only hypothesis. The horizontal axis corresponds to the signal cross section and the vertical axis shows the number of toys. The expected upper limit for this mass point is the median value in the histogram. The 68% (95%) CL band on the expected limit is determined by calculating the values of the best-fit signal cross section at which the fraction of toys below and above the median value corresponds to $\pm 1$ (2) standard deviations. . . . .	138
4.22	Profile likelihood ratio distributions for pseudo-data toy experiments in each signal strength scan point for the 350 GeV $\tilde{b}$ squark model. Top left scan point corresponds to a cross section of zero and increases from left to right and top to bottom, with the bottom right being the maximum cross section. In red is the test statistic distribution constructed from toys generated using the signal-plus-background hypothesis and in blue is the distribution from toys generated with the background-only hypothesis. The vertical black line marks the value of the profile likelihood ratio evaluated in data for the particular signal strength hypothesis. . . . .	139
A.1	Minimum per-event $\chi^2$ distribution in simulated top quark pair events. The blue (red) line corresponds to events in which the b-quark jets and leptons are correctly (incorrectly) paired. Left: linear scale. Right: logarithmic scale. . . . .	163

A.2	Distribution of the difference between the corrected and generated neutrino $p_T$ , normalized to the generated neutrino $p_T$ . Left: neutrinos; right: anti-neutrinos. . . . .	164
A.3	Distribution of the angular distance between the corrected and generated neutrinos. Left: neutrinos; right: anti-neutrinos. . . . .	165
A.4	Distribution of the difference between the corrected and generated $W^\pm$ boson $p_T$ , normalized to the generated $W^\pm$ boson $p_T$ . Left: $W^+$ bosons; right: $W^-$ bosons. . . . .	165
A.5	Distribution of the difference between the corrected and generated $W^\pm$ boson masses, normalized to the generated $W^\pm$ boson mass. Left: $W^+$ bosons; right: $W^-$ bosons. . . . .	166
A.6	Distribution of the angular distance between the corrected and generated $W^\pm$ bosons. Left: $W^+$ bosons; right: $W^-$ bosons. . . . .	166
A.7	Distribution of the difference between the corrected and generated top quark $p_T$ , normalized to the generated top quark $p_T$ . Left: top quarks; right: anti-top quarks. . . . .	167
A.8	Distribution of the difference between the corrected and generated top quark masses, normalized to the generated top quark mass. Left: top quarks; right: anti-top quarks. . . . .	167
A.9	Distribution of the angular distance between the corrected and generated top quarks. Left: top quarks; right: anti-top quarks. . . . .	168
A.10	Distribution of the difference between the corrected and generated bottom quark $p_T$ , normalized to the generated bottom quark $p_T$ . Left: bottom quarks; right: anti-bottom quarks. . . . .	168
A.11	Distribution of the angular distance between the corrected and generated bottom quarks. Left: bottom quarks; right: anti-bottom quarks. . . . .	169
A.12	Distribution of the difference between the corrected and generated light parton $p_x$ , normalized to the generated light parton $p_x$ . Left: first generated light partons; right: second generated light partons. . . . .	169
A.13	Distribution of the difference between the corrected and generated light parton $p_y$ , normalized to the generated light parton $p_y$ . Left: first generated light partons; right: second generated light partons. . . . .	170

# CHAPTER 1

## THEORETICAL FRAMEWORK

### 1.1 Motivation

The subject of this thesis is a search for pair-produced new physics resonances that decay to a top quark and light parton. We use data collected in 2012 by the Compact Muon Solenoid (CMS) detector, a general-purpose apparatus recording the results of proton-proton collisions at the Large Hadron Collider (LHC), which is located at CERN in Geneva, Switzerland. The analysis is documented in a CMS Public Analysis Note [1] and an internal note [2]. A journal publication, including other CMS results, is underway.

The standard model of particle physics is the current best description of elementary particles and their interactions at the quantum level, successfully describing a wide range of phenomena over many orders of magnitude in energy up to the  $\sim 10^2$  GeV scale with excellent precision. However the standard model leaves some essential questions unanswered, foretelling the necessity of a more fundamental theory to explain physics beyond the standard model, at the TeV scale. One potential candidate is supersymmetry [3], which predicts a wealth of new particles. The LHC was built with the intention of searching for these new particles.

Within the standard model, the masses of the particles arise from the spontaneous breaking of the electroweak symmetry [4–6]. The top quark, with its high mass, has long been suspected to play a special role in this mechanism. Its coupling to hypothetical particles described by physics beyond the standard model

could potentially be large. It is therefore natural to search for new particles that couple to the top quark. We search for pair-produced new physics resonances that couple to a top quark and another parton. We study in detail the  $R$ -parity violating minimal supersymmetric model constrained to have minimal flavor violation [7], which allows bottom squarks ( $\tilde{b}$ ) to be the lightest supersymmetric particle and restricts their decays to a top quark and strange quark. Due to the excellent lepton resolution in CMS, we restrict our search to final states with two leptons, where both top quarks undergo leptonic decays. A Feynman diagram of this process is presented in Fig. 1.1.

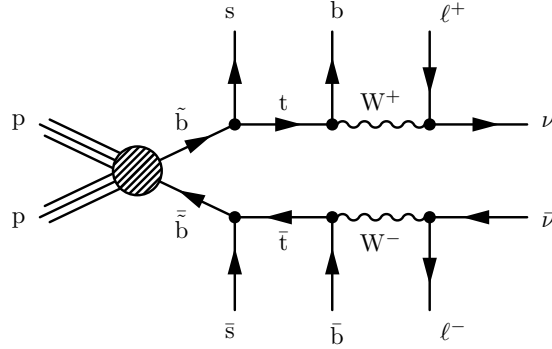


Figure 1.1: Leading order Feynman diagrams for  $R$ -parity violating bottom squark pair production.

This thesis is structured as follows. In Chapter 1 we outline the theoretical framework behind the standard model, supersymmetry, and the  $R$ -parity violating minimal supersymmetric model. The Large Hadron Collider and the Compact Muon Solenoid experiment are described in Chapter 2. Techniques for event and object reconstruction are detailed in Chapter 3. Finally in Chapter 4 we present a search for pair-produced  $R$ -parity violating bottom squarks decaying into a top quark and light parton. We conclude in Chapter 5.

In this chapter, we present the theoretical framework that serves as the basis

for the analysis presented in Chapter 4, which is  $R$ -parity violating supersymmetry.

In Section 1.2, we describe the standard model (SM) of particle physics, the theory that is the current best description of elementary particles and their interactions at the quantum level. However, although predictions of the SM have been in excellent agreement with data collected by experiments in the past century, it does not provide an answer for a certain number of questions, a few of which are presented in Section 1.2.5. Several models that attempt to provide explanations have been developed. We focus on one such model, supersymmetry (SUSY), in Sections 1.3 and 1.4. Faced with the most recent results from the ATLAS and CMS experiments, which have not yet found evidence for SUSY, we detail a modified version of the theory in Section 1.5. This is the model upon which the search presented in Chapter 4 is based.

## 1.2 The standard model Lagrangian

In this section we describe the SM in the formalism of quantum field theory. The discussion is based on Refs. [8, 9].

### 1.2.1 Gauge and fermion fields

The SM is a  $SU(3)_C \times SU(2)_L \times U(1)_Y$  gauge theory, with  $SU(3)$  symmetry in the color sector and  $SU(2)_L \times U(1)_Y$  in the electroweak (EWK) sector. The gauge bosons of the SM ( $W^\pm$  and  $Z^0$  bosons, photon, and gluons) are incorporated into

the Lagrangian via the field strength tensors  $W_{\mu\nu}^a$ ,  $B_{\mu\nu}$ , and  $G_{\mu\nu}^a$ :

$$B_{\mu\nu} = \partial_\mu B_\nu - \partial_\nu B_\mu, \quad (1.1a)$$

$$W_{\mu\nu}^a = \partial_\mu W_\nu^a - \partial_\nu W_\mu^a + g\epsilon^{abc}W_\mu^b W_\nu^c, \quad (1.1b)$$

$$G_{\mu\nu}^a = \partial_\mu G_\nu^a - \partial_\nu G_\mu^a + g_s f^{abc}G_\mu^b G_\nu^c, \quad (1.1c)$$

where:

- in the SU(1) sector, the structure is identical to that of classical Abelian electromagnetism;
- $g$  is the gauge coupling of the SU(2) sector, and  $\epsilon^{abc}$  is the antisymmetric tensor with  $\epsilon^{123} = 1$ ;
- $g_s$  is the strong coupling constant of SU(3), and the structure constants  $f^{abc}$  are related to the generators of SU(3) by  $[t^a, t^b] = if^{abc}t^c$ .

The  $W^\pm$  and  $Z^0$  bosons and photon are obtained from linear combinations of the first two fields  $B_\mu$  and  $W_\mu^a$ , while the last field  $G_\mu^a$  corresponds to the gluons. The corresponding kinetic terms in the SM Lagrangian are:

$$\mathcal{L}_{\text{gauge}} = -\frac{1}{4}G_{\mu\nu}^a G^{a\mu\nu} - \frac{1}{4}W_{\mu\nu}^a W^{a\mu\nu} - \frac{1}{4}B_{\mu\nu} B^{\mu\nu}. \quad (1.2)$$

Finally, gauge interactions are introduced in the SM Lagrangian with the covariant derivative:

$$D_\mu = \partial_\mu - ig'B_\mu Y - igW_\mu^a T^a - ig_s G_\mu^a t^a, \quad (1.3)$$

with  $g'$  the U(1) gauge coupling and  $T^a = \frac{\sigma^a}{2}$  the generators of SU(2), where  $\sigma^a$  are the Pauli matrices.

The SM contains the chiral fermion fields listed in Table 1.1. They are the color triplets  $Q_L$ ,  $u_R$  and  $d_R$ , and the color singlets  $L_L$  and  $e_R$ , where  $Q_L$  and  $L_L$

are  $SU(2)_L$  doublets; there exist three generations of each. Kinetic terms for the fermions are obtained by replacing  $\partial_\mu$  with the covariant derivative  $D_\mu$ , defined in Eq. 1.3, in the Dirac Lagrangian.

Table 1.1: Chiral Standard Model fermion fields and their quantum numbers.

Field	$SU(3)_C$	$SU(2)_L$	$U(1)_Y$
$Q_L = \begin{pmatrix} u_L \\ d_L \end{pmatrix}$	3	2	$\frac{1}{6}$
$u_R$	3	1	$-\frac{2}{3}$
$d_R$	3	1	$\frac{1}{3}$
$L_L = \begin{pmatrix} \nu \\ e_L \end{pmatrix}$	1	2	$-\frac{1}{2}$
$e_R$	1	1	1

### 1.2.2 The Higgs field

The mass terms for the above fermion and gauge fields are not gauge invariant and therefore cannot be included in the SM Lagrangian: as it currently stands, these fields must be massless. However, since the observed particles (quarks, leptons,  $W^\pm$  and  $Z^0$  bosons) are massive, the SM as described above is not complete. In order to write gauge-invariant mass terms, we must introduce a  $SU(2)_L$  doublet of scalar fields  $H = \phi$ , the Higgs doublet [3].

We can write the standard Lagrangian for a generic  $SU(2)$  doublet. Within

the SM, including interactions with the fermion fields:

$$\mathcal{L}_\phi = \left( D_\mu \phi \right)^\dagger (D^\mu \phi) - V(\phi) + \mathcal{L}_\phi^F, \quad (1.4)$$

where  $V(\phi)$  is the scalar potential for which we assume the most general, gauge-invariant form:

$$V(\phi) = -\mu^2 \phi^\dagger \phi + \lambda (\phi^\dagger \phi)^2, \quad (1.5)$$

where  $\mu$  and  $\lambda$  are unknown parameters. Let us examine the possible shapes of the potential, depending on the values of these parameters:

- $-\mu^2 > 0$  and  $\lambda > 0$  – the potential has a minimum at  $\phi = 0$ . In this case,  $SU(2) \times SU(1)$  (EWK) symmetry is unbroken, and the vacuum state is invariant. We know this is not the case in the SM – otherwise there would be no mechanism by which the gauge bosons acquire mass terms.
- $-\mu^2 < 0$  and  $\lambda > 0$  – the potential has minima at  $\phi \neq 0$ , and the vacuum state is not invariant.
- $\lambda < 0$  – the scalar potential is unbounded from below, and there is no stable vacuum. This is clearly not the case in the SM either.

Therefore in the SM  $-\mu^2 < 0$  and  $\lambda > 0$ , and the scalar potential has a minimum at  $\mu^2/2\lambda$ . Since  $\phi$  is an  $SU(2)$  doublet, its components can be written in terms of four real scalar fields. In consequence, the minimum  $\mu^2/2\lambda$  corresponds to a four-dimensional spherical surface, and the  $SU(2) \times SU(1)$  gauge transformations are rotations in this four-dimensional space.

In particular, there are three rotations that leave the ground state invariant, while it is not invariant under rotations in the fourth direction: these correspond

to three massless Goldstone bosons, which can be removed by selecting a particular gauge, and one massive particle, the Higgs boson. The non-invariance of the vacuum state breaks the EWK symmetry. The Higgs field may then be rewritten:

$$\phi(x) = \begin{pmatrix} 0 \\ v + h(x) \end{pmatrix}, \quad (1.6)$$

where  $v = \sqrt{\mu^2/\lambda}$  is the minimum of the potential and  $h$  is a fluctuation around this minimum,  $\langle h \rangle = 0$ . This gauge is the unitary gauge.

For future discussion, we note that the Higgs boson mass is given by:

$$m_H^2 = \lambda v^2. \quad (1.7)$$

The discovery of a SM Higgs-like particle, achieved with Run I data at the LHC experiments ATLAS and CMS [10, 11], was a significant milestone in that it completed the set of particles predicted by the SM. Thus far, measurements of the new particle's spin, couplings, and decays have agreed well with SM predictions [10–13]. Due to the excellent performance in reconstructing photons, electrons, and muons, the golden channels  $H \rightarrow \gamma\gamma$  and  $H \rightarrow ZZ^* \rightarrow 4\ell$  ( $\ell = e$  or  $\mu$ ) have the best resolution on the reconstructed Higgs boson mass; ATLAS has measured  $m_H = 126.0 \pm 0.4$  (stat.)  $\pm 0.4$  (syst.) while CMS obtains  $m_H = 125.3 \pm 0.4$  (stat.)  $\pm 0.5$  (syst.). The invariant mass of the reconstructed four-lepton system is presented in Fig 1.2.

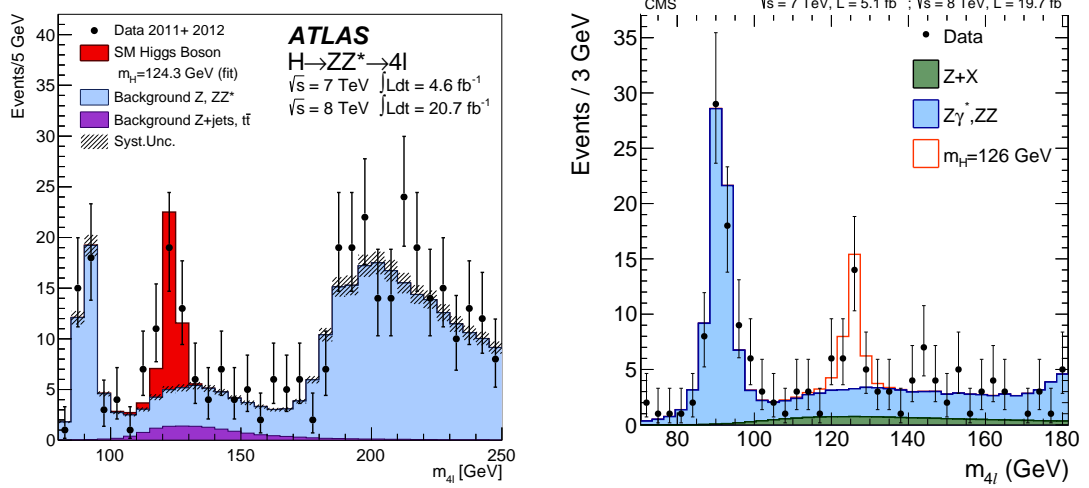


Figure 1.2: Distribution of the four-lepton invariant mass, in LHC Run I data and simulation, for the  $H \rightarrow ZZ^* \rightarrow 4\ell$  channel. Left: ATLAS result; right: CMS result.

### 1.2.3 Gauge boson masses

We now turn to the kinetic term in Eq. 1.4. Since the scalar  $\phi$  is a color singlet, we only consider the action of the first three terms in Eq. 1.3. Let:

$$\cos \theta_W \equiv c_W = \frac{g}{\sqrt{g^2 + g'^2}} \quad , \quad \sin \theta_W \equiv s_W = \frac{g'}{\sqrt{g^2 + g'^2}} ,$$

where  $\theta_W$  is the Weinberg angle. Defining the new basis:

$$W_\mu^\pm = \frac{W_\mu^1 \mp W_\mu^2}{\sqrt{2}}, \quad (1.8a)$$

$$Z_\mu = c_W W_\mu^3 - s_W B_\mu, \quad (1.8b)$$

$$A_\mu = s_W W_\mu^3 + c_W B_\mu, \quad (1.8c)$$

we can rewrite the kinetic term in a manner that makes the gauge boson mass terms and couplings to the Higgs field apparent.

For the  $W^\pm$  bosons, the kinetic term becomes:

$$\frac{1}{4} g^2 (h + v)^2 W_\mu^+ W^{-\mu} = \frac{(gv)^2}{4} W_\mu^+ W^{-\mu} + \frac{g^2 v}{2} h W_\mu^+ W^{-\mu} + \frac{g^2}{4} h^2 W_\mu^+ W^{-\mu}, \quad (1.9)$$

where we can identify the  $W^\pm$  mass  $m_W = (gv)^2/4$ , and the  $hW^\pm W^\pm$  and  $hhW^\pm W^\pm$  vertices have strengths  $g^2v/2$  and  $g^2/4$ , respectively.

The kinetic term for the  $Z^0$  boson can be written:

$$\frac{1}{8}(g^2 + g'^2)(h + v)^2 Z_\mu Z^\mu = \frac{(g^2 + g'^2)v^2}{8} Z_\mu Z^\mu + \frac{(g^2 + g'^2)v}{4} h Z_\mu Z^\mu + \frac{(g^2 + g'^2)}{8} h^2 Z_\mu Z^\mu, \quad (1.10)$$

where the  $Z^0$  mass is  $m_Z = (g^2 + g'^2)v^2/4$ , and the  $hZ^0Z^0$  and  $hhZ^0Z^0$  vertices have respective strengths  $(g^2 + g'^2)v/2$  and  $(g^2 + g'^2)/4$ .

The final term in the expansion is the kinetic term for the real scalar field  $h$ ,  $\frac{1}{2}\partial_\mu h\partial^\mu h$ ; the photon  $A_\mu$  does not couple to  $h$ , and is therefore massless. Identifying the coupling  $eQ \equiv gs_W T^3 + g'c_W Y$  in the expression for the covariant derivative in the gauge boson mass basis, we therefore have  $e = gs_W = g'c_W$  the quantum of electric charge, and each particle's value of  $Q = T^3 + Y$  determines its overall charge.

The covariant derivative term in the gauge boson mass basis is:

$$D_\mu = \partial_\mu - ig_s G_\mu^a t^a - i\frac{e}{s_W} (W_\mu^+ T^+ + W_\mu^- T^-) - i\frac{e}{s_W c_W} Z_\mu (T^3 - s_W^2 Q) - ie A_\mu Q. \quad (1.11)$$

#### 1.2.4 Fermion masses

In this paragraph, we concentrate on the interaction term  $\mathcal{L}_\phi^F$  between the scalar Higgs field and the fermions. We can use power-counting to construct the renormalizable couplings that are allowed in the Lagrangian.

To write terms for both the up-type and down-type quarks, it is necessary to introduce the complex conjugate  $\tilde{\phi}$ , which has  $Y = -1/2$ , of the SU(2) Higgs

doublet  $\phi$  (which has  $Y = 1/2$ ). The most general interaction term is:

$$\mathcal{L}_{\text{Yukawa}} = -\mathbf{y}_u \bar{Q}_L \tilde{\phi}^\dagger u_R - \mathbf{y}_d \bar{Q}_L \phi^\dagger d_R - \mathbf{y}_e \bar{L}_L \phi e_R + \text{h.c.}, \quad (1.12)$$

where  $\mathbf{y}_e$ ,  $\mathbf{y}_u$ ,  $\mathbf{y}_d$  are constant dimensionless Yukawa couplings. Since there are three generations of quarks and leptons, these are  $3 \times 3$  matrices containing 18 complex couplings overall.

Mass terms for the fermions are also obtained by replacing  $\phi$  by its expansion  $h + v$  around the minimum of the potential. We obtain the mass matrices:

$$\mathcal{M}^e = \frac{v}{\sqrt{2}} \mathbf{y}_e, \quad \mathcal{M}^u = \frac{v}{\sqrt{2}} \mathbf{y}_u, \quad \mathcal{M}^d = \frac{v}{\sqrt{2}} \mathbf{y}_d,$$

whose eigenvalues correspond to the quark mass eigenstates. For the leptons, there are three mass eigenstates corresponding to the electron, muon and tau. The quark matrices can be diagonalized simultaneously, yielding the six quark mass eigenstates. The up-type and down-type left-handed quarks are rotated differently; the mismatch of bases is responsible for vertices that violate flavor through the exchange of a  $W^\pm$  boson. The coupling strengths associated with these vertices are encoded in the Cabibbo-Kobayashi-Maskawa (CKM) matrix, which is parameterized by three mixing angles  $\theta_{12}$ ,  $\theta_{13}$ ,  $\theta_{23}$  between quark generations and one phase  $\delta$ , which is responsible for CP-violation.

The issue of neutrino masses is not important in the theoretical framework we investigate, and will not be discussed here.

In conclusion, the SM is governed by a finite list of parameters: the three lepton masses, the six quark masses, the three angles and one phase of the CKM matrix, the SU(1), SU(2) and SU(3) gauge couplings, the vacuum expectation value (VEV) of the Higgs field, and the Higgs boson mass, all of which have been measured to date.

### 1.2.5 Limitations of the standard model

Although experiments within the past century have all found results in excellent agreement with the SM [14], several open questions remain. We list a few important issues below.

**Gravity.** The gravitational force is much weaker than the other fundamental forces, the electromagnetic, weak and strong interactions; its impact on SM particles is negligibly small in comparison to these other forces. In addition, there is currently no description of gravity in the formalism of quantum field theory that is valid past the Planck scale. The question as to why gravity is so weak and how to incorporate it into the SM remain to be understood.

**Dark matter and dark energy.** Astrophysical observations show that matter as described by the SM, made up almost entirely of baryons (particles constituted by three quarks), represents less than 5% of the total matter in the Universe. The standard model of cosmology,  $\Lambda$ CDM, accounts for the remaining 95% by introducing dark matter, which is essential to understand large-scale gravitational effects, and dark energy, which is necessary to describe the observed acceleration of the expansion of the universe. Dark matter is generally assumed to be non-baryonic and to not interact electromagnetically; the current SM does not contain any good candidates. Dark energy is generally accepted to originate from the vacuum energy; its density as predicted by quantum electrodynamics is vastly inconsistent with experimental upper bounds.

**The hierarchy problem.** The insertion of virtual fermion or scalar loops of particles that couple to the Higgs field in its propagator yields divergent quantum corrections to the Higgs squared mass parameter  $m_H^2$  defined in Eq. 1.7. An

ultraviolet (UV) cutoff is used to regulate the loop integrals and avoid such unphysical divergences; this energy corresponds to the scale at which the SM is no longer valid, and new physics emerge. This UV cutoff can be anywhere between the TeV scale and the Planck scale  $M_{\text{Pl}} \approx 1.22 \times 10^{19}$  GeV, the scale at which quantum gravitational effects can no longer be neglected. Cancelling the corrections is necessary to account for the measured mass  $m_H = 125$  GeV [10, 11], but would require an unlikely level of fine-tuning, i.e., cancellations across many orders of magnitude, unless the UV cutoff, at which new physics emerge, is at the TeV scale.

**Neutrino masses.** Neutrino mixing has been experimentally observed [15–17] thus proving that neutrinos have small, non-zero masses. However the exact procedure by which neutrinos acquire their mass has not yet been determined.

### 1.2.6 Physics beyond the standard model: supersymmetry

New physics must emerge at a certain scale to answer the above open questions. In this section we focus on supersymmetry (SUSY). The description that follows below and in the next section is adapted from Ref. [3].

As mentioned in Section 1.2.5, quantum corrections to the Higgs mass, which arise from virtual loop contributions from particles that couple to the Higgs field, are divergent. Consider for example one-loop corrections to  $m_H^2$  from a fermion and a scalar, shown in Fig 1.3. Let the fermion  $f$  (scalar  $S$ ) have mass  $m_f$  ( $m_S$ ); it couples to the Higgs field via the interaction term  $-\lambda_f H \bar{f} f$  ( $-\lambda_S |H|^2 |S|^2$ ).

Corrections to  $m_H^2$  must be expressed in terms of  $\Lambda_{\text{UV}}$ , a UV cutoff that en-



Figure 1.3: One-loop quantum corrections to the Higgs squared mass parameter  $m_H^2$ , due to (a) a Dirac fermion  $f$ , and (b) a scalar  $S$ .

sures the loop integrals are finite. It represents the energy scale at which the SM is no longer valid, and a new (as yet unknown) theory describes particles and their interactions. The corrections to  $m_H^2$  from  $f$  and  $S$  are:

$$\Delta m_H^2 = -\frac{|\lambda_f|^2}{8\pi^2} \Lambda_{\text{UV}}^2 + \dots, \quad (1.13a)$$

$$\Delta m_H^2 = \frac{\lambda_S}{16\pi^2} \left[ \Lambda_{\text{UV}}^2 - 2m_S^2 \ln \frac{\Lambda_{\text{UV}}}{m_S} + \dots \right]. \quad (1.13b)$$

Taken separately, both corrections can become arbitrarily large. However, as Eq. 1.13 suggests, one can introduce a new symmetry that produces systematic cancellations of all the divergent terms, by pairing each SM fermion with a new boson, and each SM boson with a new fermion, such that  $\lambda_S = |\lambda_f|^2$ . This symmetry guarantees the cancellation of divergent contributions from virtual loops to the Higgs mass to all orders.

Supersymmetry (SUSY) predicts that all SM particles have an associated superpartner, whose spin differs from that of its SM counterpart by  $1/2$ . Thus, SM fermions have bosonic superpartners, and SM bosons have fermionic superpartners. The SM fermions (quarks, leptons and neutrinos) have superpartners called squarks, sleptons, and sneutrinos, respectively. Superpartners of the SM gauge bosons are called gauginos, while the Higgs boson superpartners are called higgsinos.

## 1.3 Components of a basic SUSY model

### 1.3.1 Chiral and gauge fields

A supersymmetry transformation acting on a fermionic state gives a bosonic state, and vice versa. In an interacting quantum field theory with chiral fermions, as is the case with the SM, generators  $Q$  and  $Q^\dagger$  of such a symmetry must satisfy the commutation and anti-commutation relations:

$$\{Q, Q^\dagger\} = P^\mu,$$

$$\{Q, Q\} = \{Q^\dagger, Q^\dagger\} = 0,$$

$$[P^\mu, Q] = [P^\mu, Q^\dagger] = 0.$$

The commutation rules for these generators define the supersymmetry algebra. Irreducible representations of the algebra are called supermultiplets, with each element of the supermultiplet corresponding to a single-particle state. A supermultiplet contains superpartner fermionic and bosonic states that have identical gauge interactions – otherwise the cancellations in  $\Delta m_H^2$  disappear – and with identical numbers of fermionic ( $n_F$ ) and bosonic ( $n_B$ ) degrees of freedom.

The simplest supermultiplet contains a left-handed Weyl fermion  $\psi$  (spin-1/2, complex two-component object). It has four off-shell degrees of freedom, and two on-shell degrees of freedom corresponding to one equation of motion each for  $\psi$  and  $\psi^\dagger$ . The simplest superpartner is a complex scalar (spin-0) field  $\phi$  with two degrees of freedom, corresponding to the real and imaginary components of the field. In order for  $n_B$  to match  $n_F$ , it is necessary to introduce a

non-propagating complex scalar auxiliary field  $F$ , which has two off-shell degrees of freedom and zero on-shell degrees of freedom. The combination of  $\psi$ ,  $\phi$  and  $F$  is called a chiral supermultiplet.

The next simplest supermultiplet contains a massless spin-1 vector boson, which has two on-shell degrees of freedom corresponding to the two possible helicity states. It also has three off-shell degrees of freedom, since the gauge transformation equation reduces  $n_B$  from four to three. The simplest superpartner is a Weyl fermion that has four off-shell degrees of freedom, and two on-shell degrees of freedom. In order to have  $n_F = n_B$  in this case, we must introduce a real bosonic auxiliary field  $D$  with one off-shell degree of freedom and zero on-shell degrees of freedom. This combination is called a gauge supermultiplet.

In the  $N = 1$  supersymmetry framework, in which there is one distinct copy of  $Q$  and  $Q^\dagger$ , all other representations are reducible to combinations of chiral and gauge supermultiplets. This is the simplest case in which the known SM particles can be integrated, and the one we focus on here.

Since none of the predicted superpartners can be matched to known SM particles, they must correspond to entirely new particles. Additionally, because no equal-mass superpartners have been observed, supersymmetry must be broken, with superpartners much heavier than their SM counterparts. In order to guarantee that supersymmetry-breaking does not spoil the cancellations in divergent quadratic corrections to the Higgs squared mass, a so-called “soft” SUSY-breaking term,  $\mathcal{L}_{\text{soft}}$ , must be included in the supersymmetric Lagrangian; it contains only mass terms and coupling parameters that have positive mass dimensions. The  $\mathcal{L}_{\text{soft}}$  term is discussed in more detail in Section 1.3.5. The

superpartners do not necessarily correspond to mass eigenstates: EWK symmetry breaking and SUSY breaking allow for mixing of the different gauginos and higgsinos, and different masses for elements of one supermultiplet.

We now turn to the task of writing the Lagrangian density for a supersymmetric model.

### 1.3.2 Free supermultiplets

**Free chiral supermultiplet.** In this paragraph, we establish the expression for the Lagrangian density of a free chiral supermultiplet:

$$\mathcal{L}_{\text{chiral}} = \mathcal{L}_{\text{scalar}} + \mathcal{L}_{\text{fermion}} + \mathcal{L}_{\text{auxiliary}}$$

A chiral supermultiplet contains a Weyl fermion  $\psi$ , a complex scalar field  $\phi$ , and a complex non-propagating field  $F$ . The standard kinetic terms for  $\psi$  and  $\phi$ ,  $-\partial^\mu \phi^* \partial_\mu \phi$  and  $i\psi^\dagger \bar{\sigma}^\mu \partial_\mu \psi$ , can be added to the Lagrangian density.

To determine how the scalar and fermion fields transform under a supersymmetric transformation, we require the action to be invariant under such a transformation. In order to preserve the group structure, we must also require closure of the supersymmetry algebra, i.e., the commutator of two supersymmetry transformations must also be a supersymmetry transformation.

The most general transformation satisfying these conditions is parameterized by an infinitesimal spinor  $\epsilon_a$ , with  $\partial_\mu \epsilon = 0$  (we only consider global trans-

formations<sup>1)</sup>. The transformation rules for the fields  $\phi$ ,  $\psi$  and  $F$  are:

$$\begin{aligned}\delta\phi &= \epsilon\psi, & \delta\phi^* &= \epsilon^\dagger\psi^\dagger, \\ \delta\psi_\alpha &= -i(\sigma^\mu\epsilon^\dagger)_\alpha\partial_\mu\phi + \epsilon_a F, & \delta\psi_{\dot{\alpha}}^\dagger &= i(\epsilon\sigma^\mu)_{\dot{\alpha}}\partial_\mu\phi^* + \epsilon_{\dot{\alpha}}^\dagger F^*, \\ \delta F &= -i\epsilon^\dagger\bar{\sigma}^\mu\partial_\mu\psi, & \delta F^* &= i\partial_\mu\psi^\dagger\bar{\sigma}^\mu\epsilon,\end{aligned}$$

where spinor indices on scalars have been contracted.

The free Lagrangian density for a chiral supermultiplet is then:

$$\mathcal{L}_{\text{chiral}} = -\partial^\mu\phi^*\partial_\mu\phi + i\psi^\dagger\bar{\sigma}^\mu\partial_\mu\psi + F^*F,$$

implying that the auxiliary field  $F$  follows the equations of motion  $F = F^* = 0$ . Because no kinetic term for  $F$  appears in the Lagrangian, the auxiliary field is non-propagating.

**Free gauge supermultiplet.** A gauge supermultiplet contains a massless gauge boson  $A_\mu^a$ , a Weyl fermion gaugino  $\lambda^a$ , and a real bosonic auxiliary field  $D^a$ , where the index  $a$  refers to an element in the adjoint representation of the gauge group:  $a = 1\dots 8$  for  $SU(3)_C$  color,  $a = 1, 2, 3$  for  $SU(2)_L$  weak isospin, and  $a = 1$  for  $U(1)_Y$  weak hypercharge.

Gauge transformations are parameterized by an infinitesimal gauge transformation parameter  $\Lambda^a$ , the gauge coupling strength  $g$ , and the antisymmetric structure constants  $f^{abc}$  defining the gauge group:

$$\delta_{\text{gauge}}A_\mu^a = \partial_\mu\Lambda^a + gf^{abc}A_\mu^b\Lambda^c,$$

$$\delta_{\text{gauge}}\lambda^a = gf^{abc}\lambda^b\Lambda^c.$$

---

<sup>1</sup>Local transformations, with  $\partial_\mu\epsilon \neq 0$ , are unnecessarily general, requiring a supersymmetric theory of gravity. In the limit that gravity is weak, global transformations are sufficient to describe the SM.

For the action to be invariant under a supersymmetry transformation, the fields must transform as:

$$\begin{aligned}\delta A_\mu^a &= \frac{1}{\sqrt{2}}(\epsilon^\dagger \bar{\sigma}_\mu \lambda^a + \lambda^{\dagger a} \bar{\sigma}_\mu \epsilon), \\ \delta \lambda_\alpha^a &= \frac{i}{2\sqrt{2}}(\sigma^\mu \sigma^\nu \epsilon)_\alpha F_{\mu\nu}^a + \frac{1}{\sqrt{2}}\epsilon_\alpha D^a, \\ \delta D^a &= \frac{i}{\sqrt{2}}(-\epsilon^\dagger \bar{\sigma}^\mu D_\mu \lambda^a + D_\mu \lambda^{\dagger a} \bar{\sigma}^\mu \epsilon).\end{aligned}$$

The free Lagrangian density for a gauge supermultiplet is then:

$$\mathcal{L}_{\text{gauge}} = -\frac{1}{4}F_{\mu\nu}^a F_{\mu\nu}^a + i\lambda^{\dagger a} \bar{\sigma}^\mu D_\mu \lambda^a + \frac{1}{2}D^a D^a, \quad (1.18)$$

where  $F_{\mu\nu}^a = \partial_\mu A_\nu^a - \partial_\nu A_\mu^a + g f^{abc} A_\mu^b A_\nu^c$  and the covariant derivative of the gaugino field is  $D_\mu \lambda^a = \partial_\mu \lambda^a + g f^{abc} A_\mu^b \lambda^c$ .

Here too, the auxiliary field has a trivial equation of motion  $D^a = 0$ . However, once chiral and gauge supermultiplets are coupled, this will not be the case anymore.

### 1.3.3 Interaction terms

**Interactions of chiral supermultiplets.** This paragraph describes how to construct non-gauge interaction terms for a collection of chiral supermultiplets, indexed by  $i$ , containing a Weyl fermion  $\psi_i$ , a complex scalar field  $\phi_i$ , and a complex scalar auxiliary field  $F_i$ . The dual requirements that the Lagrangian be invariant under supersymmetry transformations, and renormalizable by power counting, greatly constrain the form of these terms.

The most general interaction term can be written in terms of a complex function that is analytical in the scalar fields  $\phi_i$ , the superpotential  $W$ :

$$W = L^i \phi_i + \frac{1}{2} M^{ij} \phi_i \phi_j + \frac{1}{6} y^{ijk} \phi_i \phi_j \phi_k, \quad (1.19)$$

where  $L_i$  are parameters with dimension [mass]<sup>2</sup>, and  $M^{ij}$  is a symmetric mass matrix for the fermion fields. In analogy with previous results from field theory,  $y^{ijk}$  can be interpreted as a Yukawa coupling between a scalar  $\phi_k$  and two fermions  $\psi_j$  and  $\psi_k$ , and is symmetric under interchange of  $i, j, k$ .

The parameters  $L_i$  only appear in the scalar potential, through a term proportional to the superpotential squared; in particular, terms linear in a scalar field will be present. This is only allowed if the field is a gauge singlet, and since there are no such chiral fields in the SM, as they are forbidden by gauge transformations, the term will be omitted from this point forward.

The interaction part of the Lagrangian density for a collection of chiral supermultiplets can then be written:

$$\mathcal{L}_{\text{int}} = -\frac{1}{2} (W^{ij} \psi_i \psi_j + W_{ij}^* \psi^{\dagger i} \psi^{\dagger j}) - W^i W_i^*,$$

with:

$$W^{ij} = \frac{\delta^2 W}{\delta \phi_i \delta \phi_j} = M^{ij} + y^{ijk} \phi_k, \quad W^i = \frac{\delta W}{\delta \phi_i} = M^{ij} \phi_j + \frac{1}{2} y^{ijk} \phi_j \phi_k.$$

The masses of the fermions and scalars are obtained by computing the equations of motion for these fields, using the full Lagrangian density (sum of the free and interaction terms). In consequence, the masses of the fermion and boson elements of a supermultiplet are given by the same squared mass matrix  $(M^2)_i^j = M_{ik}^* M^{kj}$ . Chiral supermultiplets therefore contain a mass-degenerate complex scalar and Weyl fermion, as postulated (recall that a supersymmetry-breaking term has not yet been included in the Lagrangian).

The non-propagating auxiliary fields  $F_i$  and  $F^{*i}$  have been eliminated from the Lagrangian density using their equations of motion  $F_i = -W_i^*$ ,  $F^{*i} = -W^i$ .

We express for future use the scalar potential  $V(\phi, \phi^*) = W^i W_i^*$ :

$$V(\phi, \phi^*) = M_{ik}^* M^{kj} \phi^{*i} \phi_j + \frac{1}{2} M^{in} y_{jkn}^* \phi_i \phi^{*j} \phi^{*k} + \frac{1}{2} M_{in}^* y^{ikn} \phi^{*i} \phi_j \phi_k + \frac{1}{4} y^{ijn} y_{klm}^* \phi_i \phi_j \phi^{*k} \phi^{*l} \quad (1.20)$$

The Lagrangian density can then be written:

$$\begin{aligned} \mathcal{L} = & -\partial^\mu \phi^{*i} \partial_\mu \phi_i - V(\phi, \phi^*) + i \psi^{\dagger i} \bar{\sigma}^\mu \partial_\mu \psi - \frac{1}{2} M^{ij} \psi_i \psi_j - \frac{1}{2} M_{ij}^* \psi^{\dagger i} \psi^{\dagger j} \\ & - \frac{1}{2} y^{ijk} \phi_i \psi_j \psi_k - \frac{1}{2} y_{ijk}^* \phi^{*i} \psi^{\dagger j} \psi^{\dagger k} \end{aligned} \quad (1.21)$$

**Gauge interactions.** The properties under gauge transformations of the gauge supermultiplets were studied in Section 1.3.2. Because they act on different spaces, supersymmetry and gauge transformations commute. The fields in a chiral supermultiplet are therefore in the same representation of the gauge group, and transform as:

$$\delta_{\text{gauge}} X_i = ig \Lambda^a (T^a X)_i,$$

where  $X_i = \phi_i, \psi_i, F_i$ , and  $T^a$  is a set of Hermitian matrices satisfying the standard commutation relation  $[T^a, T^b] = if^{abc}T^c$ , which correspond to the representation chosen for the gauge transformation.

For the Lagrangian density to be invariant under the gauge transformation, the ordinary derivative  $\partial_\mu$  is replaced by the covariant derivative  $D_\mu$ , whose action on the fields is defined as:

$$D_\mu \phi_i = \partial_\mu \phi_i - ig A_\mu^a (T^a \phi)_i, \quad (1.22a)$$

$$D_\mu \phi^{*i} = \partial_\mu \phi^{*i} + ig A_\mu^a (\phi^* T^a)^i, \quad (1.22b)$$

$$D_\mu \psi_i = \partial_\mu \psi_i - ig A_\mu^a (T^a \psi)_i. \quad (1.22c)$$

This effectively couples vector bosons residing in gauge supermultiplets with scalars and fermions in chiral supermultiplets.

Other allowed interactions, i.e., with field dimension less than [mass]<sup>4</sup>, couple gaugino  $\lambda^a$  and auxiliary  $D^a$  fields. They have the form:

$$(\phi^* T^a \psi) \lambda^a, \quad \lambda^{\dagger a} (\psi^\dagger T^a \phi), \quad (\phi^* T^a \phi) D^a.$$

The interactions described above can be combined into the full Lagrangian density for a renormalizable supersymmetric theory, which is invariant up to total derivatives under a transformation of the chiral fields:

$$\delta\phi_i = \epsilon\psi_i,$$

$$\delta\psi_{i\alpha} = -i(\sigma^\mu \epsilon^\dagger)_\alpha D_\mu \phi_i + \epsilon_\alpha F_i,$$

$$\delta F_i = -i\epsilon^\dagger \bar{\sigma}^\mu D_\mu \psi_i + \sqrt{2}g(T^a \phi)_i \epsilon^\dagger \lambda^{\dagger a}.$$

The full Lagrangian density is:

$$\mathcal{L} = \mathcal{L}_{\text{chiral}} + \mathcal{L}_{\text{gauge}} - \sqrt{2}g(\phi^* T^a \psi) \lambda^a - \sqrt{2}g\lambda^{\dagger a}(\psi^\dagger T^a \phi) + g(\phi^* T^a \phi) D^a, \quad (1.24)$$

where the regular derivatives in  $\mathcal{L}_{\text{chiral}}$  have been replaced by the gauge-covariant derivatives defined in Eq. 1.22.

The strength  $g$  of the last three terms in the Lagrangian is determined by the gauge coupling, although these terms are not gauge interactions in the ordinary field theory sense. The first and second of these terms correspond to couplings between gauginos and chiral fields; the last term combined with the  $D^a$  term in  $\mathcal{L}_{\text{gauge}}$  give the equation of motion for the auxiliary gauge field  $D^a = -g(\phi^* T^a \phi)$ .

Note that both types of auxiliary fields ( $F_i$  and  $D^a$ ) can be expressed as a function of the scalar fields.

The scalar potential for this Lagrangian density is:

$$V(\phi^*, \phi) = F^{*i}F_i + \frac{1}{2} \sum_a D^a D^a = W_i^* W^i + \frac{1}{2} \sum_a g_a^2 (\phi^* T^a \phi)^2. \quad (1.25)$$

The terms in this expression are called *F*-term and *D*-term contributions, respectively, and are regulated exclusively by the other interactions in the theory: fermion mass terms and Yukawa couplings for the *F*-term, and gauge interactions for the *D*-term.

### 1.3.4 SUSY model-building

The expression for the full supersymmetric Lagrangian density shows that all interactions and masses are determined by properties under gauge transformations, and by the superpotential.

The full supersymmetric Lagrangian density, expanded to make all interaction vertices explicit, is given in Eq. 1.21. The last two terms correspond to scalar-fermion-fermion couplings. There is also a (scalar)<sup>4</sup> coupling, which arises from the last term in the superpotential given in Eq. 1.19. These types of vertices all have dimensionless couplings.

The Lagrangian also contains interactions with a coupling strength of dimension [mass], corresponding to (scalar)<sup>3</sup> interactions from the middle terms of Eq. 1.20; and [mass]<sup>2</sup>, from the first term in Eq. 1.20, and fourth and fifth terms in Eq. 1.21, which are the scalar and fermion propagators, respectively.

We come next to the supersymmetric gauge interaction vertices. The field strength term in Eq. 1.18 yields cubic and quartic gauge boson interaction vertices. The covariant derivative in Eq. 1.22 introduces gauge boson-fermion and gauge boson-scalar field interactions, which can be of type scalar-scalar-gauge boson and fermion-fermion-gauge boson. Fermion-gaugino-scalar interactions emerge from the third and fourth terms in Eq. 1.24. Finally, the last term in Eq. 1.25 is responsible for (scalar)<sup>4</sup> interactions, this time with a strength determined by the gauge coupling.

These represent general rules for building an interacting theory; we will soon specify the superpotential in the case of the Minimal Supersymmetric standard model (MSSM).

### 1.3.5 Soft SUSY breaking

Since no superpartners with masses equal to that of their SM counterparts have been observed, supersymmetry must be spontaneously broken: the Lagrangian is invariant under supersymmetry transformations, but the ground state is not. Supersymmetry breaking is explicitly introduced in the supersymmetric Lagrangian through the addition of a term  $\mathcal{L}_{\text{soft}}$ .

By construction this term violates supersymmetry, but must contain only mass terms and couplings with positive mass dimension. Dimensionless and negative mass dimension SUSY breaking terms are forbidden: dimensionless couplings will spoil the cancellations in  $\Delta m_H^2$ , while negative mass dimension couplings imply that supersymmetry breaks down beyond a certain energy scale, requiring a new mechanism to constrain  $\Delta m_H^2$  and avoid fine-tuning, this

time at a much higher scale.

In the context of a model with minimal field content, as is discussed here, the allowed soft SUSY-breaking terms may be written

$$\mathcal{L}_{\text{soft}} = - \left( \frac{1}{2} M_a \lambda^a \lambda^a + \frac{1}{6} a^{ijk} \phi_i \phi_j \phi_k + \frac{1}{2} b^{ij} \phi_i \phi_j + t^i \phi_i \right) + \text{c.c.} - \left( m^2 \right)_j^i \phi^{j*} \phi_i,$$

where  $M^a$  are gaugino masses for each group,  $\left( m^2 \right)_j^i$  and  $b^{ij}$  are scalar squared-mass terms,  $a^{ijk}$  are (scalar)<sup>3</sup> couplings, and  $t_i$  are tadpole couplings, which can be omitted in analogy with the  $L_i$  term in the scalar potential, due to the absence of a chiral gauge singlet candidate in the SM. Although (scalar)<sup>3</sup> couplings  $c_i^{jk}$  between the fields  $\phi^{*i}$ ,  $\phi_j$ , and  $\phi_k$  are in principle allowed, these tend to be vanishingly small in any model with spontaneous SUSY breaking, and are typically neglected.

Mass splittings between superpartners and their SM counterparts are controlled by  $m_{\text{soft}}$ , the highest mass scale associated with terms in  $\mathcal{L}_{\text{soft}}$ . Corrections to the Higgs squared mass parameter due to these terms may be written

$$\Delta m_H^2 = m_{\text{soft}}^2 \left[ \frac{\lambda}{16\pi^2} \ln \left( \frac{\Lambda_{\text{UV}}}{m_{\text{soft}}} \right) + \dots \right],$$

where higher-order loop corrections and terms independent of the UV cutoff are not explicitly written. The coupling  $\lambda$  stands for any dimensionless coupling.

In order to avoid fine-tuning,  $m_{\text{soft}}$  can therefore not be too large, and the lightest superpartners at least cannot be too heavy. If the UV cutoff  $\Lambda_{\text{UV}}$  is of order the Planck scale, for  $\lambda \sim 1$  the upper bound on the masses of the lightest superpartners is approximately 1 TeV.

## 1.4 The Minimal Supersymmetric Standard Model

### 1.4.1 Particle content

The SM Higgs boson is spin-0, and must therefore reside in a chiral supermultiplet<sup>2</sup>. Fermionic partners of the Higgs are called higgsinos.

The SM fermions, leptons, neutrinos and quarks, have left- and right-handed components which transform differently under gauge transformations; these fermions must reside in chiral supermultiplets. Their spin-0 superpartners are called sleptons, sneutrinos and squarks, respectively. Since elements of a supermultiplet have the same gauge transformation, there is one distinct superpartner for left and right-handed fermions.

SM vector bosons, which have spin-1, must be contained in gauge supermultiplets, along with their fermionic superpartners, which are called gauginos. The supersymmetric partners of the  $W^\mu$  and  $B^\mu$  bosons, mediators of the EWK gauge symmetry, are respectively called the winos and bino; after EWK symmetry breaking the  $W^0$  and  $B^0$  gauge eigenstates mix to form the  $Z^0$  and  $\gamma$ , whose superpartners are called zino and photino. The gluon, mediator of color gauge interactions, has a spin-1/2 superpartner called the gluino  $\tilde{g}$ .

The full particle content of the MSSM is presented in Table 1.2.

The MSSM contains four neutral fermions, the superpartners of the  $B^0$  and  $W^0$  and two higgsinos. Electroweak symmetry breaking mixes the neutral hig-

---

<sup>2</sup>Actually, two Higgs chiral supermultiplets with weak hypercharge  $Y = \pm 1/2$  are required to give mass to both up-type quarks ( $Y = +1/2$ ), and down-type quarks and leptons ( $Y = -1/2$ ). A reason for this will be given in section 1.4.2.

Table 1.2: Fermion and gauge fields of the Minimal Supersymmetric Standard Model and their quantum numbers.

Field	spin	spin	SU(3) <sub>C</sub>	SU(2) <sub>L</sub>	U(1) <sub>Y</sub>
chiral	0	1/2			
$Q$	$\begin{pmatrix} \tilde{u}_L \\ \tilde{d}_L \end{pmatrix}$	$\begin{pmatrix} u_L \\ d_L \end{pmatrix}$	<b>3</b>	<b>2</b>	$\frac{1}{6}$
$\bar{u}$	$\tilde{u}_R^*$	$u_R^\dagger$	<b>3̄</b>	<b>1</b>	$-\frac{2}{3}$
$\bar{d}$	$\tilde{d}_R^*$	$d_R^\dagger$	<b>3̄</b>	<b>1</b>	$\frac{1}{3}$
$L$	$\begin{pmatrix} \tilde{\nu} \\ \tilde{e}_L \end{pmatrix}$	$\begin{pmatrix} \nu \\ e_L \end{pmatrix}$	<b>1</b>	<b>2</b>	$-\frac{1}{2}$
$\bar{e}$	$\tilde{e}_R^*$	$e_R^\dagger$	<b>1</b>	<b>1</b>	1
$H_u$	$\begin{pmatrix} H_u^+ \\ H_u^0 \end{pmatrix}$	$\begin{pmatrix} \tilde{H}_u^+ \\ \tilde{H}_u^0 \end{pmatrix}$	<b>1</b>	<b>2</b>	$+\frac{1}{2}$
$H_d$	$\begin{pmatrix} H_d^+ \\ H_d^0 \end{pmatrix}$	$\begin{pmatrix} \tilde{H}_d^+ \\ \tilde{H}_d^0 \end{pmatrix}$	<b>1</b>	<b>2</b>	$-\frac{1}{2}$
gauge	1/2	1			
	$\tilde{g}$	$g$	<b>8</b>	<b>1</b>	0
$\tilde{W}$	$\tilde{W}^\pm, \tilde{W}^0$	$W^\pm, W^0$	<b>1</b>	<b>3</b>	0
$\tilde{B}$	$\tilde{B}^0$	$B^0$	<b>1</b>	<b>1</b>	0

gsinos  $\tilde{H}_u^0$  and  $\tilde{H}_d^0$  and gauginos  $\tilde{B}$  and  $\tilde{W}^0$  to form four mass eigenstates called neutralinos  $\tilde{N}_i$ , conventionally labelled in ascending order of mass. Usually,  $\tilde{N}_1$  is assumed to be the LSP.

The charged higgsinos  $\tilde{H}_u^+$  and  $\tilde{H}_d^-$  mix with the charged winos  $\tilde{W}^\pm$  to form two mass eigenstates with charge  $\pm 1$ , called charginos  $\tilde{C}_1, \tilde{C}_2$ , with  $m_{\tilde{C}_1} < m_{\tilde{C}_2}$ .

The gluino is the only color octet fermion in the MSSM, and therefore cannot mix with any other particle.

The MSSM contains 21 scalar fields that are superpartners of the SM right- and left-handed quarks and leptons. For the first generation, these are the four squarks  $\tilde{u}_L, \tilde{u}_R, \tilde{d}_L, \tilde{d}_R$ , two sleptons  $\tilde{e}_L, \tilde{e}_R$  and a sneutrino  $\tilde{\nu}_{e_L}$ ; similar copies exist for the other generations.

### 1.4.2 Superpotential and interactions

Before applying the general expression for the superpotential, based on Eq. 1.19, to the MSSM, we must identify the different possible terms.

The Yukawa term couples a scalar and two fermion fields of chiral supermultiplets, which in the case of the MSSM can be the squarks and quarks, or sleptons and leptons, or Higgs and higgsinos. The mass term couples scalar fields of chiral supermultiplets, which in this case are squarks or sleptons.

Thus we obtain a superpotential of the form:

$$W_{\text{MSSM}} = \bar{u}\mathbf{y_u}QH_u - \bar{d}\mathbf{y_d}QH_d - \bar{e}\mathbf{y_e}LH_d + \mu H_u H_d.$$

The signs are chosen so that the terms giving quark and lepton masses have

positive sign. The  $\mu$  term is the supersymmetric equivalent of the SM Higgs boson mass. It produces both higgsino mass terms and Higgs squared-mass terms.

Based on this expression, it is clear why two Higgs supermultiplets are needed to produce Yukawa couplings, and hence masses, to all families of quarks and leptons: the superpotential must be an analytical function of the scalar fields only, and not their complex conjugates, so that terms of the form  $\bar{u}QH_d^*$  cannot replace  $\bar{u}QH_u$ ; similarly for  $\bar{e}LH_u^*$  and  $\bar{e}LH_d$ .

Once the neutral scalar components of the Higgs have acquired non-zero VEVs, the  $3 \times 3$  Yukawa matrices  $\mathbf{y}_u$ ,  $\mathbf{y}_d$  and  $\mathbf{y}_e$  will determine current masses, and constrain the mixing angles between quark generations (much like the CKM matrix in the SM). In the approximation that the third generation of quarks and leptons is much heavier than the first two, we can assume that only the (3, 3) element of these matrices is non-zero. Let these couplings be called  $y_t$ ,  $y_b$  and  $y_\tau$ . This simplifies the expression for the MSSM superpotential:

$$W_{\text{MSSM}} \approx y_t(\bar{t}tH_u^0 - \bar{t}bH_u^+) - y_b(\bar{b}tH_d^- - \bar{b}bH_d^0) - y_\tau(\bar{\tau}\nu_\tau H_d^- - \bar{\tau}\tau H_d^0) + \mu(H_u^+H_d^- - H_u^0H_d^0). \quad (1.26)$$

In addition to the Higgs-quark-quark and Higgs-lepton-lepton couplings made explicit in the superpotential, squark-higgsino-quark and slepton-higgsino-lepton couplings also exist. For example, based on the superpotential, the SM coupling of top, anti-top and Higgs has strength  $y_t$ . Since the Yukawa coupling  $y^{ijk}$  is completely symmetric under the exchange of  $i$ ,  $j$  and  $k$ , the stop-Higgsino-top couplings also have strength  $y_t$ . The same holds for the exchange of a t and b quark, as can be seen in the second term of Eq. 1.26.

These are not the only terms with couplings that are a power of  $y_t$ . As the last term in the expression for the scalar potential in Eq. 1.20 shows, there will also be (scalar)<sup>4</sup> terms of strength  $y_t^2$ , coupling four stops or two stops and two Higgs. Since the Yukawa couplings are symmetric, the exchange of a stop for a sbottom squark yields an interaction of the same strength. In general, all scalar quartic couplings [(squark)<sup>4</sup>, (slepton)<sup>4</sup>, (squark)<sup>2</sup>(slepton)<sup>2</sup>, (squark)<sup>2</sup>(Higgs)<sup>2</sup> and (slepton)<sup>2</sup>(Higgs)<sup>2</sup>] can be obtained from elements of  $\mathbf{y_u}$ ,  $\mathbf{y_d}$  and  $\mathbf{y_e}$ .

Note that since the Yukawa couplings are quite small, superpartners will most likely be produced via gauge-strength supersymmetric interactions, for example squark-quark-gluino, squark-quark-wino and slepton-lepton-wino (the wino can only couple to left-handed squarks and sleptons), squark-quark-bino and slepton-lepton-bino, Higgs-higgsino-wino and Higgs-higgsino-bino, with strength proportional to the electroweak gauge couplings  $g$  (wino) and  $g'$  (bino). In addition, the last term in Eq. 1.24 allows for (scalar)<sup>4</sup> terms, for example (Higgs)<sup>4</sup>, proportional to  $g^2$  and  $g'^2$ .

### 1.4.3 *R*-parity

The supersymmetric Lagrangian is expressed in Eq. 1.24. It is possible to write other, additional terms that do not conserve baryon and lepton numbers. This type of interaction has not been experimentally observed; the most notable consequence is that the decay time of a proton into states containing a lepton and meson must be greater than  $10^{32}$  years. Therefore a new symmetry, called *R*-parity (or matter parity), is introduced to eliminate terms in the renormalizable Lagrangian that violate baryon and lepton number conservation; it is defined

for each particle as:

$$P_R = (-1)^{3(B-L)+2s},$$

where  $B$  and  $L$  are the baryon and lepton numbers, respectively, and  $s$  the spin of the particle.

By construction, the known SM particles are even under  $R$ -parity, while their superpartners, called sparticles, are odd, because their spins differ by exactly 1/2. Conservation of  $R$ -parity implies that regular particles and sparticles cannot mix, and each interaction vertex in the supersymmetric theory must contain an even number of particles with  $P_R = -1$ . The MSSM is *defined* to conserve  $R$ -parity.

There are three phenomenologically important consequences to  $R$ -parity conservation:

- The lightest supersymmetric particle (LSP) is stable, because there are no other  $P_R = -1$  states to which it can decay. If the LSP is electrically neutral, it is a good dark matter candidate.
- Other sparticle decay chains must include an odd number of LSPs.
- Sparticles can only be pair-produced in collider experiments.

#### 1.4.4 Naturalness

In minimal SUSY the symmetry between fermions and bosons cancels the divergent terms in Eq. 1.13. However SUSY must be broken, and SUSY-breaking terms in the Lagrangian may introduce new divergent terms in  $\Delta m_H^2$  that must

also be regulated by a cutoff scale. Excessive fine-tuning can nevertheless be avoided for sparticle masses at or near the TeV scale [18].

SUSY models with a mass spectrum satisfying the above requirement are called natural SUSY models. In many of these, the stop and sbottom squarks are expected to be the lightest squarks; searches for superpartners have often aimed at discovering these particular sparticles. Since they strongly couple to their third generation SM counterparts, multiple b quarks are expected to be produced in collisions. These can in turn be reconstructed.

### 1.4.5 Experimental signature

At hadron colliders, sparticles must be pair-produced, either in interactions of EWK or strong (QCD) strength. At the LHC, gluon-gluon and gluon-quark fusion dominates, producing gluinos and squarks, although associated production of a chargino or neutralino with a squark or gluino is also allowed (with a smaller cross-section).

Since sparticles must be pair-produced, and their decay chains always include at least one LSP, the final state is characterized by a minimum of  $2m_{\text{LSP}}$  of missing energy. Due to the fact that the longitudinal component of parton momenta is unknown in hadron colliders (each parton has a momentum that is an unkown fraction of the proton to which it belongs), only missing energy in the direction transverse to the beam ( $E_{\text{T}}^{\text{miss}}$ ) is observable. In general, the experimental signature of SUSY includes zero or more leptons, zero or more jets, and  $E_{\text{T}}^{\text{miss}}$ . If the lightest stop and sbottom are light enough, typical SUSY events can have high b-jet multiplicities.

Multiple searches targeting these signatures have been performed, at the LHC and elsewhere [19–23]. With data from its first run, the LHC has already placed stringent bounds on the MSSM, excluding large swaths of parameter space at low masses. Figure 1.4 presents a summary of limits obtained by CMS sparticle production in certain decay channels, as a function of the sparticle mass and for different LSP masses. Already the TeV scale favored by naturalness is nearly excluded.

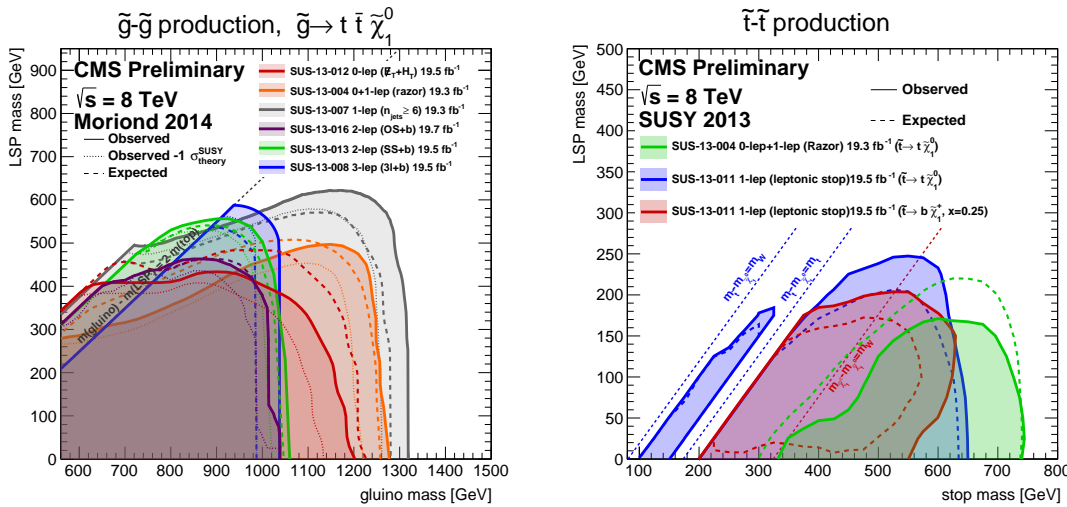


Figure 1.4: Left: summary of CMS limits on gluino pair production, with the gluino decaying to top anti-top neutralino, in the  $m_{\tilde{g}} - m_{\text{LSP}}$  plane. Right: summary of CMS limits on stop squark pair production in the  $m_{\tilde{t}} - m_{\text{LSP}}$  plane.

In recent years, the focus has therefore switched to other new physics models, in particular those in which the LSP decays promptly, resulting in an experimental signature without significant  $E_T^{\text{miss}}$ , a direct consequence of  $R$ -parity conservation. In Section 1.5, we will describe one such model, the  $R$ -parity violating MSSM constrained to have Minimal Flavor Violation (MFV) [7]. This model provides the theoretical motivation for the search presented in Chapter 4.

## 1.5 *R*-parity violating SUSY with Minimal Flavor Violation

In this section we present the theoretical framework that forms the basis for the analysis performed in this thesis.

### 1.5.1 Superpotential

Instead of requiring strict *R*-parity conservation, as in the framework of the MSSM, *R*-parity violating terms may be introduced into the Lagrangian. Provided the couplings are small enough, these terms will not conflict with current experimental bounds on the proton lifetime [24].

In the MFV framework, instead of *R*-parity conservation, the sole Yukawa couplings are hypothesized to violate flavor symmetry. Due to their size, these couplings, along with CKM factors, contribute to suppressing the *R*-parity violating terms in the Lagrangian. As shown in Ref. [7], in the limit of vanishing neutrino masses, the proton is still stable; we will therefore restrict ourselves to the limit of zero-mass neutrinos.

With the inclusion of these terms, only one new allowed operator is renormalizable and can be added to the MSSM superpotential given in Eq. 1.26:

$$W_{\text{BNV}} = \frac{1}{2} w'' (\mathbf{y}_u \bar{u}) (\mathbf{y}_d \bar{d}) (\mathbf{y}_d \bar{d}), \quad (1.27)$$

where  $w''$  is an unknown  $O(1)$  coefficient. As noted, this term exclusively violates baryon number (BNV); lepton number is still conserved in this modified MSSM.

### 1.5.2 BNV vertices and coupling strengths

In this section, we evaluate the coupling strengths associated with the BNV vertex in Eq. 1.27.

Through an  $SU(3)^5$  rotation, we can move to the basis in which the Yukawa matrices can be expressed simply in terms of the CKM matrix  $V_{CKM}$ , the Higgs VEVs  $v_u$  and  $v_d$ , and the quark masses:

$$\mathbf{y}_u = \frac{1}{v_u} V_{CKM}^\dagger \begin{pmatrix} m_u & 0 & 0 \\ 0 & m_c & 0 \\ 0 & 0 & m_t \end{pmatrix}, \quad \mathbf{y}_d = \frac{1}{v_d} \begin{pmatrix} m_d & 0 & 0 \\ 0 & m_s & 0 \\ 0 & 0 & m_b \end{pmatrix}, \quad \mathbf{y}_e = \frac{1}{v_d} \begin{pmatrix} m_e & 0 & 0 \\ 0 & m_\mu & 0 \\ 0 & 0 & m_\tau \end{pmatrix}.$$

The new  $R$ -parity and baryon-number violating term can be written:

$$W_{BNV} = \frac{1}{2} \lambda''_{ijk} \epsilon^{abc} \bar{u}_a^i \bar{d}_b^j \bar{d}_c^k, \quad (1.28)$$

where  $a, b, c$  are color indices and  $i, j, k$  are flavor indices, and in this particular basis the coupling strength is given by:

$$\lambda''_{ijk} = w'' y_i^{(u)} y_j^{(d)} y_k^{(d)} \epsilon_{jkl} V_{il},$$

$y_i^{(u)}$  and  $y_i^{(d)}$  being the up- and down-type Yukawa couplings. There are nine distinct vertices, whose strengths can be estimated using the following quark masses [14]:

$$m_u \sim 3 \text{ MeV} , \quad m_c \sim 1.3 \text{ GeV} , \quad m_t \sim 173 \text{ GeV} ,$$

$$m_d \sim 6 \text{ MeV} , \quad m_s \sim 100 \text{ MeV} , \quad m_b \sim 4 \text{ GeV} ,$$

the lepton masses:

$$m_e \simeq 0.511 \text{ MeV} , \quad m_\mu \simeq 106 \text{ MeV} , \quad m_\tau \sim 1.78 \text{ GeV} ,$$

and the CKM matrix:

$$V_{CKM} \sim \begin{pmatrix} 1 & \lambda & \lambda^3/2 \\ \lambda & 1 & \lambda^2 \\ \lambda^3 & \lambda^2 & 1 \end{pmatrix},$$

where  $\lambda \sim 1/5$  gives an estimate of the matrix elements to within 20% accuracy.

Consequently, the nine vertices have strengths parameterized by  $\tan\beta$ , the ratio of the Higgs VEVs  $v_u$  and  $v_d$ :

$$\begin{aligned} \lambda''_{usb} &\sim \tan^2 \beta \frac{m_b m_s m_u}{m_t^3}, & \lambda''_{ubd} &\sim \lambda \tan^2 \beta \frac{m_b m_d m_u}{m_t^3}, & \lambda''_{uds} &\sim \lambda^3 \tan^2 \beta \frac{m_d m_s m_u}{2m_t^3}, \\ \lambda''_{csb} &\sim \lambda \tan^2 \beta \frac{m_b m_c m_s}{m_t^3}, & \lambda''_{ cbd} &\sim \tan^2 \beta \frac{m_b m_c m_d}{m_t^3}, & \lambda''_{cds} &\sim \lambda^2 \tan^2 \beta \frac{m_c m_d m_s}{m_t^3}, \\ \lambda''_{tsb} &\sim \lambda^3 \tan^2 \beta \frac{m_b m_s}{m_t^2}, & \lambda''_{tbd} &\sim \lambda^2 \tan^2 \beta \frac{m_b m_d}{m_t^2}, & \lambda''_{tds} &\sim \tan^2 \beta \frac{m_d m_s}{m_t^2}. \end{aligned} \quad (1.30)$$

Taking  $w'' = 1$  and  $\tan\beta = 45$ , we subsequently obtain the approximate values:

$$\begin{aligned} \lambda''_{usb} &\sim 5 \times 10^{-7}, & \lambda''_{ubd} &\sim 6 \times 10^{-9}, & \lambda''_{uds} &\sim 3 \times 10^{-12}, \\ \lambda''_{csb} &\sim 4 \times 10^{-5}, & \lambda''_{ cbd} &\sim 1.2 \times 10^{-5}, & \lambda''_{cds} &\sim 1.2 \times 10^{-8}, \\ \lambda''_{tsb} &\sim 2 \times 10^{-4}, & \lambda''_{tbd} &\sim 6 \times 10^{-5}, & \lambda''_{tds} &\sim 4 \times 10^{-5}. \end{aligned} \quad (1.31)$$

Since the parameter  $\lambda''_{tsb}$  dominates by an order of magnitude, we expect the most common MFV RPV SUSY interactions to occur between third-generation particles.

### 1.5.3 Phenomenology

The experimental signature of MFV RPV SUSY will depend on the nature of the LSP. As previously noted, since  $R$ -parity is no longer required to be conserved, the LSP is allowed to decay. Furthermore, the assumption that the LSP be electrically and color neutral places unnecessary restrictions, and is accordingly dropped.

The mass spectrum of the model is dictated by the constraints MFV places on squark and slepton masses [7]: CKM elements and Yukawa couplings suppress all but the stop, sbottom and stau. Other squarks and sleptons are much heavier and usually degenerate, but there can be one light stop or sbottom squark. Thus, we consider the natural scenario of a third generation squark LSP. Both stop and sbottom LSP scenarios are considered in Ref. [7]; in the context of this thesis we study the case of a sbottom LSP.

As described in Section 1.5.2, the sbottom will decay to a top and strange quark in 99% of cases. The remaining sbottom decays mainly produce top and down quarks. Displaced vertices (greater than  $50\mu\text{m}$ ) are expected only for  $\tan\beta \lesssim 10$ . Hence, at the LHC we expect to see increased top quark production in conjunction with light jets. This signature is the subject of this thesis.

## CHAPTER 2

### ACCELERATOR AND DETECTOR

The subject of this thesis is a search for new physics resonances using data collected with the CMS detector, a general-purpose apparatus recording the results of proton-proton collisions from beams delivered by the LHC accelerator complex, located at CERN. The LHC is described below in Section 2.1. Characteristics of the CMS detector are presented in Section 2.2.

#### **2.1 The Large Hadron Collider**

Following the motivations for physics beyond the SM outlined in Chapter 1, there was an international consensus to build a TeV collider, the Large Hadron Collider (LHC), in order to probe this particular range of energies in search of new physics. In addition, the LHC would provide another opportunity to search for the Higgs boson, in parallel with the CDF and D0 experiments at Fermilab.

The collider was built at CERN, re-purposing accelerator facilities and an underground tunnel below the Franco-Swiss border that had previously been the site of the LEP collider. We briefly describe the accelerator and collider below, following closely the material in Ref. [25]. A more in-depth description can be found elsewhere [26].

### 2.1.1 Machine layout and operation

The LHC is a circular proton-proton collider with a circumference of 26.7 km, housed in a tunnel built beneath the Earth's surface, at a depth varying between 45 and 170 m, on a 1.4% incline towards Geneva and the Lac Léman. Hadron colliders present the advantage that synchrotron radiation is much smaller than at electron-positron colliders, allowing for higher center-of-mass energies to be probed. The choice of protons, which are readily available, required a double-ring configuration with proton beams circulating in opposite directions. A schematic view of the LHC and CERN accelerator complex is presented in Fig. 2.1 [27].

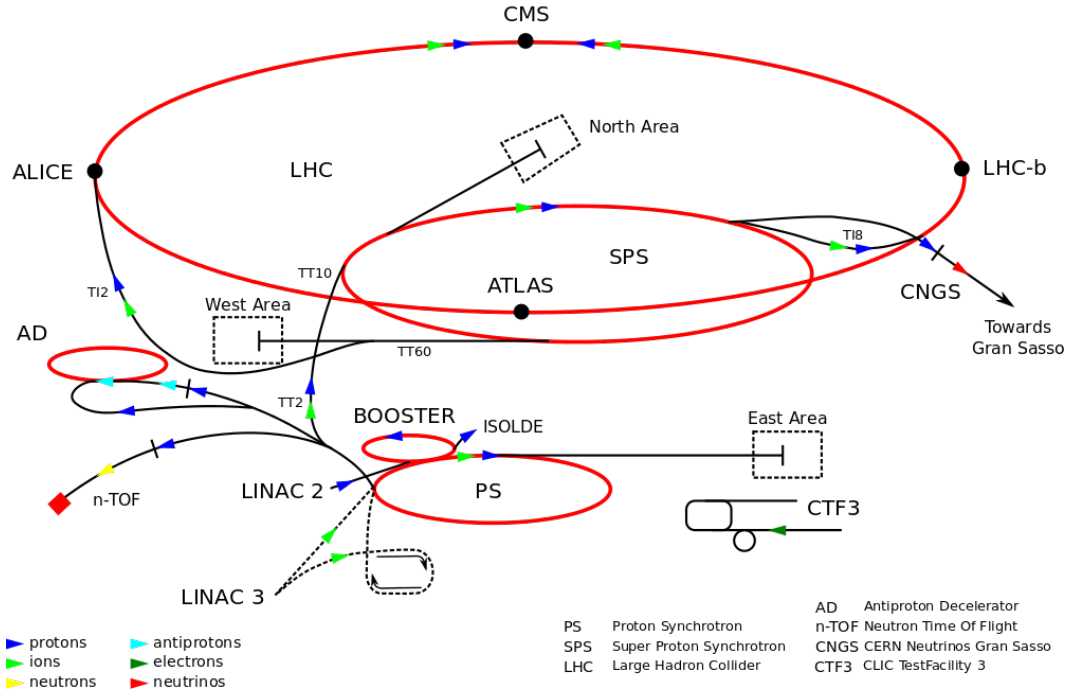


Figure 2.1: Schematic view, not to scale, of the Large Hadron Collider and accelerator complex at CERN. The different LHC experiments, ALICE, ATLAS, CMS, and LHCb, are denoted by black points around the circumference.

Protons are obtained by stripping electrons from hydrogen atoms using an ion source. They then go through the machine's injection chain, which comprises the following elements. The Linac2 is a linear accelerator that accelerates protons to 50 MeV. Protons are then channeled into a series of circular accelerators: the Proton Synchrotron Booster (PSB) of radius 25 m that accelerates protons to 1.4 GeV; the Proton Synchrotron (PS) with a circumference of 630 m accelerates protons to 26 GeV; and the Super Proton Synchrotron (SPS) with a circumference of 6.9 km, which brings protons to 450 GeV before injecting them into the LHC rings.

The LHC machine is composed of arcs alternating with straight sections. Arcs contain dipole magnets that serve to bend protons around the circumference of the tunnel, while straight sections contain quadrupole magnets acting to focus the proton beams. Superconducting technologies are employed to produce the high magnetic fields (8.3 T), and thus high currents, that are necessary: the magnets are built using niobium-titanium Rutherford cables, and superfluid helium is used to efficiently absorb heat generated in coils throughout the magnet structures.

Protons circulating in the LHC rings are accelerated using radio frequency (RF) cavities that produce oscillating electric fields: protons traveling around the ring at a frequency that is an integer multiple of the resonant frequency of the cavity are accelerated at each revolution. This creates a discrete structure in the beams, where protons are grouped into bunches with a well-defined spacing between each. The RF cavities operate at 400 MHz and produce an overall voltage per beam of 16 MV/m.

The two counter-rotating proton beams are brought into collision at four in-

teraction points (IP) around the ring, at which experiments are located to record the interactions. These correspond to the two general-purpose experiments ATLAS (A Toroidal LHC Apparatus) and CMS, and the two specialized experiments ALICE (A Large Ion Collider Experiment) and LHCb. In order to avoid parasitic interactions between multiple proton bunches, the beams collide with a crossing angle  $\theta_c \sim \mu\text{rad}$  instead of head-on.

The LHC's main quadrupole magnets constitute a magnetic lattice that acts to alternatively focus and defocus the proton beams, producing independent oscillations of varying amplitudes in the plane transverse to the beam direction  $s$  (by convention, the axis is oriented in the clockwise direction). Individual protons are deflected differently by the magnets, depending on their momentum and initial transverse position in the injected bunches; the maximum amplitude is parameterized by the beta function  $\beta(s)$ , a machine-dependent quantity that plays a significant role in evaluating the performance of the machine. The value of the beta function at the interaction point is called  $\beta^*$ .

The motion of protons within a bunch through the magnetic lattice creates a transverse spread in the beam, with a size at position  $s$  that depends on the beta function as  $\sigma(s) = \sqrt{\varepsilon \beta(s)}$ , where  $\varepsilon$  is the emittance of the beam, defined as the contour confining a given fraction of the protons. Particles within the beam are assumed to be normally distributed. Generally, a more useful parameter that is independent of beam energy is the normalized emittance  $\varepsilon_n = \beta \gamma \varepsilon$ , where  $\beta$  and  $\gamma$  are the relativistic parameters.

### 2.1.2 Performance

The performance of the LHC is measured in terms of the delivered luminosity  $\mathcal{L}$ , which depends on a limited number of beam parameters: the number of protons per bunch  $N_b$ , the number of bunches per beam  $n_b$ , the revolution frequency of the protons  $f$ , the relativistic factor of the protons  $\gamma$ , the normalized transverse beam emittance  $\epsilon_n$ , the value of the beta function at the interaction point  $\beta^*$ , and a factor  $F \lesssim 1$  accounting for the crossing angle between beams.

Assuming the two counter-rotating beams are identical, round at the interaction points, and the protons are normally distributed within the beams, the luminosity is given by

$$\mathcal{L} = \frac{N_b^2 n_b f \gamma}{4\pi \epsilon_n \beta^*} F. \quad (2.1)$$

The parameter  $F$  quantifies the reduction in luminosity associated with increasing the crossing angle:

$$F = \frac{1}{\sqrt{1 + \left(\frac{\theta_c \sigma_z}{2\sigma^*}\right)^2}}, \quad (2.2)$$

where  $\sigma_z$  is the RMS bunch length and  $\sigma^*$  the beam size at the collision point.

Beam parameters are listed in Table 2.1, which compares the design values to the settings used in 2012, when the data used in this thesis were collected. Gradually, as protons are lost in collisions, the luminosity decreases, and it is necessary to dump the beams and start a new fill. The luminosity integrated over time  $L_{\text{int}}$  is directly related to the number of events produced in the proton-proton collisions,

$$N = \sigma_{\text{total}} L_{\text{int}} = \sigma_{\text{total}} \int \mathcal{L} dt,$$

where  $\sigma_{\text{total}} \sim 100 \text{ mb}$  is the 8 TeV cross section of proton-proton processes at the LHC. In 2012, the LHC delivered a total integrated luminosity in proton-proton

Table 2.1: Some LHC machine parameters and their values in 2012, compared to the design specifications.

Parameter		2012	Design	Unit
Collision energy	$\sqrt{s}$	8	14	TeV
Protons per bunch	$N_b$	$1.7 \times 10^{11}$	$1.15 \times 10^{11}$	
Bunches per beam	$n_b$	1380	2808	
Bunch separation	$\tau_{\text{bunch}}$	50	25	ns
Beta function at the IP	$\beta^*$	60	55	cm
Normalized emittance	$\varepsilon_n$	2.5	3.75	$\mu\text{m mrad}^{-1}$
Luminosity	$\mathcal{L}$	up to $8 \times 10^{33}$	$10^{34}$	$\text{cm}^{-2} \text{s}^{-1}$

collisions of  $23.30 \text{ fb}^{-1}$ .

The majority of physics processes that CMS intends to observe have cross sections measured in pb, a factor of  $10^{11}$  smaller than  $\sigma_{\text{total}}$ . In fact, inelastic scattering events, with a cross section  $\sigma_{\text{inelastic}} \approx 70 \text{ mb}$  at 8 TeV, account for the majority of events observed in proton-proton collisions at the LHC, and represent a major difficulty in isolating potentially “interesting” events. On average we expect  $N_{\text{inelastic}} = \sigma_{\text{inelastic}} \tau_{\text{bunch}} \mathcal{L}$  such interactions per bunch. Using values from Table 2.1, we estimate that an average of 28 inelastic scattering interactions per beam crossing, referred to as pile-up, occurred in 2012.

## 2.2 The Compact Muon Solenoid

The LHC hosts several experiments with multiple physics goals. Amongst them, ATLAS and CMS were intended to spearhead the search for the Higgs

boson and physics beyond the SM. In this section we describe the CMS detector, focusing on components that play an essential role in reconstructing the physics objects used in the analysis described in Chapter 4: leptons, jets, and missing transverse energy. A more complete description can be found elsewhere [28,29].

CMS is a cylindrically shaped detector measuring 21.6 m in length, 14.6 m in diameter, and weighing 12.5 kt. The innermost layer of the detector is a silicon tracker that is used to reconstruct the trajectories of charged particles. It is surrounded by electromagnetic and hadronic calorimeters, which record energy deposits from charged and neutral particles, respectively. These lay inside the coils of a superconducting solenoid that provides the high magnetic field necessary to accurately measure the momenta of charged particles. Outside of this volume, interspersed with the iron return yoke of the magnet, are detectors for muons. Due to their mass (approximately 200 times that of electrons), muons lose less energy to Bremsstrahlung radiation than electrons and interact less frequently with detector material. They are thus more likely to travel from the interaction region, through the inner layers, and reach this region of the detector. A diagram of the detector is presented in Fig. 2.2 [29].

The experiment uses the following coordinate conventions. The coordinate system is centered at the interaction point. The  $x$  axis is oriented radially inward, toward the center of the LHC; the  $y$  axis points vertically upward. The  $z$  axis is oriented along the counter-clockwise rotating proton beam. Azimuthal angles  $\phi$  are measured from the  $x$  axis and in the  $x - y$  plane. Polar angles  $\theta$  are measured from the  $z$  axis. Pseudo-rapidity  $\eta$ , commonly used instead of the polar angle, is defined as  $\eta = -\log \tan(\theta/2)$ .

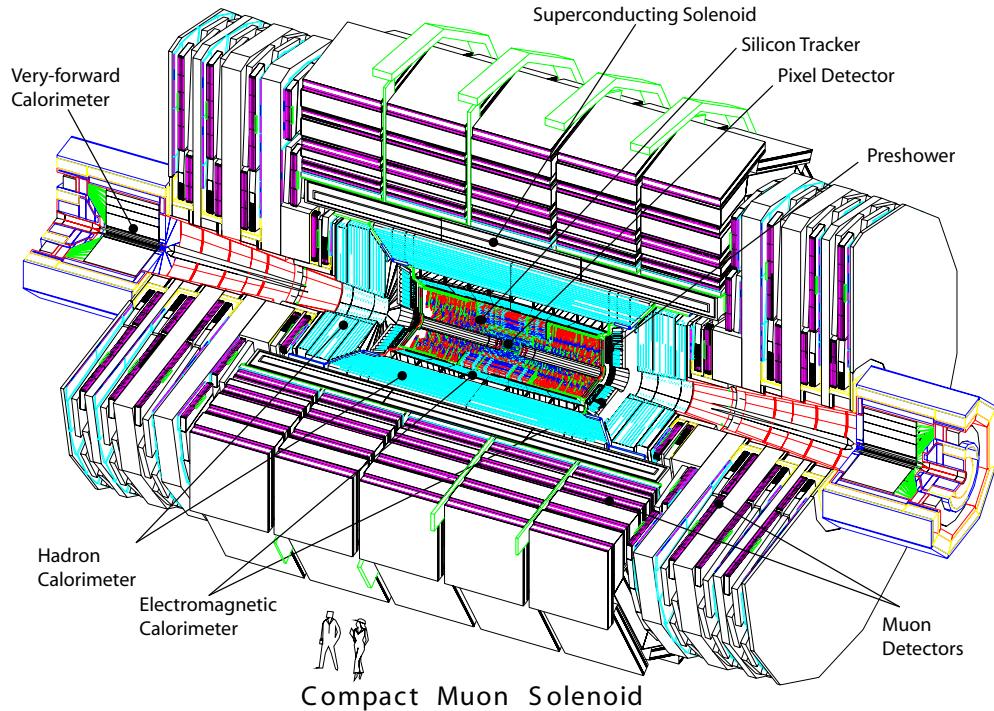


Figure 2.2: Layout of the CMS detector, showing the location of the different sub-detectors.

### 2.2.1 Tracking systems

Due to the proximity of the tracker to the interaction point, its design poses multiple challenges. At a distance of 4 cm from the IP, the charged particle flux resulting from high luminosity collisions is expected to be of order  $10^8 \text{ s}^{-1}$  [29]. The high flux results in an extremely dense tracking environment, potentially high occupancy for detectors close to the IP, and high radiation. In order to deal with these challenges, the tracker is designed to be finely segmented, resulting in low occupancy; to have excellent track resolution, in order to successfully reconstruct secondary vertices from the decays of heavy-flavor objects; and to be radiation-hard.

The inner tracking system extends radially to  $r = 110$  cm and has a length of 540 cm. Dual silicon pixel and silicon microstrip systems, offering hermetic coverage in the  $r - \phi$  plane, are used. The tracker is composed of an Inner Barrel, an Outer Barrel (longer than the Inner Barrel), and two Endcaps, one on each side of the tracker barrel. A diagram of the inner tracker in the  $r - z$  plane is presented in Fig 2.3 [30].

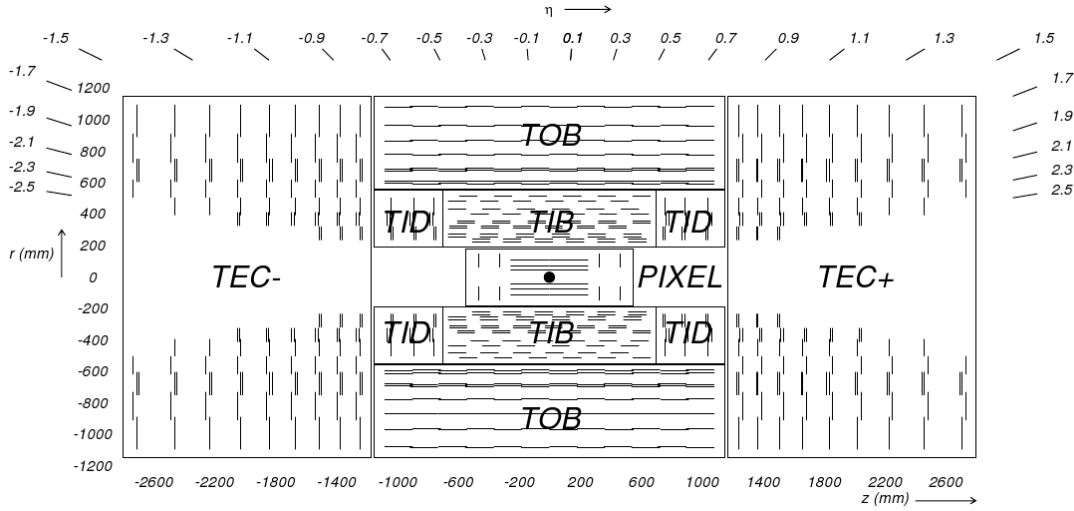


Figure 2.3: A view of the CMS tracking systems in the  $r - z$  plane. These consist of the pixel detector, tracker inner and outer barrels (TIB and TOB), tracker inner disks (TID), and tracker endcaps (TEC).

### 2.2.1.1 Pixel tracker

Silicon pixels are used in the region closest to the interaction point, up to  $r \approx 10$  cm. The pixels have dimensions of  $100 \times 150 \mu\text{m}^2$  (and  $285 \mu\text{m}$  thick), resulting in an occupancy of approximately  $10^{-4}$  per bunch crossing. The barrel region comprises three layers of pixels that are located at  $r = 4.4, 7.3$ , and  $10.2$  cm; each layer is 53 cm long, and is hermetic in  $r$  and  $\phi$ . On either side are two end disks,

at  $|z| = 34.5$  and  $46.5$  cm, which extend between  $r = 6$  and  $15$  cm. The layout of the pixel detector is illustrated in Fig. 2.4 [29].

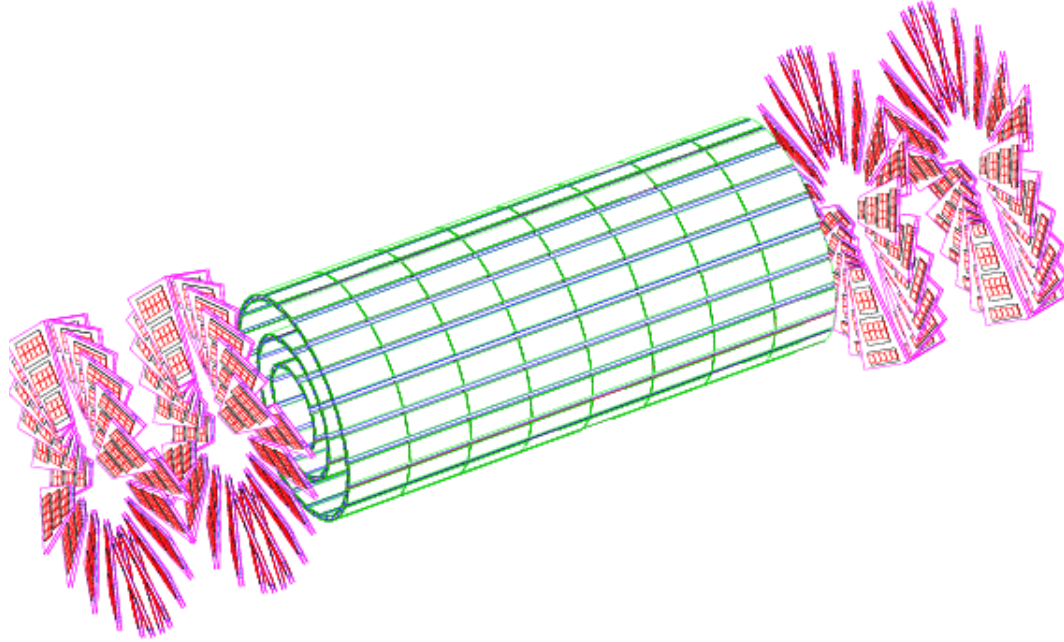


Figure 2.4: Perspective view of the CMS pixel detector, the innermost tracking system.

In the barrel portion of the pixel detector (BPix), each layer is divided into two half-cylinders, one in the  $+z$  direction and the other in the  $-z$  direction. A half-cylinder is composed of ladders and half-ladders situated to ensure hermetic coverage in  $r$  and  $\phi$  up to  $|\eta| < 2.5$ , and which provide the necessary structural support and cooling. The barrel is made up of 768 modules that are divided into half-ladders of four identical modules each. The read-out of each module is performed by 16 Read-Out Chips (ROC), bump-bonded to the sensors, which each read a  $52 \times 80$  array of pixels. There are 48 million pixels in the BPix.

The pixel endcaps (FPix) are composed of two disk, with each disk compris-

ing multiple blades (trapezoidal-shaped panels) that are rotated by  $20^\circ$ , creating a turbine-like geometry. Each blade is constructed from different-sized plaquettes that hermetically cover the blade. There are 672 plaquettes overall, with 7 modules per blade and between two and ten ROCs per module, for a total of 18 million pixels in the FPix. There are thus 66 million unique channels in the pixel detector, which has an area of  $1\text{ m}^2$ .

The strength of the magnetic field inside the pixel detector is 4 T. Charged particles moving in this field are deflected perpendicularly from their path along electric field. Ionizing particles traversing a pixel create electron-holes pairs that drift across the sensor and into neighboring pixels. This charge-sharing effect between neighboring pixels increases spatial resolution by providing a measure of the center of gravity of the overall charge. The spatial resolution of the pixel detector is  $10\mu\text{m}$  in  $r - \phi$  and  $20\mu\text{m}$  in  $z$ . The geometry of the pixel detector provides track measurements (three in the barrel, two in the endcap) within  $|\eta| < 2.5$ .

### 2.2.1.2 Strip tracker

At a distance of  $r \approx 20\text{ cm}$ , the particle flux has decreased to a level at which silicon microstrips provide sufficient resolution to reconstruct tracks. Between 20 and 55 cm, these have minimum dimensions  $10\text{ cm} \times 80\mu\text{m}$ , and have an occupancy of 2–3% per bunch crossing; while above 55 cm the minimum dimensions are  $25\text{ cm} \times 80\mu\text{m}$ , and the occupancy  $\approx 1\%$  per bunch crossing. The layout of the silicon microstrip detector is illustrated in Fig. 2.5 [29].

In the barrel the silicon tracker extends to  $r = 110\text{ cm}$  and is divided into the

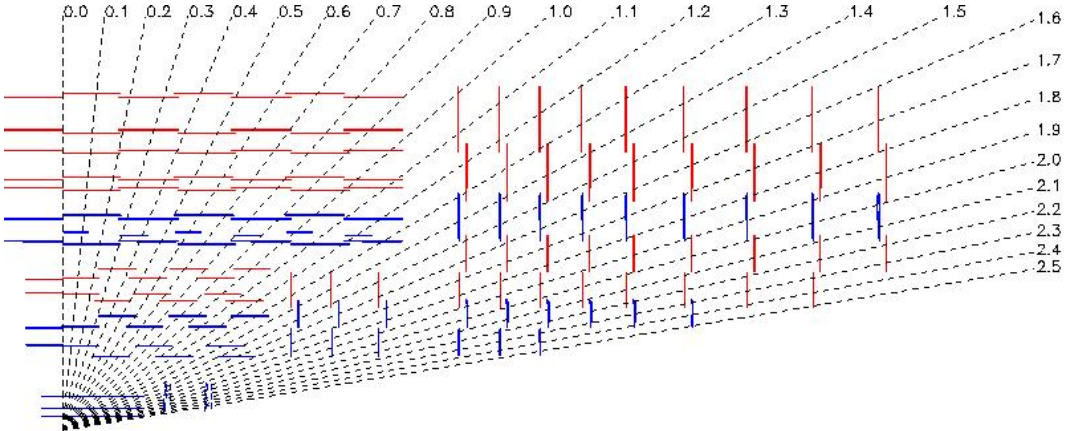


Figure 2.5: Layout of one quarter of the CMS silicon microstrip tracker in the  $r - z$  plane.

Tracker Inner Barrel (TIB) and Tracker Outer Barrel (TOB), which are composed of rectangular sensors. The TIB, composed of four layers of silicon microstrips of thickness  $320\mu\text{m}$  and pitch varying from  $80$  to  $120\mu\text{m}$ , extends to  $|z| = 65\text{ cm}$ . The TOB comprises six layers of  $500\mu\text{m}$ -thick microstrips with pitch between  $120$  and  $180\mu\text{m}$ , and extends to  $|z| = 110\text{ cm}$ . The first two layers of the TIB and TEC consist of double-sided modules made from two back-to-back sensors with a stereo angle of  $100\text{ mrad}$ , allowing for measurements parallel and perpendicular to the strip.

The forward strip tracker is separated into the Tracker End Cap (TEC) and the Tracker Inner Disks (TID), and is built using different wedge-shaped sensors. The TEC disks, composed of nine microstrip layers of thickness  $320$  or  $500\mu\text{m}$ , cover the region  $120\text{ cm} < |z| < 280\text{ cm}$ , while the TID, comprising three disks each with thickness  $320\mu\text{m}$ , are located in the space between the TIB and TEC. Strips are placed in concentric rings that are centered on the beam line, with sensors pointing toward the beam line. The modules are mounted on petals that are attached to the disks. The strip pitch varies between  $100$  and  $140\mu\text{m}$  in

the TID, and 140 and  $180\mu$  in the TEC. As in the barrel, certain layers are made up of stereo modules: the first two rings of the TID, and the first two and fifth rings of the TEC.

There are 15 148 modules overall in the strip tracker, each composed of one thin or two thick sensors, with 24 244 sensors total and 9.6 million silicon strips spread over  $200\text{ m}^2$ . Each sensor consists of 512 or 768 strips, with blocks of 256 channels sent via fiber-optic cable to be processed through one read-out channel, the strip tracker Front End Driver (FED). The strip tracker has 450 FEDs overall. The tracker is hermetic in  $r - \phi$  up to  $|\eta| < 2.5$ , and provides a resolution of approximately  $30\mu\text{m}$  in  $r - \phi$  and  $230\mu\text{m}$  in  $z$ .

## 2.2.2 Calorimeter systems

We describe below the two calorimeter systems used in the CMS experiment, the Electromagnetic Calorimeter (ECAL) and the Hadronic Calorimeter (HCAL).

### 2.2.2.1 Electromagnetic calorimeter

One of the design goals of the ECAL was to successfully reconstruct decays of Higgs bosons to a pair of photons. In practice the ECAL records energy deposits from photons, electrons and other charged particles using crystals that scintillate when traversed by ionizing radiation, and photodetectors that measure the emitted photon shower. In its environment inside the detector, the ECAL faces challenges similar to that of the tracker. It was therefore designed to be finely segmented, with a fast response, and radiation-resistant.

The ECAL is divided into a barrel section (EB) and endcaps (EE) on either side. In addition there is a preshower system (ES) that is located on the inner face of the EE. The calorimeter is hermetic with the EB covering the pseudorapidity range  $|\eta| < 1.479$ , the EE extending to  $1.479 < |\eta| < 3.0$ , and the ES in the region  $1.653 < |\eta| < 2.6$ . Lead tungstate ( $\text{PbWO}_4$ ) crystals are used throughout. This type of crystal permits rapid feedback: 80% of light produced through scintillation is emitted within 25 ns, the design LHC bunch spacing. The short radiation length results in a high-granularity system, allowing precise measurement of the electromagnetic shower. The crystals are polished to maximize total internal reflection of light within the crystals, and thus ensure optimal functioning conditions for the photodetectors. The layout of the ECAL is illustrated in Fig. 2.6 [29].

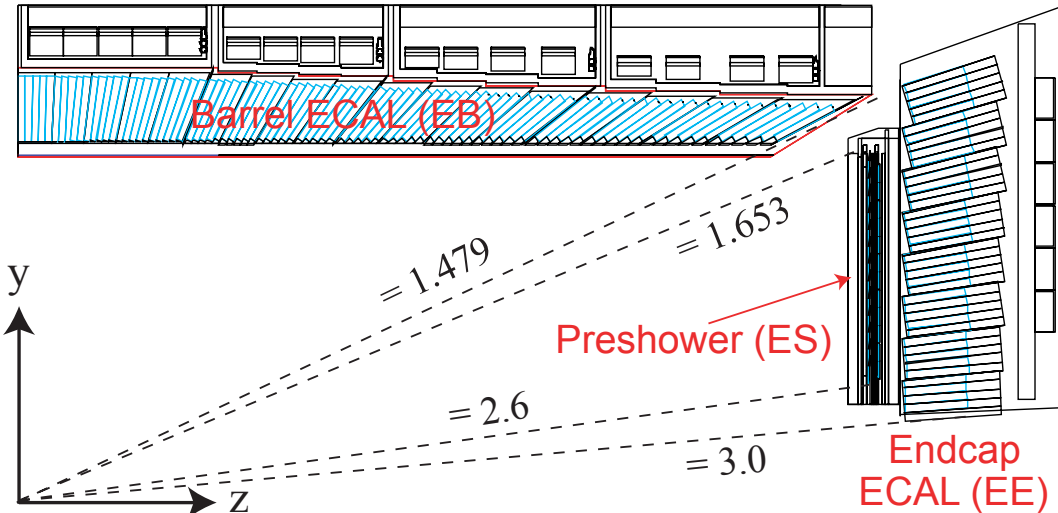


Figure 2.6: View of one quarter of the CMS electromagnetic calorimeter (ECAL) in the  $r - z$  plane.

The EB has an inner radius of 129 cm. It is segmented into 360 regions in  $\phi$  and  $2 \times 85$  regions in  $\eta$ , for a total of 61 200 crystals. At the inner radius the front face of the crystals have area  $22 \times 22 \text{ mm}^2$ , while the rear face measures

$26 \times 26 \text{ mm}^2$ ; the length of the crystals is 230 mm. The crystals are placed in alveolar structures called submodules, which are then assembled into modules made up of between 400 and 500 crystals. Different types of modules are produced for different  $\eta$  regions. In order to avoid crystal edges, and hence cracks, aligned with the trajectories of particles emanating from the interaction point, the crystals are tilted by  $3^\circ$  in both  $\eta$  and  $\phi$  directions. Ensembles of four modules are joined by an aluminium web to create supermodules of 1 700 crystals. Overall there are 36 identical supermodules that each stretch across half the barrel length, with each supermodule spanning  $20^\circ$  in  $\phi$ . Read-out is performed by pairs of silicon avalanche photodiodes (APD) of active area  $5 \times 5 \text{ mm}^2$  that are attached to the rear face of each crystal.

The EE are located at  $|z| = 314 \text{ cm}$  on either side of the interaction point. The disks are divided into two D-shaped sections (Dees). Each Dee is composed of  $5 \times 5$  arrays of identical crystals called supercrystals, also housed in alveolar structures; in total there are 3 662 crystals organized into 138 supercrystals and 18 partial supercrystals located around the circumference of the Dees. In the EE the crystals are of length 220 mm with front faces of area  $28.6 \times 28.6 \text{ mm}^2$  and rear faces of area  $30 \times 30 \text{ mm}^2$ ; they are segmented in  $x - y$  and arranged in a rectangular grid. Single vacuum phototriodes (VPT) of active area  $\approx 280 \text{ mm}^2$  are mounted on the backs of crystals for read-out.

The ES detectors are located in front of the EE disks over the range  $1.653 < |\eta| < 2.6$ , and are 20 cm thick. The detectors also have a Dee structure, with elements having the same orientation as those in the EE. The ES is composed of two layers of lead radiators that are backed by silicon strip detectors, which measure shower shapes and energy deposits. The lead components are matched to the

neighboring EE crystals for optimal performance. The silicon sensors are composed of 32 strips with 1.9 mm pitch, have a thickness of 320  $\mu\text{m}$ , and an active area of  $61 \times 61 \text{ mm}^2$ . The strips in the second plane are mounted orthogonally to those in the first plane; by design approximately 95% of incident photons begin to shower in the first layer. Unit elements composed of one sensor, read-out electronics, and a support structure, are called micromodules. Groupings of seven, eight or ten micromodules connected to an electronics motherboard form a ladder, and ladders are affixed to the lead radiators. There are approximately 4 300 micromodules overall, corresponding to 137 000 read-out channels.

The performance of the ECAL is quantified by its energy resolution, which was measured in electron test beams [31] and found to be:

$$\left(\frac{\sigma_E}{E}\right)^2 = \left(\frac{2.8\%}{\sqrt{E}}\right)^2 + \left(\frac{0.415}{E}\right)^2 + (0.30\%)^2,$$

where the energy is measured in GeV. In these measurements electrons were incident on a central crystal and the deposited energy was measured in the surrounding  $3 \times 3$  crystal array. In order to maintain this resolution the temperature in the ECAL is closely monitored. The operating temperature is 18°C, motivated in part by the need to minimize radiation damage to the crystals, with a  $\pm 0.05^\circ\text{C}$  window dictated by temperature-sensitive factors such as the light output of the crystals. A water-cooling system is used to dissipate heat in the ECAL.

#### 2.2.2.2 Hadronic calorimeter

The HCAL completes the ECAL system in that it measures energy deposits from hadronic jets, collimated structures of particles resulting from the hadronization

of quarks and gluons, and missing transverse energy ( $E_T^{\text{miss}}$ ), which is the one essential characteristic of classic SUSY signatures, as discussed in Section 1.4.5. The HCAL occupies the space between the ECAL and solenoid. It must withstand high radiation and particle fluxes, and be constructed from non-magnetic materials in order to not impact the field produced by the magnet. For optimal performance it was designed to be hermetic, covering the range  $|\eta| < 5.0$ , and to maximize the amount of absorbing material inside the magnet coils. It is constructed from brass plates and tiles of plastic scintillator material. The emitted light is read out using multi-pixel hybrid photodiodes (HPD) that are connected to the scintillator material by a combination of wavelength-shifting (WLS) fibers and clear fibers.

The HCAL is composed of barrel (HB) and endcap (HE) sections, forward calorimeters (HF), and a “tail-catcher” outer section (HO) located beyond the magnet coils. The HB covers the range  $|\eta| < 1.4$  while the endcaps are installed in the range  $1.3 < |\eta| < 3.0$ . The HF extends forward coverage in  $2.9 < |\eta| < 5.2$  and the HO increases coverage in the region  $|\eta| < 1.26$ . The layout of the HCAL is illustrated in Fig. 2.7 [32].

The HB extends between  $r = 1.77 \text{ m}$  and  $2.95 \text{ m}$ , respectively the outer edge of the ECAL and the inner edge of the magnet, and is composed of two half-barrels (HB+ and HB-). These are in turn comprised of 36 identical azimuthal wedges that are each divided into four  $\phi$  sectors. The wedges are made of two external stainless steel support and 14 inner brass absorber plates. The inner and outer steel plates have thicknesses of 40 mm and 75 mm, respectively; there are successively eight 50.5 mm and six 56.5 mm brass plates in between. The brass plates, which are 30% zinc and 70% copper, contribute an absorber thickness

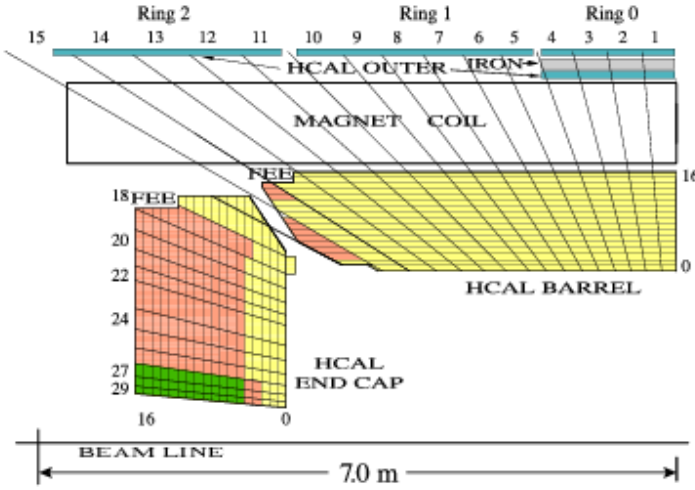


Figure 2.7: Layout of one quarter of the CMS hadronic calorimeter (HCAL) in the  $r - z$  plane.

varying between approximately six and ten interaction lengths, depending on  $\eta$ . In order to avoid holes the plates are assembled such that the different layers are staggered in  $\phi$ . The layers of plates alternate with tilings of plastic scintillator material that are 9 mm thick for the external plates and 3.7 mm thick for the remaining plates, with the first layer located in front of the inner steel plate. In each  $\phi$  segment the scintillator is divided into 16 different  $\eta$  regions called towers that produce an overall  $(\Delta\eta, \Delta\phi) = (0.087, 0.087)$  segmentation. Tiles are assembled into units called trays that span a  $\phi$  segment; there are 108 trays per scintillator layer. Grooves are machined in the tiles, and showers produced in each tile are read out by a WLS fiber. At the edge of the tile, the WLS fiber is spliced with a clear fiber that runs to an optical connector at the end of the tray, from which an optical fiber carries the signal to an HPD for read-out.

The HE are situated on either side of the HB, and their design is similar to the barrel system. In this system also, brass plates are assembled in a staggered

fashion. The plates are 79 mm thick and are interspersed with 9 mm gaps filled by tiles of plastic scintillator material. Each HE is composed of 20 196 tiles organized into 1368 trays. There are 36  $\phi$  wedges called megatiles, and 32 towers of varying  $\eta$  width in each megatile, for a total of 2304 towers. The segmentation of the HE is  $(\Delta\eta, \Delta\phi) = (0.087, 0.087)$  in the region  $1.3 < |\eta| < 1.6$  and  $(\Delta\eta, \Delta\phi) \approx (0.17, 0.17)$  for  $1.6 < |\eta| < 3.0$ . External stainless steel support plates of thickness 10 cm frame this structure. Read-out is performed in the same manner as in the HB.

The HO is installed outside of the magnet coils in the region  $|\eta| < 1.3$  to compensate for the shorter depth of interacting material in the central region of the detector, in which there is not enough space inside the volume of the solenoid to capture the full hadron shower. The HO geometry is constrained by the magnet return yoke and muon detector structures. The iron return yoke consists of five rings of length 2.5 m that are numbered  $-2, -1, 0, +1, +2$  and arranged along the  $z$  axis, with the HO representing the innermost absorbing layer. The central ring comprises two 19.5 cm-thick iron layers at  $r = 3.82$  m and 4.07 m, each placed in between two layers of plastic scintillator material; the remaining rings are composed of only one layer of iron surrounded by plastic scintillators, at  $r = 4.07$  m. In the central region the HO increases the absorber depth to over ten interaction lengths, similar to that in more forward regions. Following the distribution of the muon systems, each ring is composed of 12 identical  $\phi$  sectors interleaved with material belonging to the return yoke and muon systems. The  $\phi$  sectors are further divided into six slices that lay in a common plane. The subdivision of each slice in  $\eta$  defines a tile, with tiles in one slice assembled in a tray. The tray length matches the muon ring length in  $z$ . The  $\eta, \phi$  segmentation and resulting tower structure are designed to align with

the HB geometry. Each of the six trays per  $\phi$  sector are composed of five tiles in rings  $\pm 2$ , six tiles in rings  $\pm 1$ , and 8 tiles in ring 0, for a total of 72 trays in the internal layer of ring 0 and 360 trays for all other layers and rings, and 2730 tiles overall. Read-out is also performed via WLS and clear fibers steered through optical connectors to photodetectors. Simulation of incident pions confirmed the reduction in leakage in the central region, while QCD dijet events were used to verify the improvement in  $E_T^{\text{miss}}$  resolution with the HO.

The HF is designed to cover the forward pseudorapidity range  $3.0 < |\eta| < 5.0$ . It is cylindrically shaped with an inner radius of 12.5 cm, and extends to  $r = 130.0$  cm, with the face closest to the interaction point located at  $z = 11.2$  m. Due to its proximity with the beam line and resulting high particle fluxes as well as radiation, the HF makes use of a different technology than the other HCAL components: 5 mm-thick steel absorber plates separated into 13 concentric rings and threaded through by quartz fibers, for an overall absorber depth of 165 cm. In order to distinguish signals produced by electrons and photons, which shower over short distances, from those generated by hadrons, half the fibers cover the full absorber length while the other half, measuring 1.43 m, begin 22 cm past the inner face of the HF. Alternating long and short fibers of width 0.6 mm, arranged parallel to the beam, are organized in a 5.0 mm square lattice. A signal is registered when incident particles originating from a shower emit Cherenkov radiation in a fiber. The rings are separated into azimuthal wedges spanning  $10^\circ$  ( $20^\circ$ ) in the outermost 11 (innermost two) rings, and into towers measuring  $\Delta\eta = 0.175$ , except in the innermost ring where  $\Delta\eta = 0.300$  and the outermost ring for which  $\Delta\eta = 0.111$ ; fibers are arranged in bundles within each tower. The detector is placed in a hermetic radiation shield made of 40 cm-thick layers of steel and concrete and an additional 5 cm-thick layer of polyethylene

designed to protect the read-out devices and electronics. The quartz fibers are connected to light guides (phototubes) that extend through part of the radiation shield, and terminate in photomultiplier tubes (PMT). Read-out from the long and short fibers is performed in separate channels; groups of 24 PMTs are used for read-out of a single half-wedge.

The energy resolution of the HCAL has been measured in combination with that of the ECAL [33, 34], leading to the following parameterization:

$$\left(\frac{\sigma_E}{E}\right)^2 = \left(\frac{a}{\sqrt{E}}\right)^2 + b^2,$$

where the energy is measured in GeV, and parameters  $a$  and  $b$  are  $\sim 2 \text{ GeV}^{1/2}$  and  $\sim 0.07$ , respectively.

### 2.2.3 Superconducting solenoid

Charged particles traveling in a static magnetic field have a helical trajectory with a bending radius at a given momentum that is inversely proportional to the field strength. In addition the reconstructed trajectory can be used to calculate a particle's charge-to-mass ratio. Thus high magnetic fields can be used to obtain excellent momentum resolution as well as discriminate between particles and their antiparticles.

The CMS experiment makes use of a 3.8 T magnetic field delivered by a superconducting solenoid to achieve its performance goals of  $\Delta p/p \approx 10\%$  momentum resolution and resolving the sign of  $1 \text{ TeV}/c$  muons. The magnet and associated cryogenic system form a 12.5 m-long cylindrical structure of diameter 6.3 m that is centered on the beam pipe; a return yoke is used to confine the magnetic flux.

The magnet distinguishes itself from solenoids used in previous experiments by the energy it is capable of storing and the high mechanical deformation it must withstand. The system was therefore designed to be self-supporting. The solenoid is constructed from mechanically reinforced NbTi Rutherford cables with an aluminium insert; these are wound into four layers, with 2168 turns total. The inductance of the magnet is 14.2 H, and operated at a current of 19 kA it stores 2.6 GJ of energy. The magnet coils are separated into five rings of cryogenic modules, for a total weight of 220 t; the system is operated at 5 K.

The return yoke (barrel and endcaps) is made of 10 kt of iron, thus constituting the bulk of the detector. It is situated outside the magnet volume, and is interleaved with the muon detectors. The barrel part is also divided into five cylindrical segments, numbered YB  $-2, -1, 0, +1, +2$ , beginning at the far end of the  $z$  axis and going towards increasing  $z$ . In addition to confining the magnetic flux, the iron also serves as an absorber for hadronic matter.

## 2.2.4 Muon systems

The muon detectors were designed to maximize muon identification capabilities, which are essential in order to measure Higgs decays to four muons via a pair of  $Z^0$  bosons, for example. Following the structure of the inner detector layers, the muon systems are composed of a cylindrical barrel section and two flat endcaps on either side of the barrel. The total detector area is approximately 25 000 m<sup>2</sup>; the muon systems must therefore be robust and inexpensive. Three types of gaseous detectors are used. These systems are described below.

Drift tubes (DT) are employed in the barrel region, where the intensity of

the magnetic field, mostly confined by the return yoke, and the particle flux are low; they cover the range  $|\eta| < 1.2$ . In the endcap regions the particle flux, comprising muons as well as other types of particles, is higher and the magnetic field is non-uniform and of higher intensity, leading to the choice of cathode strip chambers (CSC). These extend  $|\eta|$  coverage between 0.9 and 1.2. The DT and CSC systems are augmented by resistive plate chambers (RPC), which provide secondary position measurements, albeit with a lesser resolution, as well as fast response times, in both barrel and endcap regions. RPCs cover the range  $|\eta| < 1.6$ . The layout of the different systems is illustrated in Fig.2.8 [29].

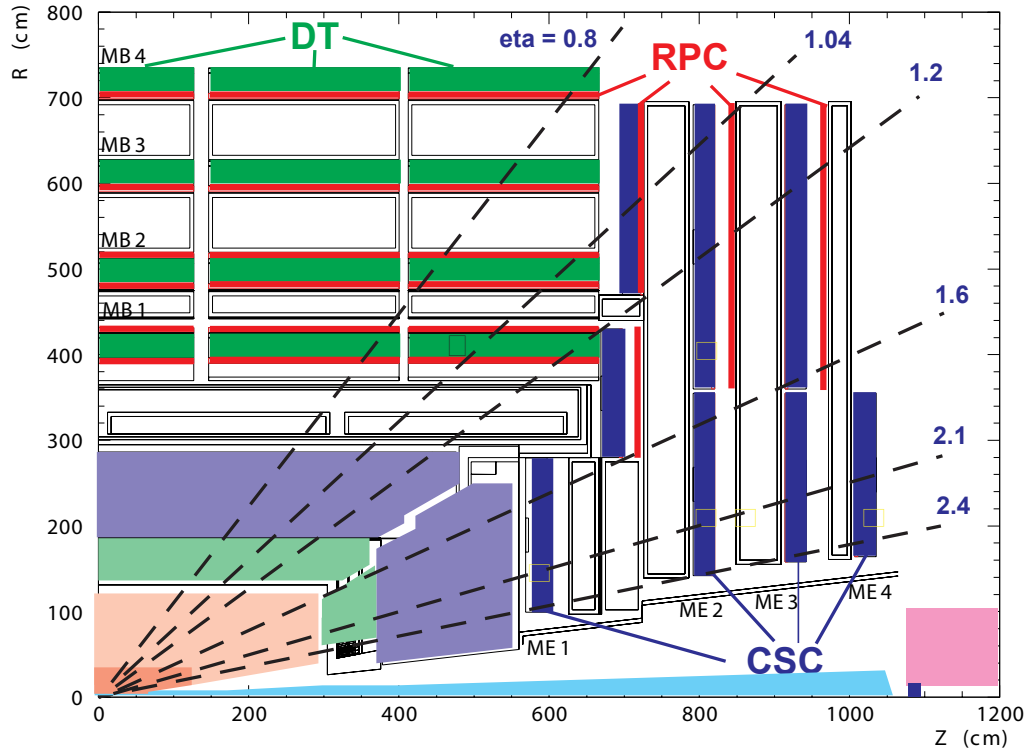


Figure 2.8: Layout of one quarter of the CMS muon systems: drift tubes (DT), cathode strip chambers (CSC), and resistive plate chambers (RPC), in the  $r - z$  plane.

#### 2.2.4.1 Drift tubes

Part of the Muon Barrel (MB) system is made of drift tube chambers. Each sensor is composed of a gas-filled tube, whose walls are grounded, containing a wire that is kept at a high potential. Particles traveling through the system ionize the gas; the resulting charges are collected and produce a current in the wire that is proportional to the initial particle's energy. In combination with high-precision timing, the position of incoming particles with respect to the wire can be inferred. DTs can therefore be used to measure the energy and position of incident muons.

As in the magnetic field return yoke, the DTs are separated into five rings, or wheels, that are centered on the beam pipe. Within wheels the rectangular DT chambers are organized into four concentric cylindrical layers, called stations, that are interspersed with the return yoke. The stations are numbered MB 1–4. Each wheel is divided into 12 identical  $\phi$  sectors that are numbered starting with the sector centered at  $\phi = 0$ , and increasing with  $\phi$ .

Within the stations MB 1–3 (MB 4) are 12 (eight) layers of DTs organized into three (two) units called superlayers (SL), consisting of four neighboring layers. In order to minimize dead zones, tubes are staggered by a half-tube length in each SL. In the innermost stations MB 1–3 the outer SLs, in which wires are oriented parallel to the beam line, measure a track's position in  $\phi$  while the middle SL, in which wires are perpendicular to the beam line, measures its  $z$  position. Only the  $\phi$  coordinate is measured in the outer station MB 4. An aluminium honeycomb plate is inserted between the innermost SL and the outer SL(s), thus providing mechanical support. Each SL provides a time resolution of a few nanoseconds, allowing for the attribution of measurements to individual

bunch crossings.

Each tube is filled with a gas mixture of argon (Ar) and carbon dioxide ( $\text{CO}_2$ ). Field electrodes, made from an aluminium sheet, are glued to an insulating mylar sheet and set on the inner and outer faces of the drift cells. A gold-plated stainless steel wire of length  $\sim 2.4\text{ m}$  and diameter  $50\,\mu\text{m}$  serves as the anode. Cathodes are built following the same design as the field electrodes and provide insulation from external grounded aluminium plates. Wires are held at  $+3\,600\text{ V}$ , while electrode strips and cathodes are held at  $+1\,800\text{ V}$  and  $-1\,200\text{ V}$ , respectively.

A DT unit, the SL, is formed from aluminium plates, with cells (drift tubes) of width 42 mm placed in between I-shaped support structures (I-beams); the spacing between sheets is 13 mm. These values were chosen because they represent a compromise between granularity and number of active channels. The wires and electrodes are powered by high voltage supplies mounted to the aluminium plates. SLs are then glued to the honeycomb support plate to form individual DT chambers. There are 60 (70) such chambers in the MB 1–3 (MB 4) stations, for a total of 250 chambers per wheel and approximately 172 000 sensitive wires summed over wheels.

The spatial resolution associated with a signal registered in a single wire is  $250\,\mu\text{m}$ , with an angular resolution of approximately 1 mrad. Combined with tracker information, DTs increase the resolution for muons that register in both subsystems.

#### 2.2.4.2 Cathode strip chambers

The Muon Endcap (ME) system is comprised in part of cathode strip chambers, another type of proportional sensor. One unit consists of a gas-filled enclosure criss-crossed with orthogonal anode wires and cathode strips. An incident muon ionizes the gas, prompting electrons to move towards the anode and ions towards the cathode. The resulting charges and their positions on the wires and strips are measured. Two sets of coordinates are thus measured, allowing for the computation of the center of gravity of the charges. Charges are distributed across multiple cathode strips, increasing the detector resolution.

There are 468 CSCs divided between the two endcaps, organized into four rings numbered ME 1–4 towards increasing  $|z|$ . The rings are separated into radial groupings of three, two, two, and one trapezoid-shaped chambers, respectively. Each chamber covers between  $10^\circ$  and  $20^\circ$  in  $\phi$ . The chambers overlap in order to provide full  $\phi$  coverage, and span  $0.9 < |\eta| < 2.4$ . Muons with  $0.9 < |\eta| < 1.2$  are measured by both DTs and CSCs, while muons with  $1.2 < |\eta| < 2.4$  cross between three and four CSCs. Additional coverage is also provided for muons with  $|\eta| < 1.6$  by RPCs, described below.

The CSCs are multi-wire proportional chambers consisting of seven radially-oriented copper cathode sheets segmented into strips, and six azimuthally-oriented gold-plated tungsten anode wires. These provide  $\phi$  and  $r$  coordinate measurements, respectively. The wire spacing is approximately 3.2 mm, and the spacing between the cathode strips creates 9.5 mm-high gas gaps. The chambers are filled with a mixture of Ar, CO<sub>2</sub> and CF<sub>4</sub>. The largest chambers have dimensions of  $1.5 \times 3.4 \text{ m}^2$ . The overall sensitive area of the CSC system is  $5000 \text{ m}^2$ , for a total of approximately  $2 \times 10^6$  wires.

Each chamber provides a spatial resolution on the order of  $200\,\mu\text{m}$ , while the angular resolution is approximately 10 mrad.

#### 2.2.4.3 Resistive plate chambers

Resistive plate chambers are used throughout the muon barrel and endcap systems in order to supplement measurements from the DTs and CSCs. They consist of a gas-filled enclosure delimited by parallel plates, one anode and one cathode. Incident muons ionize the gas, creating an electron avalanche. The resulting charged particles migrate towards the two types of plates depending on their charge. In addition to sensible spatial resolution even in a high-rate environment (up to  $1\,\text{kHz}/\text{cm}^2$ ), RPCs provide nanosecond timing resolution, ensuring that a trigger system relying on these detectors will unambiguously assign a signal to a specific bunch crossing all but a fraction of the time.

One unit consists of a double-gap structure made from plates a high-resistivity plastic, bakelite, separated by a 2 mm-wide gas gap. RPC modules consist of two such units. The small gas gap width guarantees the excellent timing resolution. Modules of different shapes are used in the barrel and endcap muon systems. There are a total of 610 RPCs in the barrel and endcaps combined.

In the barrel, RPCs are organized into four concentric stations that are numbered RB 1–4 with increasing  $r$ . In the two inner stations, the RPCs are located on the internal and external faces of the corresponding DT stations, while in the outer stations the RPCs are located on the internal face of the corresponding DT stations. The barrel RPCs are approximately 2.5 m long, oriented parallel to the

beam pipe, and between 1.5 and 2.5 m wide.

Endcap RPCs are separated into three layers, RE 1–3, that are mounted on a single face of the iron return yoke endcap disks. The rings are subdivided into three concentric rings of trapezoidal chambers. Each segment spans between  $10^\circ$  and  $20^\circ$  in  $\phi$ , with segments overlapping in order to minimize dead zones on the edges of the chambers. The endcap RPCs extend dual coverage (by two different types of muon detectors) to  $|\eta| < 1.6$ , with plans to extend to  $|\eta| < 2.1$ .

### 2.2.5 Trigger and data acquisition

At the LHC’s design bunch spacing of 25 ns, the event rate is 40 MHz. However, a large fraction are simple pp scattering events that are unlikely to result in the type of physics the LHC is meant to probe; these events are therefore discarded. Combined with write-out and storage limitations, a rejection rate of  $\sim 10^6$  is necessary. The trigger and data acquisition (DAQ) systems address this need. Triggering is divided into two sub-systems that make successive decisions using increasingly detailed data read out by the front-end electronics of the different sub-detectors. These are the Level-1 (L1) trigger and the High-Level Trigger (HLT).

The L1 trigger is responsible for lowering the rate to approximately 100 kHz, before further processing by the HLT. In order to make fast decisions, it uses only low-granularity data from the calorimetry and muon systems. For trigger purposes, the ECAL and HCAL are divided into towers, constructed from blocks of ECAL crystals and corresponding HCAL towers, which are read out together. The muon systems supply track candidates as well as timing informa-

tion used to identify bunch crossings. Trigger-primitive objects, i.e., electrons, muons, photons, or jets above a certain threshold, as well as the total  $E_T$  and  $E_T^{\text{miss}}$  in the event, are constructed from these data. Logical expressions formed from the number, energy and momentum of the various trigger-primitive objects are then evaluated. The final decision of the L1 is expressed as an OR of all the algorithms, or bits. For example, the triggers used in this thesis require the presence of two leptons (either electrons or muons), with the leading lepton  $p_T$  above 17 GeV and sub-leading lepton  $p_T$  above 8 GeV. The L1 trigger is built using custom hardware, and has a latency of  $3.2\,\mu\text{s}$ . During this time, high-resolution data from the full detector read-out is held in front-end memory pipelines.

The HLT reduces the output rate  $\sim 100\,\text{Hz}$ . If an event passes the L1 trigger, the full detector read-out is sent to front-end read-out buffers, and onto a processor residing in a  $\sim 1000$ -node farm of commercial-grade processors, via a switching network. The HLT comprises multiple levels of decisions that are based on increasingly complex and CPU-intensive physics reconstruction and selection steps. This allows the system to efficiently reject events before performing a more complex analysis of potentially interesting event.

First, high-resolution data from the calorimetry and muons systems are used; partial tracker information from hits in the pixel detector are then added; the last level employs the full tracker read-out and track reconstruction using algorithms that are similar to the final offline reconstruction. At each step, selection requirements are applied to the reconstructed physics objects, followed by a decision to keep the event for further reconstruction and analysis, or to reject the event. In the latter case, events are entirely discarded. The HLT software

follows a structure similar to the L1 trigger, with multiple trigger paths defined and the event saved if it passes at least one of these. The overall runtime per event is of order 1 s [35], and the stored event size is 1.5 MB on average.

## CHAPTER 3

### EVENT RECONSTRUCTION

In this chapter we describe how particles are reconstructed from the information collected in the sub-detectors presented in Chapter 2. We wish to reconstruct events containing  $\tilde{b}$  squarks that decay to a top quark and a light flavor quark. Top quarks decay almost exclusively to a b quark and W boson, and the W boson can decay either hadronically, to a  $q\bar{q}$  pair, or leptonically, to a lepton and neutrino. Neutrinos interact extremely weakly with matter and escape undetected, resulting in a momentum imbalance in the plane transverse to the beam direction, or  $E_T^{\text{miss}}$ .

We therefore focus on the techniques used to reconstruct quarks, leptons, and  $E_T^{\text{miss}}$ . In order to accurately identify these different types of particles, CMS relies on an algorithm that exploits the full detector read-out to reconstruct all stable particles produced in proton-proton collisions, i.e., electrons, muons, photons, charged hadrons, and neutral hadrons. Higher-order objects such as jets (including b-tagged jets) and  $E_T^{\text{miss}}$  are then reconstructed using the full list of particles, thus providing a global event description. This algorithm is described in Section 3.1.

Full event reconstruction begins with the identification of tracks, which are the signature of charged particles in the detector; and vertices, which correspond to either interactions between quarks within colliding protons (primary vertices), or decays of particles produced in collisions (secondary vertices). Primary vertex reconstruction is detailed in Section 3.2. Of particular interest for the analysis presented in Chapter 4 are particles produced in the decays of sbottoms. We first detail the reconstruction of electrons and muons in Sections 3.3

and 3.4, before turning to the description of jets and missing transverse energy in Section 3.5.

### 3.1 Particle Flow

The Particle Flow (PF) algorithm has been documented in detail [36,37]. A short summary of the algorithm, as it pertains to this thesis, is presented below. By combining information from all the different sub-detectors, the PF algorithm aims to provide a precise determination of the type, momentum, and direction of all stable particles produced in a proton-proton collision. This is made possible by the high magnetic field, fine granularity, and near-hermeticity of the CMS detector.

The inputs to the PF algorithm are tracks from charged particles, which are reconstructed in the pixel and strip tracker; clusters of energy deposits in the ECAL and HCAL; and muon tracks reconstructed in the muon chambers. Simultaneous high reconstruction efficiencies and low fake rates in these subsystems are necessary to guarantee the performance of the method. A linking algorithm is used to form blocks, composed of a track and/or a calorimeter cluster and/or a muon track, which are then assumed to originate from a single particle. Particle species are identified in a certain order; blocks are removed once they have been successfully linked and before proceeding to the next candidate type.

First, PF muons are constructed from compatible muon tracks and tracker tracks. PF electrons are then built from tracks and ECAL clusters, along with any neighboring deposits attributed to radiated Bremsstrahlung photons. Next,

the remaining tracks are matched to energy-compatible ECAL and HCAL clusters to construct PF charged hadrons. Any remaining cluster energy in excess of the track energies is used to build PF photons and neutral hadrons. Lastly, PF photons and neutral hadrons are constructed from any remaining unlinked calorimeter clusters.

The techniques used to reconstruct objects that are relevant for this thesis are described in the following sections.

## 3.2 Tracks and vertices

### 3.2.1 Tracks

Track reconstruction begins with a clusterization step, in which hit clusters are formed from hits in the pixel and strip tracker. The clusters comprise estimates of the cluster position and associated uncertainty. An iterative method is then used to reconstruct tracks. First, tracks seeds are constructed and extrapolated from to form track trajectories. The extrapolation assumes in a first estimate that the magnetic field is uniform in the tracker volume, producing helical track trajectories. Track fitting is then performed using a combinatorial Kalman filter [38]. Lastly, high-quality tracks are selected and corresponding hits removed, before proceeding to the next iteration, progressively loosening the seeding criteria.

Tracks seeds are generated from either pairs or triplets of hits in different layers of the tracker. An iterative pattern recognition procedure, based on a

Kalman filter <sup>1</sup>, is then applied. The filter is initialized with a track seed and the associated pixel and strip hits, estimates of track parameters ( $p_T$ ,  $\eta$ ,  $\phi$ , and impact parameters in the transverse and longitudinal planes), and their covariance matrix. Following the initialization, the track trajectory is extrapolated to the next detector layer. The predicted trajectory is compared with hits in this layer; one trajectory candidate per potential matching hit is created, as well as one trajectory candidate without a hit in the layer (corresponding to a fake, or “invalid”, hit).

Track parameters and their covariance matrix are updated with information from the new hit, and a mean of the predicted trajectory and the hit, weighted by their uncertainties, is assigned to each candidate. Only the candidates passing certain selection requirements are extrapolated to the next layer, where the effect of interactions with material at the sensor surface are taken into account before advancing to the next iteration. This procedure is carried out until the outermost detector layer is reached.

Finally, the Kalman filter method is applied to the output list of hits, now taking into account the non-uniformity of the magnetic field. In addition, a smoothing filter is implemented, proceeding iteratively back to the interaction region, and allowing for hits not found in prior iterations to be associated with track candidates. This results in a final, more precise estimate of the track parameters.

At each iteration, selection requirements are applied. With default values noted in parentheses, these include the maximum number of track candidates propagated at each step (5); the maximum value of the  $\chi^2$  measuring the con-

---

<sup>1</sup>A Kalman filter performs a linear least-squares minimization, assuming Gaussian fluctuations for the parameters.

sistency of a hit with the predicted trajectory (30); whether to include invalid hits (yes); the maximum consecutive invalid hits (1); the minimum track  $p_T$  (0.9 GeV); the minimum number of hits per track (5). These parameters can be tuned to work within the different constraints of the HLT, governed by CPU time, and offline level, where high reconstruction efficiency is the goal.

The efficiency to reconstruct muons in the range  $1 < p_T < 100$  GeV is above 97% throughout most of the tracker  $\eta$  range, with a decrease to  $\sim 75\%$  occurring in the forward region, close to the edge of the pixel detector. For pions in the same  $p_T$  range, the efficiency is lower because of interactions with the tracker material, but still above 70% (80% for  $10 < p_T < 100$  GeV).

### 3.2.2 Vertices

After track reconstruction, vertices are reconstructed to determine the point of origin of the corresponding particles. For a given track collection, tracks are clustered to form compatible vertex candidates, and a fit is used to determine the vertex position, its uncertainty, and the associated track parameters, as well as a measure of the goodness of the fit.

Beginning with all reconstructed tracks in an event, tracks are preselected based on the number of pixel and strip hits, the normalized track  $\chi^2$ , and transverse impact parameter with respect to the interaction region (beamspot). Tracks are then grouped into clusters depending on their  $z$  coordinate at the distance of closest approach to the beamspot.

An adaptive vertex fitter [39], also based on the Kalman filter method, and

which is robust to contamination from tracks originating from different vertices, is employed. It consists of an iterative least squares fit in which tracks are assigned a weight between 0 and 1, according to their consistency with the vertex. Tracks not consistent with the vertex are recursively removed, and the fit converges when all the tracks in the cluster are consistent at a certain (user-defined, adjustable) level with originating from the vertex.

Reconstructed vertices are ordered by  $\sum_{\text{tracks}} p_T^2$ , where the sum runs over tracks associated with the vertex. The highest vertex is assumed to correspond to the hard interaction in the event.

### 3.3 Electrons

The reconstruction of electrons draws upon information collected in the electromagnetic calorimeter, the pixel detector, and the strip tracker. As an electron travels through interacting material in the tracker, it radiates bremsstrahlung photons. The 3.8 T magnetic field, which bends the trajectory of the electron, results in an electromagnetic shower that deposits energy into multiple ECAL crystals distributed along  $\phi$ . The difficulty lays in estimating the energy and momentum of the initial electron.

An electron candidate consists of a collection of energy deposits, or “super-cluster”, in the ECAL, which is matched to one track that is identified as originating from a primary vertex. The reconstruction proceeds in multiple steps.

First, clustering algorithms are used to identify super-clusters. In the barrel the algorithm searches in  $1 \times 3$  or  $1 \times 5$  arrays in  $\eta$  for energy clusters in the  $\phi$

direction, thus building  $3 \times 3$  or  $5 \times 5$  crystal arrays. In the endcaps the algorithm starts from a crystal with a local maximum in deposited energy and searches in  $\phi$ , then in  $\eta$ , for an edge at which the energy stops decreasing, thus creating  $5 \times 5$  crystal arrays. Both algorithms then form super-clusters from blocks of clusters in a  $\sim 0.3$  rad-wide  $\phi$  strip. The position of a super-cluster is defined as the energy-weighted average of the constituent cluster positions.

A matching step then attempts to pair a super-cluster with a track. The position of the super-cluster is extrapolated inwards to the interaction region. Expected hits in the pixel detector are computed and compared to existing hits. If two such hits are found in different layers of the pixel detector, electron track candidates are constructed using a dedicated algorithm. Instead of the Kalman filter technique detailed in Section 3.2.1, a non-linear filter, the Gaussian-sum filter (GSF) [40], must be used to account for non-Gaussian fluctuations introduced by bremsstrahlung radiation of the electron; these are modeled by a sum of Gaussian terms. Seeds consisting of a pair of pixel hits are used to initialize the filter.

Electron candidates must furthermore satisfy pre-selection requirements: track and super-cluster are required to match in  $\phi$  and  $\eta$ , as well as in energy and momentum; and the energy deposited in the hadron calorimeter tower immediately behind the super-cluster must be less than 20% of the super-cluster energy. These help reduce the rate of misidentification of a jet as an electron. Analyses such as this thesis are concerned with prompt leptons, i.e., those produced by the hard interactions in proton-proton collisions. In this context, electrons are therefore additionally required to be consistent with originating from the hard interaction vertex.

The efficiency to reconstruct electrons from super-clusters is presented in Fig. 3.1 [41] as a function of super-cluster  $E_T$  in different ranges of super-cluster  $\eta$ . Above  $E_T$  of 20 GeV the efficiency is found to be greater than  $\sim 90\%$  across the range of the ECAL,  $|\eta| < 2.5$ .

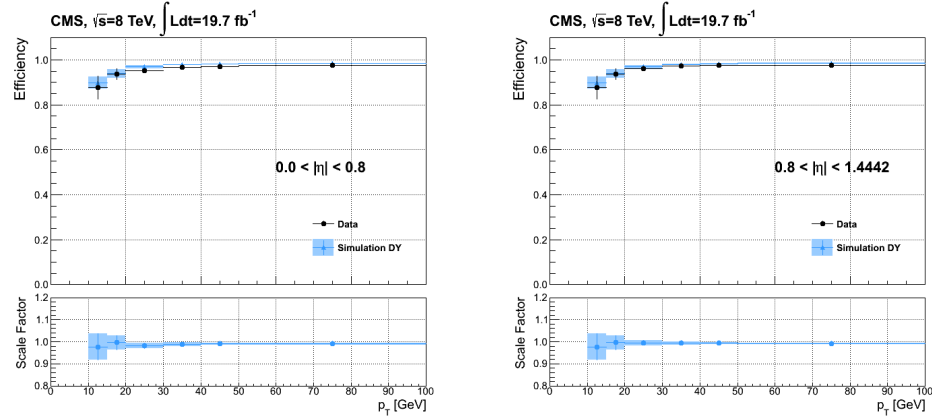


Figure 3.1: Electron reconstruction efficiency in data (black points) and simulation (blue points) in different super-cluster  $\eta$  regions as a function of super-cluster  $E_T$ . The bottom panel shows the corresponding data-to-simulation scale factors. The blue shaded area represents the total systematic uncertainty on the prediction in simulation. Left:  $0 < |\eta| < 0.8$ . Right:  $0.8 < |\eta| < 1.4442$ .

### 3.4 Muons

Muon reconstruction proceeds in multiple steps, beginning with a local reconstruction at the detector level, using only data collected in the muon chambers (CSC, DT, RPC) in which hits were measured. For DTs, segment candidates are constructed from a linear fit to aligned hits, in different DT layers, that are found to be consistent with originating from the nominal interaction region. In CSCs, strip hits are clustered and a linear fit is performed to build track segments. RPC

strips are clustered and the position of hits determined.

Next, “stand-alone” muon candidates are built using a Kalman filter and the full muon system read-out. The input seeds are track segments, produced during local reconstruction, in the innermost muon stations. The segments are then extrapolated outwards, taking into account interactions in the detector material and the effect of the magnetic field. The procedure terminates at the outermost muon station, at which point a second Kalman filter is applied in the reverse direction. Lastly, track candidates are extrapolated backwards to the interaction region, and a vertex-constrained fit is performed to obtain final estimates of the track parameters and their associated uncertainties.

Finally, information from the pixel detector and strip tracker is incorporated to construct “global” muons. A stand-alone muon is extrapolated inwards from the innermost muon station, accounting for the possibility of scattering and interactions with detector material. Potential matching hits in the different layers of the silicon detector are used to define a region in which tracks are reconstructed with a Kalman filter technique, following the method outlined in Section 3.2.1. In the final smoothing step, hits in the muon chambers are included. In order to maintain the reconstruction efficiency in the TeV- $p_{\mathrm{T}}$  range, muon candidates are subsequently rejected by a selection on the track fit  $\chi^2$ . This technique allows for the detection of large energy losses before the first muon station is reached.

The reconstruction efficiency for stand-alone and global muons with  $p_{\mathrm{T}}$  between 10 GeV and 1 TeV is expected to be greater than 98% throughout the majority of the  $\eta$  range covered by the muon systems,  $|\eta| < 2.5$ ; the  $p_{\mathrm{T}}$  resolution is between a few tenths and a few %. For global muons with a  $p_{\mathrm{T}}$  of 100 GeV, the

rate of charge misidentification is below 0.1%. The reconstruction efficiency for PF muons is presented as a function of muon  $p_T$  in Fig. 3.2 [42] in data and simulation. For muons with  $p_T$  above 10 GeV the reconstruction efficiency is nearly 100% in the range  $|\eta| < 2.4$ .

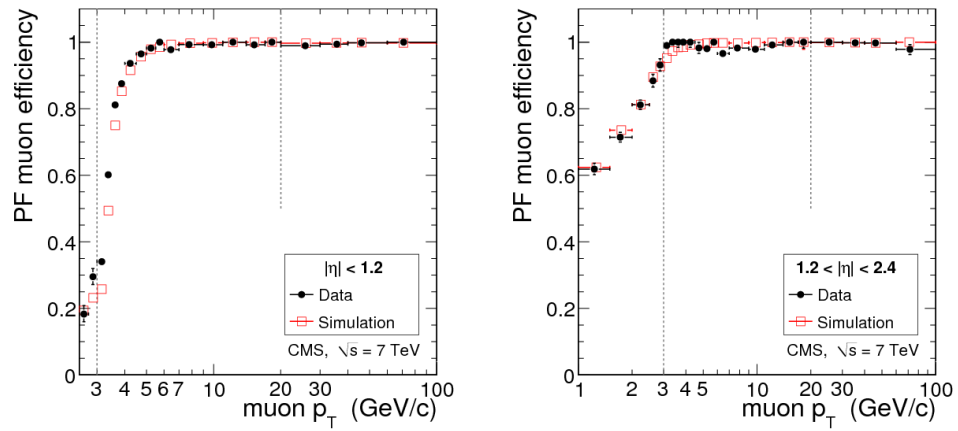


Figure 3.2: Reconstruction and identification efficiency of Particle Flow muons with a reconstructed tracker track in different  $\eta$  ranges in data (black points) and simulation (red squares) as a function of muon  $p_T$ . Left:  $0 < |\eta| < 1.2$ . Right:  $1.2 < |\eta| < 2.4$ .

### 3.5 Jets and missing transverse energy

The full list of candidates – electrons, muons, photons, charged hadrons, and neutral hadrons – reconstructed by the PF algorithm are used to build higher-level objects such as jets and  $E_T^{\text{miss}}$ .

### 3.5.1 Jets

Due to its large cross section, multijet production, or QCD, is the dominating physics process at the LHC. The differential cross section for dijet production has been measured in bins of the maximum jet rapidity  $|y_{\max}|$  and the mass of the dijet system  $M_{jj}$  [43], and found to be  $\sim 10^2 \text{ pb/GeV}$  for  $|y_{\max}| < 0.5$  and  $M_{jj} \sim 300 \text{ GeV}$ . Integration over bins yields an overall cross section on the order of  $10^{10} \text{ pb}$ , many orders of magnitude larger than the cross section for top quark pair production, which is  $\sim 250 \text{ pb}$  at  $8 \text{ TeV}$  [44]. QCD results in the production of quarks and gluons, hereafter referred to as partons. Color confinement dictates that singlet quark states cannot exist. Instead, quarks (and gluons) undergo hadronization, in which  $q\bar{q}$  pairs are generated from the vacuum. This process creates hadrons, particles composed of either two or three quarks. Interactions lead to the creation of a shower of collimated particles, known as jets.

PF candidates are combined using the anti- $k_t$  clustering algorithm [45] to construct jets. The algorithm proceeds as follows. For a given candidate  $i$  the distance measures  $d_{ij}$ , and  $d_{iB}$  between  $i$  and the beam  $B$ , are calculated. These are defined as:

$$d_{ij} = \min \left( \frac{1}{k_{t,i}^2 k_{t,j}^2} \right) \frac{\Delta_{ij}^2}{R^2},$$

$$d_{iB} = \frac{1}{k_{t,i}^2},$$

with  $k_{t,i}$ ,  $y_i$ , and  $\phi_i$  respectively the transverse momentum, rapidity, and azimuthal angle of the  $i^{\text{th}}$  particle, and  $\Delta_{ij}^2 = (y_i - y_j)^2 + (\phi_i - \phi_j)^2$ . The minimum runs over all other candidates  $j \neq i$ . Within CMS the radius parameter is chosen to be  $R = 0.5$ .

Next, the distances  $d_{ij}$  and  $d_{iB}$  are compared. If  $d_{ij} < d_{iB}$ , candidates  $i$  and  $j$

are combined into one; otherwise element  $i$  is labeled a jet and removed from the list of candidates. The procedure is repeated until no candidates remain. A jet is therefore constructed starting from a high-energy particle, and particles are clustered into a cone of finite size  $R$ .

A complete understanding of the jet four-momentum as it relates to that of the underlying parton is crucial in order to include jets in physics analyses. Jet constituents can be classified according to the species of the corresponding PF candidates; charged hadrons have been measured to account for 65% of the total jet energy, while photons and neutral hadrons carry 15% and 20%, respectively [37]; electron and muon contributions were found to be negligible. Jet resolution therefore depends upon the performance of the tracker, ECAL, and HCAL systems, and is limited by the non-linearity and non-uniformity of each sub-detector's response. The limiting factor in reconstructing the jet energy is the HCAL resolution.

The jet energy calibration procedure and determination of the transverse momentum resolution is described in Ref. [46]. A correction factor relates the four-momenta of the measured jet and “true” jet, i.e., reconstructed in Monte Carlo simulation using the above clustering algorithm on the collection of stable particles originating from the underlying parton and particles arising from pile-up:

$$p_\mu^{\text{corrected}} = \mathcal{C}(p_T^{\text{measured}}, \eta) \cdot p_\mu^{\text{measured}}. \quad (3.2)$$

The correction factor is factorized into multiple components, which address both the offset and jet response. For PF jets the response is already close to one. First, an offset correction factor is applied to subtract eventual additional energy in the jet originating from pile-up. It is a function of the jet area in the  $y-\phi$  plane, and the event-specific  $p_T$  area density  $\rho$ , from which the contribution

from pile-up has been subtracted.

A Monte Carlo correction factor is then applied to account for the difference between measured and generated jet energy; this restores the uniformity in  $\eta$  and linearity in  $p_T$ . Finally, residual corrections are applied to correct for any remaining differences in the jet energy scale in data and simulation. A relative correction is used to resolve the  $\eta$  discrepancy, while an absolute correction adjusts the  $p_T$ .

For PF jets within  $|\eta| < 2.0$  the uncertainty on the jet energy scale is below 3% above 30 GeV, and for jets within  $|\eta| < 4.0$  the uncertainty is at most 5%. The  $p_T$  resolution is better than 10% for jets within detector acceptance and with  $p_T < 1$  TeV, as shown in Fig. 3.3 [47].

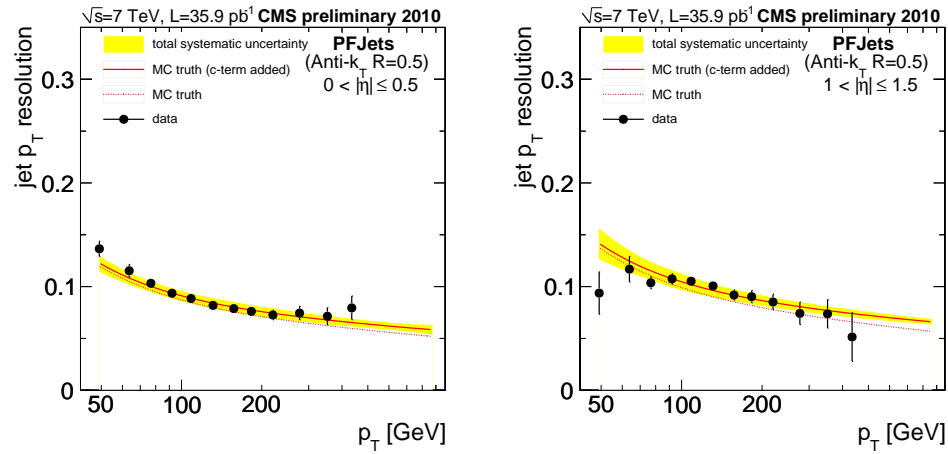


Figure 3.3: Resolution on the transverse momentum of Particle Flow jets in data (black points) compared to the true resolution in simulation (red dashed line) and the resolution in simulation after applying a data-to-simulation correction factor (red line) in different  $\eta$  ranges as a function of jet  $p_T$ . Left:  $0 < |\eta| < 0.5$ . Right:  $1 < |\eta| < 1.5$ .

### 3.5.2 Missing transverse energy

Missing transverse energy arises from neutral weakly interacting particles, such as neutrinos, that escape CMS undetected. The presence of these particles is inferred from the eventual transverse momentum imbalance in an event. In the context of the PF algorithm,  $E_T^{\text{miss}}$  is simply defined as the modulus of the negative vector sum, over all PF candidates, of the momentum in the plane transverse to the beam.

Events with real  $E_T^{\text{miss}}$ , i.e., arising from invisible particles, must be distinguished from events without such particles but in which a mismeasurement induces fake  $E_T^{\text{miss}}$ . For example, a badly mis-measured jet results in fake  $E_T^{\text{miss}}$  aligned with the jet axis (in the opposite direction if the jet is over-estimated, and vice versa). In multi-jet events, the  $E_T^{\text{miss}}$  resolution can be modeled as having a Gaussian core. As a function of the scalar sum over PF particles of transverse energies, the width was found to vary between 5 and 10 GeV over the range 50 to 350 GeV, as shown in Fig. 3.4 [48].

Type-I  $E_T^{\text{miss}}$  corrections corresponding to the propagation of jet energy corrections, described in Section 3.5.1, are generally applied.

## 3.6 b-tagging

The reconstruction and identification of jets originating from b quarks is especially important in top quark physics, due to the near-exclusive decay  $t \rightarrow W b$ ; and searches for new physics that couple strongly to third-generation SM particles. Both are of interest in this thesis. Techniques for reconstructing b-quark jets

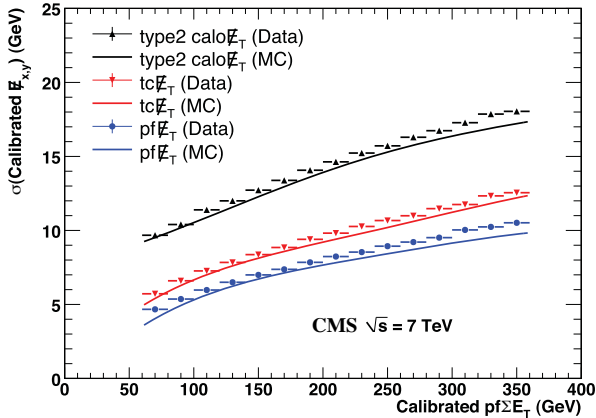


Figure 3.4: Missing transverse energy resolution, assuming a Gaussian distribution, as a function of the scalar sum over Particle Flow particles of transverse energies, for different  $E_{\text{T}}^{\text{miss}}$  reconstruction algorithms. The blue points show the results for the PF algorithm in data while the blue line corresponds to the performance of the PF algorithm in simulation.

rely on the long lifetime of b hadrons, and associated flight distance  $\sim 450 \mu\text{m}$ , resulting in secondary vertices (SV) that are displaced from the primary hard interaction vertex (PV); the high mass of b hadrons; the multiplicity of charged particles produced in b hadron decays (five on average); and the high energy of the b hadrons themselves, resulting in collimated jets.

Different algorithms have been developed in CMS to identify b-quark jets. We briefly describe below the Combined Secondary Vertex (CSV) algorithm [49–51], which was used in the analysis that is the subject of this thesis. It relies on a multi-variate technique.

Inputs for b quark identification are tracks and PF jets. Secondary vertices are reconstructed within jets with an adaptive vertex fitter [39], using a subset of high-quality tracks built following the technique outlined in Section 3.2.1.

In particular, tracks are selected based on the impact parameter at the point of closest approach of the track to the jet axis. The three-dimensional impact parameter (IP), whose sign is given by the relative orientation of the jet direction and the vector pointing from the primary vertex to the point of closest approach of the track, is expected to be positive for tracks corresponding to charged particles produced in the decay of a b hadron traveling along the jet direction; for prompt tracks it can have either sign.

If no SVs are reconstructed following the above procedure, an attempt is made to form pseudo-vertex candidates, using at least two tracks not compatible with the PV, and with a signed transverse IP significance  $d_{xy}/\sigma_{d_{xy}}$  greater than two. Otherwise no vertices can be reconstructed. In order to reduce contamination, only the vertices with fewer than 65% of tracks shared with the primary vertex are considered.

Nine variables enter in the construction of the CSV discriminator: the vertex category, the invariant mass, rapidity, and multiplicity of charged particles associated with the SV, the jet track multiplicity, the fraction of energy carried by SV tracks relative to all tracks in the jet, the significance of the flight distance in the transverse plane, the three-dimensional IP significance of the SV tracks, and the transverse IP significance of the SV track, where the track collection has been ordered by transverse IP significance.

These variables are combined using a likelihood ratio technique. Due to the significant differences in the distributions of the above variables for b quarks, c quarks and light-flavor (u, d, s) or gluon jets, three categories are defined. The discriminating variable is:

$$d_{\text{CSV}} = f_c \cdot \frac{\mathcal{L}^b}{\mathcal{L}^b + \mathcal{L}^c} + f_{\text{LF}} \cdot \frac{\mathcal{L}^b}{\mathcal{L}^b + \mathcal{L}^{\text{LF}}},$$

where the relative fraction of c and light flavor partons in jets not originating from a b quark are  $f_c \simeq 0.25$  and  $f_{LF} \simeq 0.75$ , respectively. The likelihood ratios are defined using as:

$$\mathcal{L}^{b,c,LF} = f^{b,c,LF}(\alpha) \prod_i f^{b,c,LF}(x_i),$$

where  $\alpha$  denotes the vertex category,  $x_i$  represents the variables entering the discriminator calculation, and  $f^{b,c,LF}$  are the probability density functions for these variables. The discriminator has values between zero and one, with higher values representing more b-like jets.

The efficiency to correctly identify b-quark jets (b-tagging efficiency) and the probability to misidentify a c-quark or light-flavor jet as a b-quark jet (mistag rate) are a function of  $d_{CSV}$ . Loose, medium, and tight working points are defined to correspond to approximately 10%, 1%, and 0.1% mistag rates. At the medium working point ( $d_{CSV} = 0.679$ ) the b-tagging efficiency is  $\sim 70\%$  for jets with  $p_T$  between 80 and 120 GeV [50]. The b-tagging efficiency is presented in Fig. 3.5 as a function of jet  $p_T$  and  $\eta$  for this algorithm and working point.

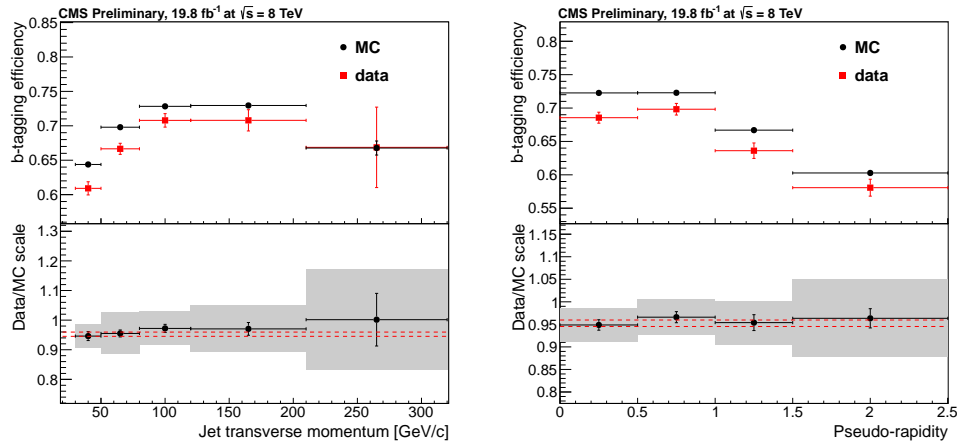


Figure 3.5: Efficiency to correctly identify b-quark jets with the medium working point of the Combined Secondary Vertex algorithm. Data are shown in red and simulation results in black. The bottom panel shows the corresponding data-to-simulation correction factors, with the shaded area representing the total statistical and systematic uncertainties and the dashed line showing the statistical uncertainty on the average scale factor values.

## CHAPTER 4

## ANALYSIS

### 4.1 Introduction

#### 4.1.1 Motivation

The subject of this thesis is a search targeting the  $R$ -parity violating SUSY model described in Section 1.5. In particular, we focus on sbottom ( $\tilde{b}$ ) squark decays. The analysis is constructed to measure the  $\tilde{b}$  mass and production cross section, in case of discovery, and set limits on  $\tilde{b}$  production otherwise.

The decays of  $\tilde{b}$  squarks overwhelmingly produce a top quark and a light-flavor quark. Assuming the  $\tilde{b}$  particles are pair-produced in proton-proton collisions, two top quarks and two jets originating from light quarks are produced. Top quarks decay almost exclusively to a  $b$  quark and  $W$  boson, and the  $W$  boson can decay either hadronically, to a  $q\bar{q}$  pair, or leptonically, to a lepton and neutrino. Although the branching fraction favors hadronic  $W$  decays, in the interest of obtaining a good resolution on the eventual  $\tilde{b}$  mass measurement, we study the leptonic decay channel. The Feynman diagram for this channel is presented in Fig. 4.1.

We therefore search for pairs of  $\tilde{b}$  squarks produced in proton-proton collisions, that each decay to a light flavor quark,  $b$  quark, lepton and neutrino. The final state consists of two light jets, two  $b$ -tagged jets, two leptons, and  $E_T^{\text{miss}}$  due to the two neutrinos escaping the detector.

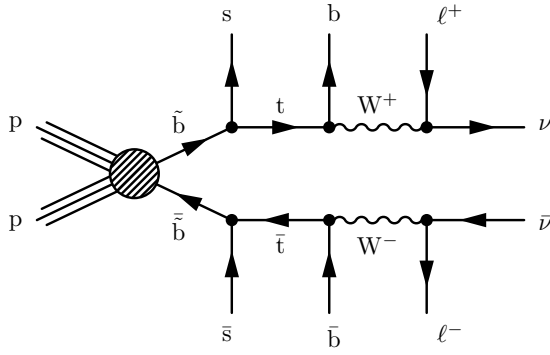


Figure 4.1: Leading order Feynman diagram for  $R$ -parity violating sbottom squark pair production.

### 4.1.2 Analysis strategy

We search for  $\tilde{b}$  squarks with the goal of extracting the particle's mass in case of a discovery, and setting limits on the production cross section otherwise. With this aim in mind, we attempt to reconstruct the full  $\tilde{b}$  particle decay chain, from neutrino to top quark to  $\tilde{b}$  candidate.

First we use a kinematic method to reconstruct the four-momenta of neutrinos originating from the leptonic decay of  $W^\pm$  bosons. We then combine the neutrinos with the visible decay products of the  $\tilde{b}$  particles, i.e., leptons,  $b$ - jets, and light flavor jets. This technique allows us to fully reconstruct the  $\tilde{b}$  candidate four-momenta, modulo pairing ambiguities. Eliminating the ambiguity would require being able to distinguish between jets originating from  $b$  and  $\bar{b}$  quarks.

Once the resonance reconstruction method is implemented, we perform a shape analysis. We use the reconstructed resonance mass and the leading and second leading light jet  $p_T$  spectra to distinguish signal from background. These distributions are presented in Fig. 4.2 for background SM processes and

a 500 GeV  $\tilde{b}$  squark, illustrating the discriminating power of the three variables. The signal and SM background yields have been normalized, using theoretical cross sections, to the integrated luminosity in data. In addition, the signal distribution has been scaled upwards by a factor of five in order to better visualize its contribution.

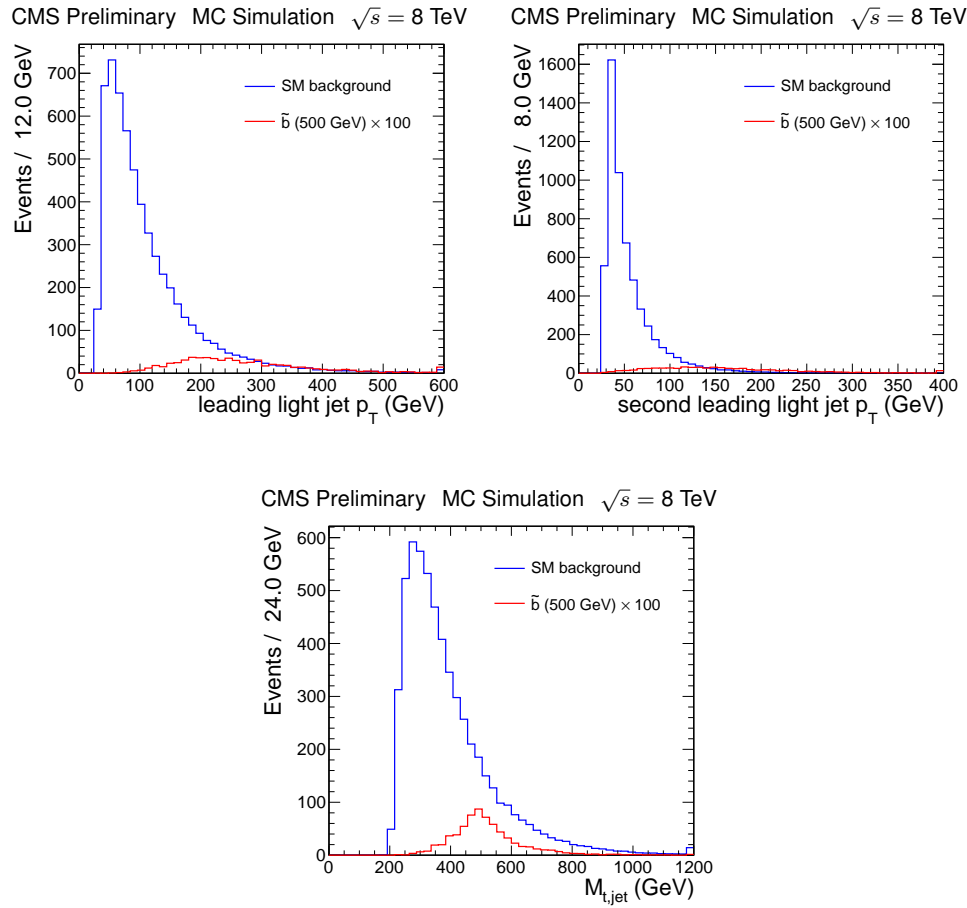


Figure 4.2: Variables used for discriminating signal from background in the search for  $\tilde{b}$  squark pairs. Top row: transverse momentum of the leading (left) and second-leading (right) light flavor jets. Bottom: reconstructed  $\tilde{b}$  resonance mass.

We parameterize the distributions of the reconstructed resonance mass and

the leading and sub-leading light jet  $p_T$  in signal and background, and use the parameterizations to construct an unbinned extended maximum likelihood which we then fit to data. We extract the overall normalization from the data in a background-dominated control region. Finally we calculate confidence intervals on the signal cross section.

This strategy presents several advantages. First, it is independent of SM background simulation and thus is not sensitive to issues of MC generators and settings or mismodeling effects. Second, the shape analysis is more powerful than a simple cut and count analysis in that it allows us to extract the mass of the new particle in the case that one is discovered.

We first present the data and simulation samples used in this analysis in Section 4.2, and the object and event selections in Section 4.3. We discuss signal and background discrimination in Section 4.4. Sources of systematic uncertainty are investigated in Section 4.5. We then describe the statistical model we employ in Section 4.6. Finally we present and interpret our results in Section 4.7.

## 4.2 Data and simulation samples

### 4.2.1 Data

We analyze data collected by the CMS experiment at 8 TeV in 2012, using dilepton triggers, and corresponding to an integrated luminosity of  $19.5 \text{ fb}^{-1}$ . Events are classified into three categories,  $\mu\mu$ ,  $ee$  or  $e\mu$ , depending on the trigger stream in which they are selected. We use trigger paths designed to collect events with

two leptons ( $e$  or  $\mu$ ) that satisfy loose identification requirements and with  $p_{\mathrm{T}}$ s above 17 and 8 GeV for the leading and sub-leading leptons, respectively. The primary datasets and associated integrated luminosities used in this analysis are listed in Table 4.1.

The event selection described in Section 4.3 includes a requirement on the lepton  $p_{\mathrm{T}}$  such that the triggers are nearly fully efficient. In simulated signal events passing the final selection, the trigger is more than 95% efficient for  $\tilde{b}$  squark masses in the entire range studied (250 to 600 GeV).

### 4.2.2 Simulation

Simulation is essential in order to understand signal and background physics processes at colliders, the resulting kinematics, physical observables, and their signatures within a detector, as well as the detector performance. We use Monte Carlo (MC) generators to simulate production of  $\tilde{b}$  pairs and SM background processes in proton-proton collisions. Event generation is performed in multiple steps, before being passed through a full detector simulation.

First the hard interaction in a collision, between a parton in one incoming proton and a parton in the other colliding proton, is simulated relying on the knowledge of Parton Distribution Functions (PDF). These tell us the probability that a parton carries a certain fraction of an incoming particle’s momentum. Next the emission of colored particles by the incoming and outgoing partons in the hard interaction, called initial- and final-state radiation (ISR and FSR, respectively), is modeled. This stage is known as the parton shower step, and is followed by the hadronization of colored particles into observable states, hadrons.

Table 4.1: Dataset names and integrated luminosities.

Dataset	$L_{int}$ ( $\text{pb}^{-1}$ )
/DoubleElectron/Run2012A-13Jul2012-v1/AOD	806.2
/DoubleElectron/Run2012A-recover-06Aug2012-v1/AOD	82.3
/DoubleElectron/Run2012B-13Jul2012-v1/AOD	4447
/DoubleElectron/Run2012C-24Aug2012-v1/AOD	495.0
/DoubleElectron/Run2012C-PromptReco-v2/AOD	6394
/DoubleElectron/Run2012C-EcalRecover_11Dec2012-v1/AOD	134.3
/DoubleElectron/Run2012D-PromptReco-v1/AOD	7273
<hr/>	
/DoubleMu/Run2012A-13Jul2012-v1/AOD	806.2
/DoubleMu/Run2012A-recover-06Aug2012-v1/AOD	82.5
/DoubleMu/Run2012B-13Jul2012-v4/AOD	4383
/DoubleMu/Run2012C-24Aug2012-v1/AOD	480.6
/DoubleMu/Run2012C-PromptReco-v2/AOD	6358
/DoubleMu/Run2012C-EcalRecover_11Dec2012-v1/AOD	134.2
/DoubleMu/Run2012D-PromptReco-v1/AOD	7273
<hr/>	
/MuEG/Run2012A-13Jul2012-v1/AOD	806.2
/MuEG/Run2012A-recover-06Aug2012-v1/AOD	82.5
/MuEG/Run2012B-13Jul2012-v1/AOD	4446
/MuEG/Run2012C-24Aug2012-v1/AOD	495.0
/MuEG/Run2012C-PromptReco-v2/AOD	6396
/MuEG/Run2012C-EcalRecover_11Dec2012-v1/AOD	134.2
/MuEG/Run2012D-PromptReco-v1/AOD	7273

The following step consists of simulating sub-leading interactions between the remaining constituents of the hadrons participating in the hard interaction, referred to as the underlying event. Finally, the unstable hadrons produced in the hard interaction are decayed into stable states.

Simulation samples corresponding to distinct processes, such as  $Z^0$  boson or top quark pair production, are produced. In order to compare the simulation to data, simulated events are weighted by a sample-specific factor meant to normalize the MC to the integrated luminosity  $L_{\text{int}}$  in data,

$$w_i = \frac{\sigma_i L_{\text{int}}}{N_i},$$

where  $\sigma_i$  is the cross section of the process simulated in the  $i^{\text{th}}$  sample and  $N_i$  is the number of generated events in the  $i^{\text{th}}$  sample.

#### 4.2.2.1 SM backgrounds

The dominant background to the  $\tilde{b}$  signal originates from SM top quarks pair-produced in association with ISR or FSR jets. The leading-order Feynman diagrams for these processes are presented in Fig. 4.3. Other SM processes account for a small ( $\approx 5\%$ ) contribution; they are single-top production ( $\approx 2\%$ ), Drell–Yan production ( $\approx 2\%$ ), diboson production, and top pair production in association with vector bosons.

MC simulation of top quark pair production, Drell–Yan production, and  $t\bar{t}$  production in association with vector bosons ( $W^\pm/Z^0$ ) was performed in MADGRAPH 5 [52]. Single top production was simulated using POWHEG [53] and TAUOLA [54]. Samples of diboson production ( $W^\pm W^\pm$ ,  $W^\pm Z^0$  and  $Z^0 Z^0$ ) were generated using PYTHIA 6 [55].

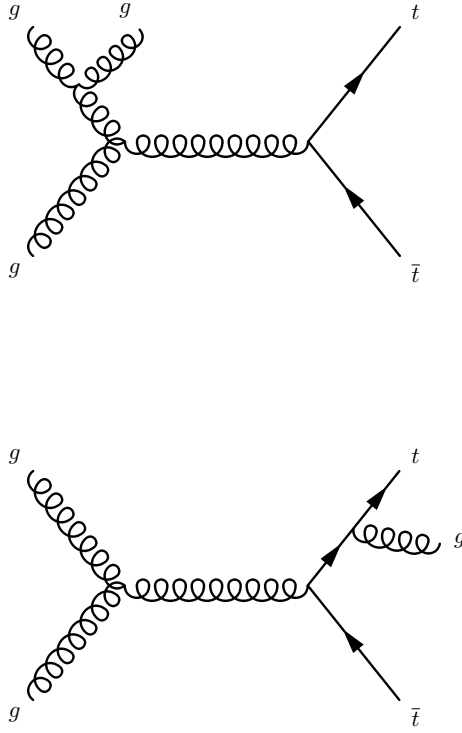


Figure 4.3: Leading-order Feynman diagrams for SM top quark pair production at a proton-proton collider, in association with an additional radiated jet. Top: initial-state radiation (ISR). Bottom: final-state radiation (FSR).

The full list of MC samples of SM processes is presented in Table 4.2, along with the cross sections used to normalize the samples to the recorded integrated luminosity.

#### 4.2.2.2 Signal

Pair production of  $\tilde{b}$  squarks in proton-proton collisions was simulated with the help of the Minimal Supersymmetric Model with  $R$ -parity Violation (RPV MSSM) implemented in FeynRules [56]. The RPV MSSM model was in-

Table 4.2: Simulation samples of SM background processes used for comparisons to data.

SM process	Generator	Cross Section (pb)	Equivalent $\mathcal{L}$ ( $\text{fb}^{-1}$ )
$t\bar{t} + \text{jets}$	MADGRAPH	245.8 (CMS)	
$t/\bar{t}$ (s-channel)	POWHEG	3.79/1.76 (approx. NNLO)	
$t/\bar{t}$ (t-channel)	POWHEG	56.4/30.7 (approx. NNLO)	
$t/\bar{t}$ (tW-channel)	POWHEG	11.1/11.1 (approx. NNLO)	
$Z^0 \rightarrow \ell^+ \ell^- + 1 \text{ jet}$	MADGRAPH		43 (NLO)
$Z^0 \rightarrow \ell^+ \ell^- + 2 \text{ jets}$	MADGRAPH		121 (NLO)
$Z^0 \rightarrow \ell^+ \ell^- + 3 \text{ jets}$	MADGRAPH		200 (NLO)
$Z^0 \rightarrow \ell^+ \ell^- + 4 \text{ jets}$	MADGRAPH		273 (NLO)
$W^\pm W^\pm$	PYTHIA	54.8 (NLO)	
$W^\pm Z^0$	PYTHIA	33.2 (NLO)	
$Z^0 Z^0$	PYTHIA	17.7 (NLO)	
$t\bar{t}W$	MADGRAPH	0.232 (NLO)	
$t\bar{t}Z$	MADGRAPH	0.208 (NLO)	
$t\bar{t}WW$	MADGRAPH	0.002037 (NLO)	

terfaced with MADGRAPH 5, where each  $\tilde{b}$  squark was subsequently decayed into a top quark and strange quark. The top quarks were forced to decay leptonically.

The output Les Houches Event Files (LHE) are passed to PYTHIA 8.1 [57] for hadronization, with settings defined in Tune 4C [58], and go through full CMS detector simulation as modeled in GEANT 4 [59]. CTEQ6L PDF sets [60] are used.

Signal samples corresponding to  $\tilde{b}$  masses between 250 and 600 GeV were produced.

## 4.3 Selections

### 4.3.1 Object definitions

Event reconstruction is performed using the Particle Flow technique described in Section 3.1. We use physics objects constructed using charged hadron subtraction (CHS), which mitigates the effect of pile-up. In this method, reconstructed charged hadrons associated with a vertex that is not the primary hard interaction vertex, i.e., a pile-up vertex, are removed. All object collections are mutually exclusive.

In order to reliably identify electrons and muons produced in the hard scatter, we apply a selection requirement on the relative isolation of the lepton, which is defined as

$$I_{\text{rel}} = \frac{\sum_{\text{charged hadrons}} p_T + \sum_{\text{neutral hadrons}} E_T + \sum_{\text{photons}} E_T}{p_T^l},$$

where  $p_T^l$  is the  $p_T$  of the lepton, and the sums run over all PF candidates contained within a cone of radius  $\Delta R$  around the lepton. Leptons originating from the hard scatter are expected to be isolated, with low activity in proximity to the lepton, and therefore have small values of  $I_{\text{rel}}$ .

Objects are identified using the following criteria, which are based on the reconstruction algorithms and quality requirements described in Chapter 3. These

object selections follow the recommendations of the Beyond Two Generations Physics Analysis Group in 2012, and are standard across CMS.

Vertices are required to have:

- ndof of the vertex fit  $> 4$
- longitudinal distance  $|z| < 24\text{ cm}$  and transverse distance  $\rho < 2\text{ cm}$  with respect to the center of the detector

Electrons are identified with a multivariate technique [61]. The candidates are selected to fulfill the following criteria:

- identified as a PF electron
- $p_T > 10\text{ GeV}$  and  $|\eta| < 2.4$
- $|\eta_{\text{scl}}| < 1.4442$  or  $|\eta_{\text{scl}}| > 1.5660$ , in order to exclude electrons with a supercluster in the transition region between barrel and endcap
- GSF track transverse impact parameter  $d_{xy} < 2\text{ mm}$  and longitudinal distance  $|z| < 5\text{ mm}$  with respect to the primary vertex
- photon conversion rejection
- relative PF isolation  $I_{\text{rel}} < 0.15$  using a cone size of  $\Delta R = 0.3$
- MVA-based identification  $> 0.5$

Muons are identified using the “tight” working point described in Refs. [62, 63]. Candidates fulfilling the following criteria are selected:

- reconstructed as a global muon

- identified as a PF muon
- $p_T > 10 \text{ GeV}$  and  $|\eta| < 2.4$
- $\chi^2/\text{ndof}$  of the global muon track fit  $< 10$
- at least one muon chamber hit included in the global muon track fit
- muon segments in at least two muon stations
- tracker track transverse impact parameter  $d_{xy} < 2 \text{ mm}$  and longitudinal distance  $d_z < 5 \text{ mm}$  with respect to the primary vertex
- at least one pixel hit
- at least 5 tracker layers with hits
- relative PF isolation  $I_{\text{rel}} < 0.12$  using a cone size of  $\Delta R = 0.4$

Jets are clustered using the anti- $k_t$  algorithm with a distance parameter  $R = 0.5$ . Inputs are the full collections of PF candidates, following removal of charged hadrons originating from pile-up, and isolated electrons and muons with  $p_T$  above 5 GeV and that are consistent with originating from the primary interaction vertex. The jets must satisfy the following loose requirements:

- $p_T > 30 \text{ GeV}$  and  $|\eta| < 2.4$
- charged hadron fraction  $> 0.0$
- neutral hadron, charged electromagnetic, and neutral electromagnetic fractions  $< 0.99$
- At least two constituents, including at least one charged constituent

These help reduce the fake jet rate from e.g. HCAL noise.

Following the definition in Section 3.5.2, we construct  $E_T^{\text{miss}}$  as the modulus of the negative vector sum of momenta of all PF objects in the event. Jet energy corrections are propagated into the  $E_T^{\text{miss}}$ .

Jets are identified as coming from a b-flavor quark using the Combined Secondary Vertex algorithm described in Section 3.6. We use the following working points in this analysis:

**CSV Loose (CSVL):** 0.244

**CSV Medium (CSVM):** 0.679

These working points correspond to different rates of misidentification of non-b partons [50]. At the loose (medium) working point, the b-tagging efficiency for jets with  $p_T$  between 80 and 120 GeV is approximately 85% (70%), and the misidentification rate is 9.9% (1.4%).

### 4.3.2 Event selection

In order to preferentially select signal-like events, we require that each contain:

- at least 2 good jets passing the CSVL requirement; one of these jets must also pass the CSVM requirement
- at least 2 good jets failing the CSVL requirement
- at least 2 good muons OR at least 2 good electrons OR at least one good muon and one good electron, each with  $p_T > 20 \text{ GeV}$

We additionally require that the invariant mass of the lepton pair be above 15 GeV to veto low-mass resonances, and outside a window around the  $Z^0$  mass of [76 GeV, 106 GeV] if the selected leptons have the same flavor. We hereafter refer to jets passing the CSVL working point discriminator requirement as loose b-jets, and jets passing the CSVM working point discriminator requirement as tight b-jets.

Additional selection cuts defining signal-depleted (control) and signal-rich regions are described in Section 4.4.1.

### 4.3.3 Monte Carlo corrections

Some discrepancies are observed when comparing the raw MC to data. For example, the vertex multiplicity is different in MC and data. This is due to the simulation being produced with a particular pile-up scenario, i.e., a certain average number of pile-up interactions per event. This quantity depends on data-taking conditions. Since producing MC samples with many different pile-up scenarios is computationally prohibitive, the simulation is generated with one such scenario, and reweighted to match the data. The effect of the reweighting is presented in Fig. 4.4, illustrating the need for this particular correction.

The MC is therefore corrected in several ways in order to match the data. The corrections we apply are as follows.

The energy resolution on simulated jets is better than for jets in data, thus jets in simulation must be smeared in order to match the data. The jet energy resolution is corrected following the procedure described in Section 3.5.1.

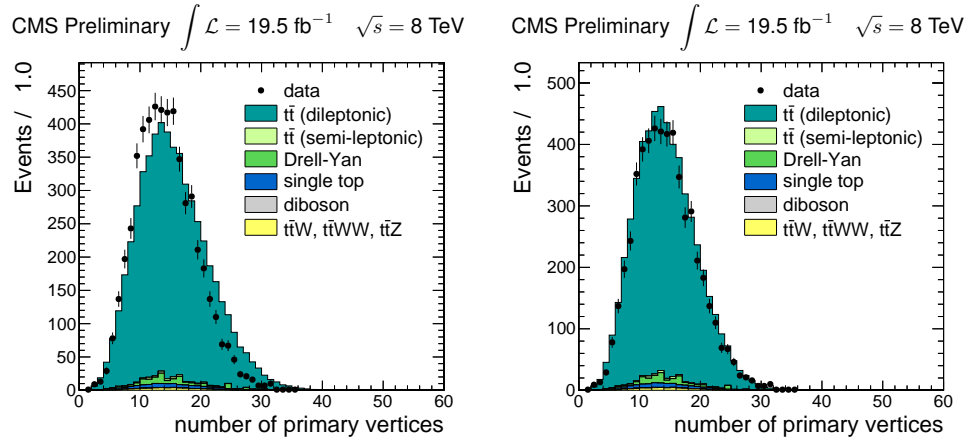


Figure 4.4: Distribution of the vertex multiplicity for vertices satisfying the selection requirements described in Section 4.3.1, in data and SM MC simulation. Left: before reweighting of the SM MC to match the distribution of vertex multiplicity in data. Right: after reweighting.

Tagging efficiencies for light and heavy flavor jets were measured in the  $t\bar{t}$  MC sample found in Table 4.2, in events passing the event selection defined in Section 4.3.2. Standard CMS light and heavy flavor scale factors correcting for the difference in tagging efficiencies between simulation and data were applied [49, 50]. These scale factors range between 0.90 and 0.97.

Lepton reconstruction and isolation scale factors binned in  $p_T$  and  $\eta$  are applied. These have been provided for the datasets listed in Table 4.1. Electron scale factors are taken from Ref. [64], while muon scale factors are documented in Ref. [65].

The simulation is reweighted to match the measured distribution of pile-up vertex multiplicity in data, using the tools described in Ref. [66]. It is also weighted to match a combination of three sets of PDFs: CTEQ, MSTW, and NNPDF.

These factors are all varied within their uncertainties when calculating systematic uncertainties. The complete list of these and all other systematic sources considered can be found in Section 4.5.2.

## 4.4 Signal and background discrimination

Signal events contain pairs of mass resonances that produce top quarks and light jets simultaneously, and the light jets from this decay have a relatively high  $p_T$ . We use both of these properties to discriminate between signal and background.

We parameterize the light jet  $p_T$  and resonant mass spectra in signal and background, relying on simulation to test various shapes. The resulting probability distribution functions are used to construct a likelihood that is fit to data, as described in Section 4.6. We describe below the different distributions chosen to model the light jet  $p_T$  and resonant mass spectra.

### 4.4.1 Light jet $p_T$ spectrum

The  $p_{TS}$  of the leading and second-leading light jets are powerful variables to discriminate between signal and background. The light jet  $p_T$  spectrum in SM processes is almost entirely from ISR or FSR production in  $t\bar{t}$  events. This spectrum is steeply falling and peaks at lower values than the hard jets from signal production, an effect that is compounded at high  $\tilde{b}$  masses. This effect is illustrated in Fig. 4.2. In addition, correlations between light jets may exist in signal, but are unlikely to be present in SM backgrounds.

In this section, we first describe the function chosen to model the two-dimensional light jet  $p_T$  spectrum of the SM background, as well as various closure tests performed in SM simulation. We then present the signal light jet  $p_T$  model.

#### 4.4.1.1 Background model

In order to model ISR and FSR light jet production, we test various steeply falling distributions in SM simulation. We choose a parameterization that fits the simulation well, can be quickly sampled from, and is sufficiently flexible to model the data.

We use a two-dimensional probability density function (pdf)  $\rho_{2D}^{SM}$  to model the spectra of the highest- $p_T$  and second-highest- $p_T$  light jets, denoted  $p_T^{(1)}$  and  $p_T^{(2)}$ , respectively. This distribution is constructed as the sum of three two-dimensional densities  $\rho_i^{2D}(p_T^{(1)}, p_T^{(2)})$ :

$$\rho_{2D}^{SM}(p_T^{(1)}, p_T^{(2)}) = 2 \sum_{i=1}^3 f_i \rho_i^{2D}(p_T^{(1)}, p_T^{(2)}) \Theta(p_T^{(1)} - p_T^{(2)}), \quad (4.1)$$

where  $\Theta$  is the Heaviside step function, which enforces the ordering of the light jets; the parameters  $f_i$  sum to 1; and the factor of two normalizes the pdf. The parameters of this function are determined by maximizing the likelihood defined in Section 4.6 on data.

We factorize each two-dimensional density into one-dimensional densities,

$$\rho_i^{2D}(p_T^{(1)}, p_T^{(2)}) = \rho_i^{\text{jet}}(p_T^{(1)}) \rho_i^{\text{jet}}(p_T^{(2)}), \quad (4.2)$$

and each one-dimensional spectrum has the form:

$$\rho_i^{\text{jet}}(p_T) = \lambda_i \alpha \exp(-\lambda_i p_T^\alpha), \quad (4.3)$$

with  $\alpha$  shared across the three components, while the  $\lambda_i$  differ in each component. This function is chosen because it has the steeply falling spectrum we expect from ISR or FSR jets, and a potentially longer tail than a pure exponential distribution, becoming identical to an exponential distribution if  $\alpha = 1$ .

The two-dimensional density is tested on SM simulation. First we perform a fit to the full SM simulation, allowing  $\alpha$ ,  $\lambda_i$ , and  $f_i$  vary. Figure 4.5 compares observed and predicted yields in the two-dimensional plane defined by the leading and second leading light jet  $p_T$ . Because the observed yield is an event count, while the predicted yield is a probability (the pdf defined in Eq. 4.1 is normalized to one), only the relative distributions are important. An artifact of the ROOT contour finding algorithm is responsible for the large triangle in the right-hand figure. The limited MC statistics produce the jagged edges in the tail of the distribution visible in the left-hand figure. We see that the SM simulation is well modeled by the above two-dimensional density.

Figures 4.6 and 4.7 show one-dimensional projections of the two-dimensional pdf along each light jet  $p_T$  spectrum. We choose to separate the simulation depending on the  $p_T$  of the second leading light jet, because we expect the SM background to populate the lower end of this spectrum, as opposed to the signal. In Fig. 4.6 (4.7), we consider events in which both light jets have  $p_T$  below (above) 50 GeV. Here too, the figures show good agreement between the chosen function and the simulated data.

In order to increase the sensitivity of the analysis, we divide the light jet  $p_T$  spectrum into four regions of second leading light jet  $p_T$ , labeled as one signal-depleted control region (denoted CR), and three signal-enhanced regions (denoted SR1–3). The regions are defined as follows:

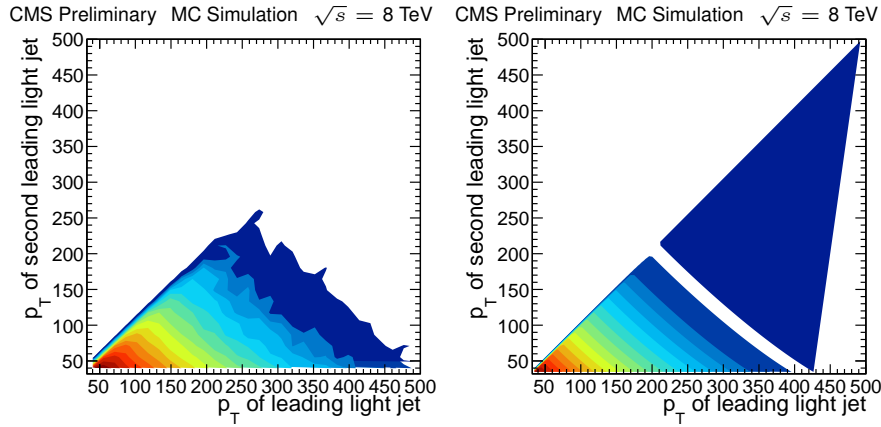


Figure 4.5: Light jet  $p_T$  distributions in SM simulation (left) and the fit to SM simulation (right) in events where both light jets have  $p_T$  above 50 GeV, shown in two dimensions. The distribution defined in Eq. 4.1 is used to fit the two-dimensional light jet  $p_T$  shape. The same logarithmic  $z$  scale is used in both plots.

- Control Region (CR): second leading light jet  $p_T$  between 30 and 50 GeV
- Signal Region 1 (SR1): second leading light jet  $p_T$  between 50 and 80 GeV
- Signal Region 2 (SR2): second leading light jet  $p_T$  between 80 and 110 GeV
- Signal Region 3 (SR3): second leading light jet  $p_T$  above 110 GeV

Almost no signal enters into the control region, and larger amounts of signal enter into the different signal regions, depending on the mass of the  $\tilde{b}$  squark. The binning is also used in constructing the distribution of candidate  $\tilde{b}$  invariant mass, which is described in Section 4.4.2. Each region has different signal and background invariant mass distributions. Since we do not know the analytic correlation between the invariant mass distribution for a  $\tilde{b}$  of a given mass and its light jet  $p_T$  spectrum, we use the above binning to obtain a coarse correlation.

In addition, we fit many unweighted data-sized sub-samples of the SM sim-

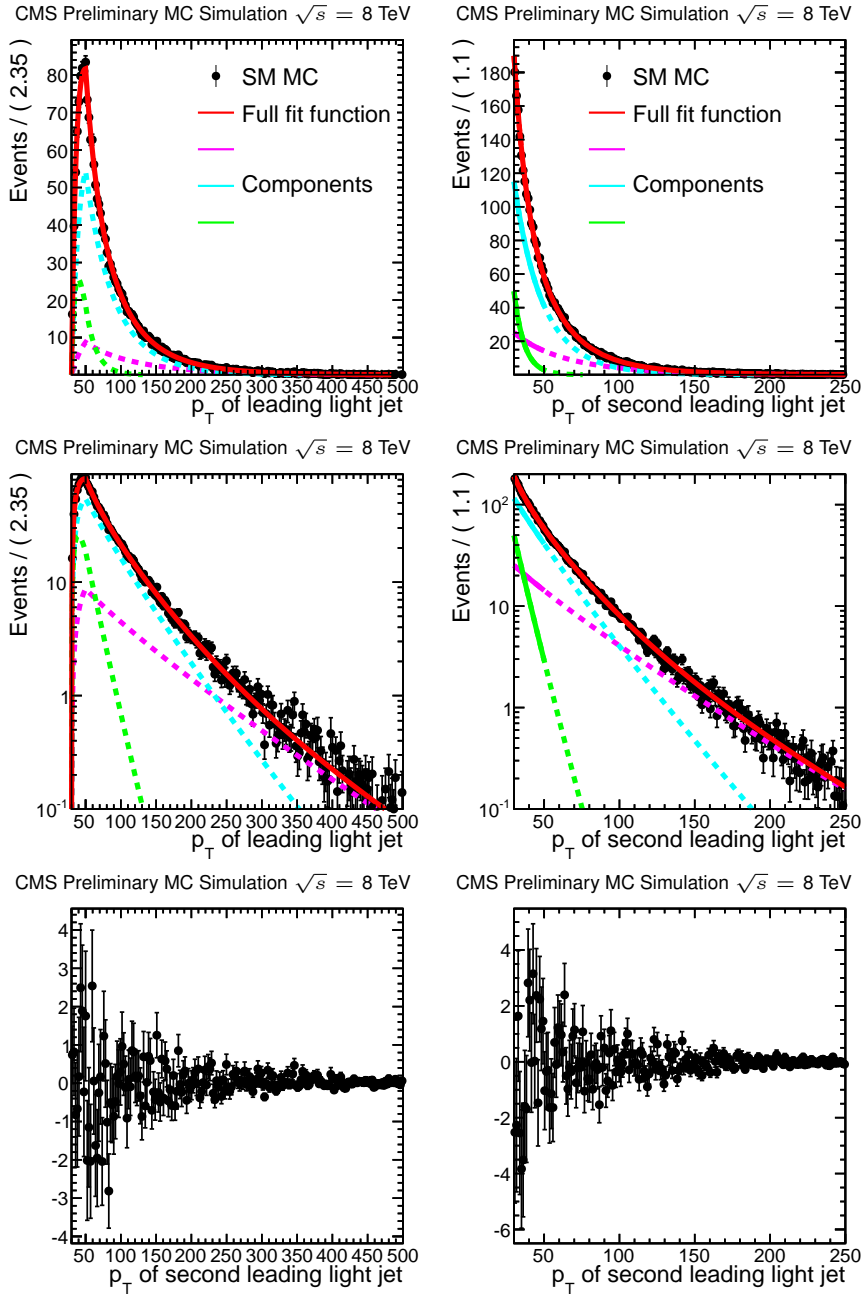


Figure 4.6: Fit to the leading and second leading light jet  $p_T$  spectra in SM simulation, in events where both light jets have  $p_T$  below 50 GeV. The distribution defined in Eq. 4.1 is used to fit the two-dimensional light jet  $p_T$  shape. The fit components are shown in pink, green, and blue, and the full fit function in red. The left (right) panel shows the  $p_T$  of the leading (second leading) light jet. Top: linear scale; center: logarithmic scale; bottom: pull distribution.

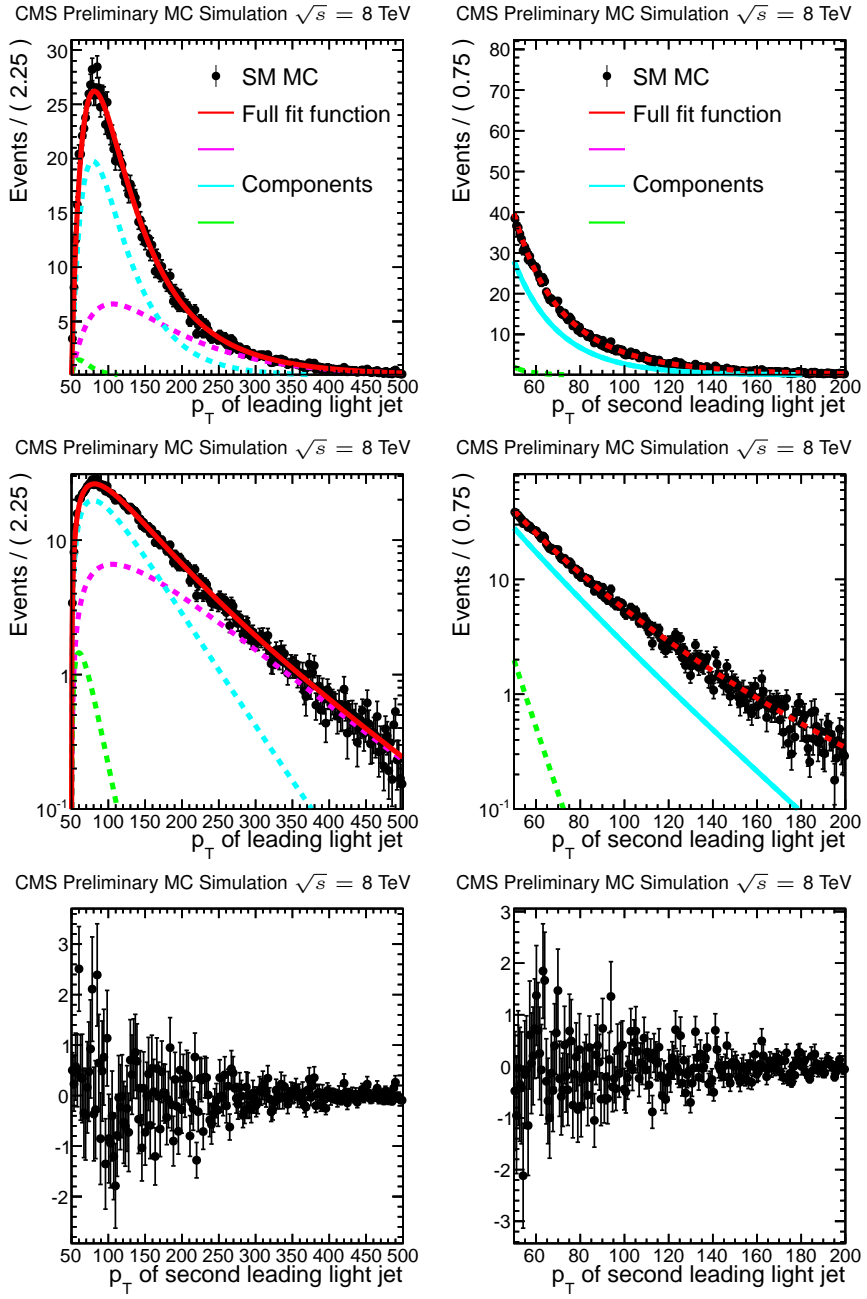


Figure 4.7: Fit to the leading and second leading light jet  $p_T$  spectra in SM simulation, in events where both light jets have  $p_T$  above 50 GeV. The distribution defined in Eq. 4.1 is used to fit the two-dimensional light jet  $p_T$  shape. The fit components are shown in pink, green, and blue, and the full fit function in red. The left (right) panel shows the  $p_T$  of the leading (second leading) light jet. Top: linear scale; center: logarithmic scale; bottom: pull distribution.

ulation to check for eventual biases introduced by the fit function, or sensitivity to statistical fluctuations. We then compare the yield predicted by the fit, i.e., the product of the total number of events in the sub-sample and the integral of the fit function in the selected region, to the observed count in the selected region in the toy dataset.

We construct the toy datasets by generating random numbers and comparing them to the weight of an event in the SM simulation. We add events with weights larger than the random number to the sub-sample. This is done for every event in the SM simulation, and the procedure is repeated many times to create multiple toys.

Figure 4.8 shows results of the toy fits in the four regions described above. Since information is shared amongst bins in the fit, we expect the widths of the predicted and observed yield distributions to be different; however the central values of the yields agree as they should. We do not find any systematic shift of the yield due to the fitted function.

In view of the fit results to both the full SM simulation and data-sized subsamples of the simulation, we conclude that the function defined in Eq. 4.1 is a good description of the background light jet  $p_T$  distribution.

#### 4.4.1.2 Signal model

The two-dimensional distribution of leading and second leading light jet  $p_T$  in signal,  $\rho_{2D}^{\text{signal}}(p_T^{(1)}, p_T^{(2)})$ , is modeled by the sum of two two-dimensional log-normal distributions, with the jets ordered by  $p_T$ . The parameters of the two distributions and their relative fractions are determined from a maximum like-

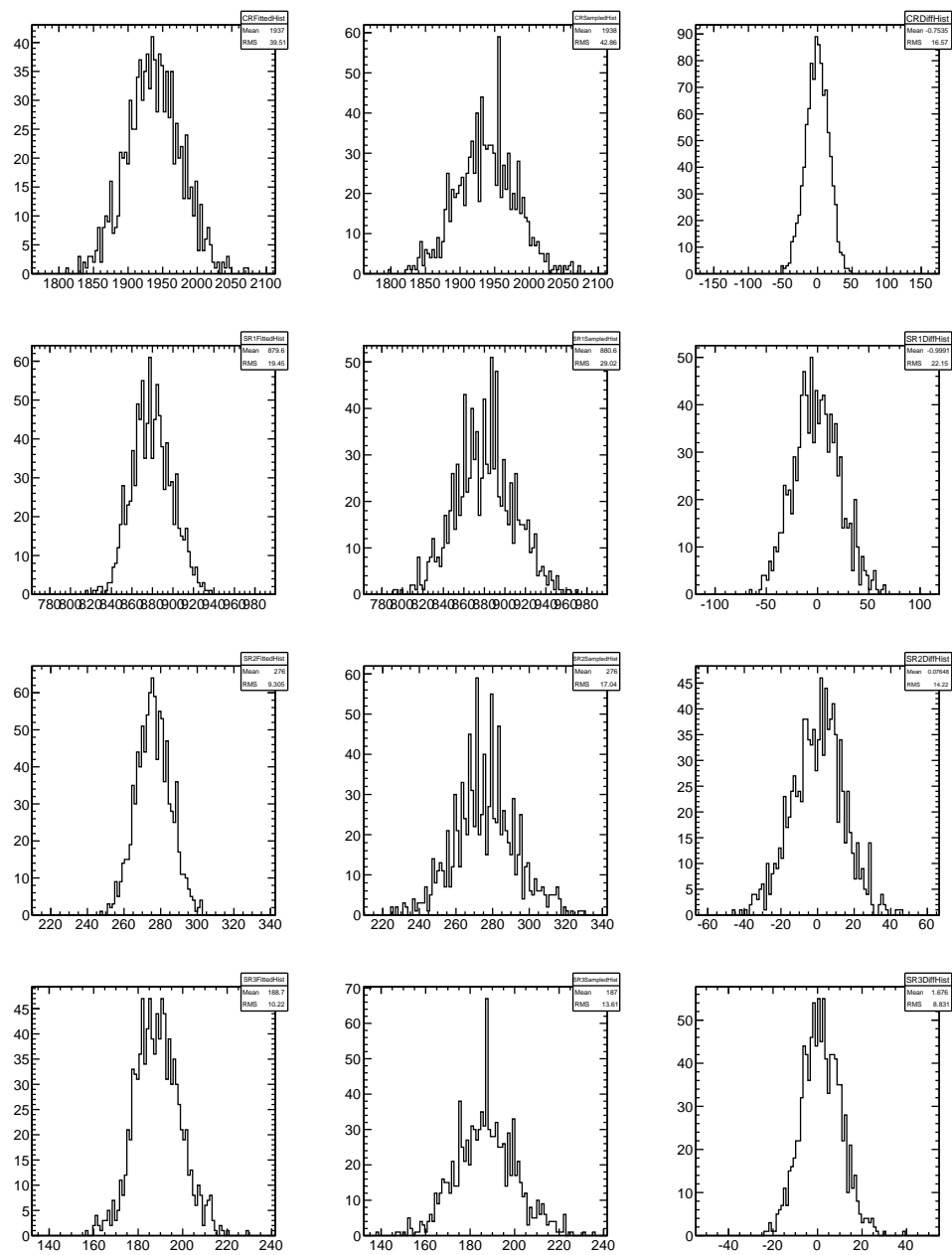


Figure 4.8: Results of light jet fit to toy samples of the SM simulation. Left: yield predicted by the fit. Center: true yield in the toy sample. Right: difference of the two. From top to bottom, plots of the CR, SR1, SR2, and SR3 selections.

lihood fit to the signal simulation.

#### 4.4.1.3 Signal and background comparison

The light jet  $p_T$  shapes in signal and background are compared in Fig. 4.9, in which we show results of the background-only hypothesis fit to data, and the signal distribution fit to the simulation of a  $\tilde{b}$  squark with a mass of 350 GeV, in regions SR1–3. This illustrates the discriminating power of the two-dimensional light jet  $p_T$  spectrum, even at low signal mass. For higher  $\tilde{b}$  masses the light jets will be boosted even further, thus enhancing the discriminating power. The results of the background-only fit to data are presented, in one-dimensional slices in the leading and second leading light jet  $p_T$ , in Fig. 4.10.

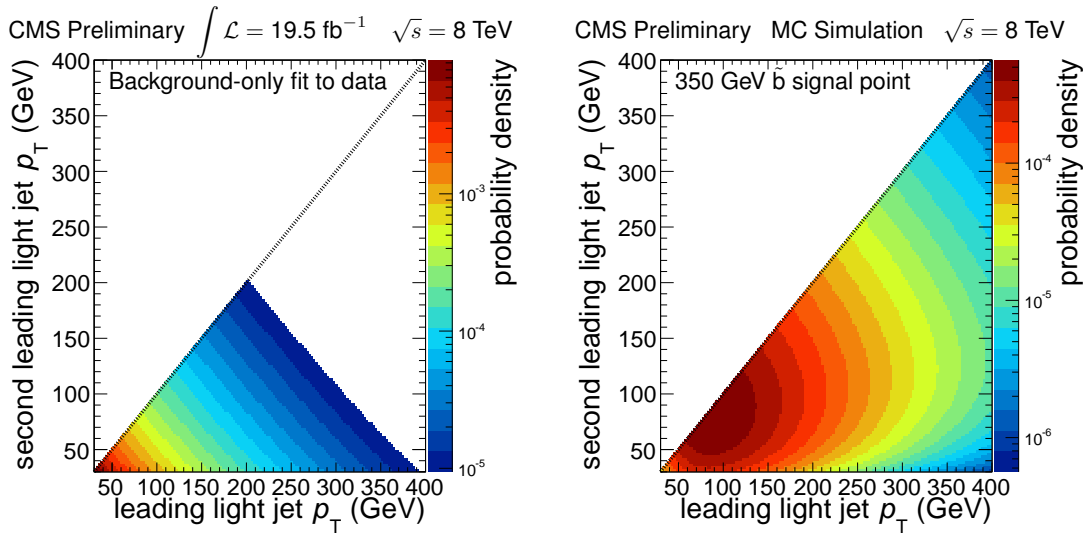


Figure 4.9: Two-dimensional light jet  $p_T$  distributions for (left) the background-only hypothesis fit to data, and (right) the  $\tilde{b}$  signal with a mass of 350 GeV. The diagonal line emphasizes the ordering of the jets by  $p_T$ .

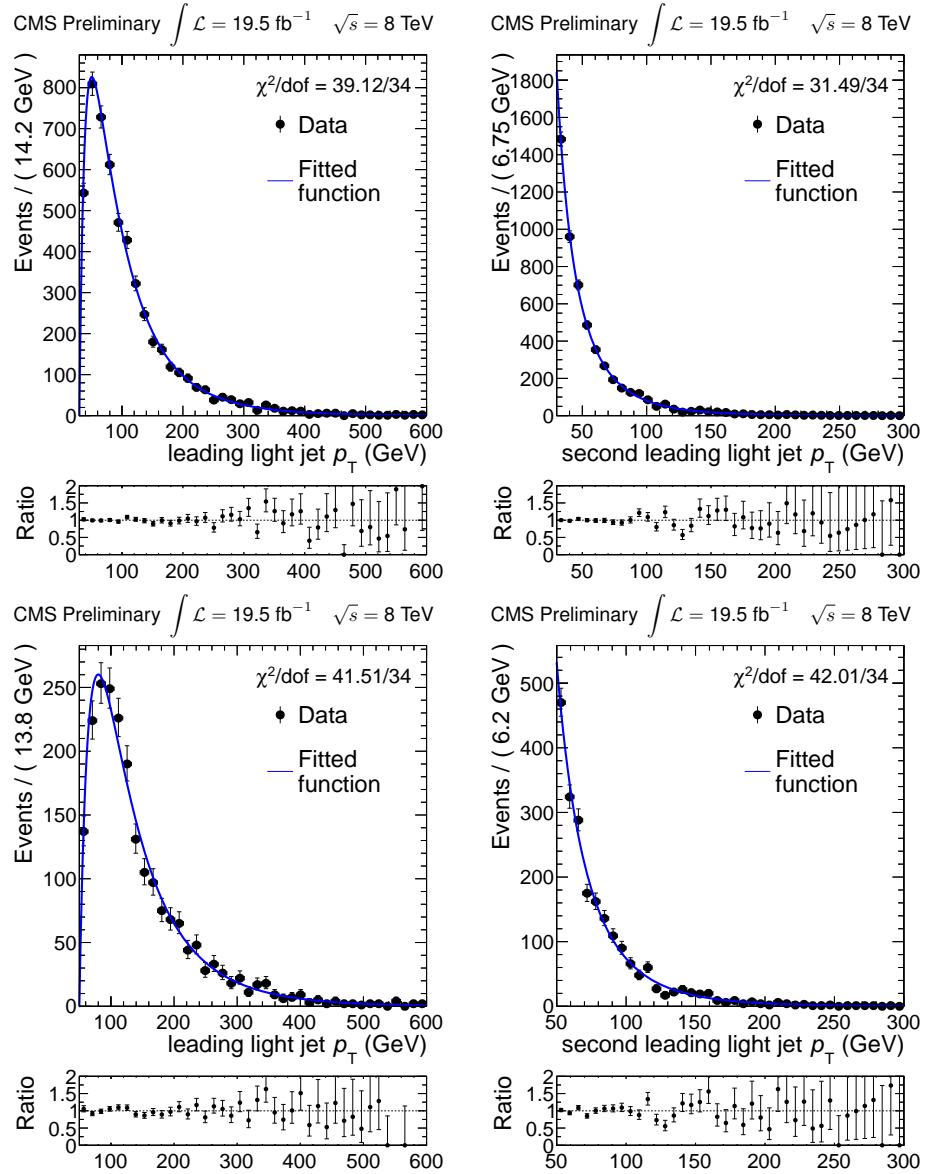


Figure 4.10: Light jet  $p_T$  distributions in data with results of the background-only fit to data overlaid. The line represents the fitted function and the points represent the data. The ratio of the data to the fitted function is also shown. The top row shows the (left) leading light jet distribution and (right) second leading light jet distribution. The bottom row is restricted to events with second leading light jet  $p_T > 50 \text{ GeV}$ .

#### 4.4.2 Resonance reconstruction

Signal events display a resonance in the mass spectrum of  $\tilde{b}$  particles, while such a behavior is not anticipated in SM backgrounds. We therefore use the reconstructed resonant mass spectrum to further discriminate between signal and background. In addition, we would like to derive the mass of the new particle in case of a discovery. We outline below the technique used to reconstruct the four-momenta of  $\tilde{b}$  candidates. We then present the parameterizations chosen to model the spectrum in signal and background.

The resonant mass spectrum is calculated by reconstructing the decay chain of  $\tilde{b}$  particles. In this thesis we focus on pair-produced  $\tilde{b}$  squarks. Each  $\tilde{b}$  decay produces a top quark and light quark, and in the leptonic channel the top quark decays to a b quark, lepton, and neutrino. We first reconstruct top quark pair candidates using the reconstructed b-tagged jet momenta, lepton momenta, and  $E_T^{\text{miss}}$ . We then reconstruct potential  $\tilde{b}$  pairs by combining the top quark candidates with the measured light jets.

##### 4.4.2.1 Neutrino reconstruction

In order to reconstruct the top quarks, we must first determine the four-momenta of the neutrinos produced in the leptonic top quark pair decays. Neutrinos escape the detector unmeasured, so we employ the following procedure to reconstruct their four-momenta. We assume that all decays occur on-shell. We assign the two highest- $p_T$  b-jets and leptons in the event as originating from the top quark pair decays. Using the measured jet and lepton momenta, the  $E_T^{\text{miss}}$ , and the values of the top quark and  $W^\pm$  boson masses [14], conservation

of four-momentum can be written:

$$m_t^2 = (p_{\ell^+} + p_\nu + p_b)^2 \quad (4.4a)$$

$$m_t^2 = (p_{\ell^-} + p_{\bar{\nu}} + p_{\bar{b}})^2 \quad (4.4b)$$

$$m_W^2 = (p_{\ell^+} + p_\nu)^2 \quad (4.4c)$$

$$m_W^2 = (p_{\ell^-} + p_{\bar{\nu}})^2 \quad (4.4d)$$

$$0 = p_\nu^2 \quad (4.4e)$$

$$0 = p_{\bar{\nu}}^2. \quad (4.4f)$$

We further assume the measured  $E_T^{\text{miss}}$  in the event arises from the neutrinos associated with the leptonic  $W^\pm$  decays <sup>1</sup>:

$$E_T^{\text{miss}}_x = (p_\nu + p_{\bar{\nu}})_x \quad (4.5a)$$

$$E_T^{\text{miss}}_y = (p_\nu + p_{\bar{\nu}})_y. \quad (4.5b)$$

The above equations reduce to six linear and two quadratic equations in the neutrino and anti-neutrino four-momenta:

$$2p_b \cdot p_\nu = m_t^2 - m_W^2 - 2p_b \cdot p_\ell^+ \quad (4.6a)$$

$$2p_{\bar{b}} \cdot p_{\bar{\nu}} = m_t^2 - m_W^2 - 2p_{\bar{b}} \cdot p_\ell^- \quad (4.6b)$$

$$2p_{\ell^+} \cdot p_\nu = m_W^2 - m_{\ell^+}^2 \quad (4.6c)$$

$$2p_{\ell^-} \cdot p_{\bar{\nu}} = m_W^2 - m_{\ell^-}^2 \quad (4.6d)$$

$$0 = p_\nu^2 \quad (4.6e)$$

$$0 = p_{\bar{\nu}}^2 \quad (4.6f)$$

$$E_T^{\text{miss}}_x = (p_\nu + p_{\bar{\nu}})_x \quad (4.6g)$$

$$E_T^{\text{miss}}_y = (p_\nu + p_{\bar{\nu}})_y, \quad (4.6h)$$

---

<sup>1</sup>The assumption is reasonable in this analysis framework since we focus on a model that does not include a source of  $E_T^{\text{miss}}$  in the new particle decays. This no longer holds in the  $R$ -parity conserving MSSM.

which finally reduce to a quartic equation [67, 68].

A quartic equation has up to four solutions that can be real or complex, though we only consider the physical solutions, i.e., with real positive neutrino energies. Since we are not able to distinguish between b and anti-b quarks, we solve the quartic equation twice (once for each lepton and b-jet pairing), yielding up to eight possible solutions.

The four-momenta of top quark candidates are then calculated by summing the different possible neutrino momenta with the measured lepton and b-tagged jet momenta. Finally, we obtain  $\tilde{b}$  candidate four-momenta by combining top quark candidates with the two highest- $p_T$  light jets in the event, thus generating up to 16 solutions per event.

#### 4.4.2.2 Jet sampling

Sometimes there are no physical solutions to the quartic equation described above. Since in decays with two real top quarks the quartic equation should always have a real solution, we ascribe the lack of solution to a resolution effect. If the detector resolution were infinite, we would perfectly measure the objects in the event. However reconstructed objects have varying resolutions, depending on their type. The main source of uncertainty originates from the measurement of jets, which will not only affect the jet four-momenta but also the  $E_T^{\text{miss}}$ .

Accordingly, we vary jets within their resolution and determine whether this allows us to find real solutions. We follow the resampling method outlined in Ref [69]. We use the standard CMS jet resolutions, which can be found in

Ref. [70]. We obtain the  $p_T$ ,  $\eta$  and  $\varphi$  resolutions of each measured jet in the event, which are a function of the jet  $p_T$  and  $\eta$ . For each jet, we randomly sample from normal distributions of widths the  $p_T$ ,  $\eta$  and  $\varphi$  resolutions, and construct a new jet that represents a potential true jet the reconstructed jet may have originated from, had the detector resolution been infinite.

The sampling is repeated for each jet in the event, and we recompute the  $E_T^{\text{miss}}$  by adding the original jet four-momenta and subtracting the new jet four-momenta<sup>2</sup>. We then re-solve the quartic equation, replacing the original jets with the resampled jets. We quantify the offset from the collection of new jets to the collection of original measured jets in terms of the sum, over all jets and the  $p_T$ ,  $\eta$  and  $\varphi$  coordinates, of the square of the ratio of sampling parameters to resolution widths. This corresponds to a distance in a  $3N_{\text{jets}}$ -dimensional space, where  $N_{\text{jets}}$  is the number of jets in the event.

We perform the resampling procedure 1000 times per event, and select the sampling that yields the new jet collection that is closest to the original jets, as quantified by the measure described above. We then select the solution to the quartic equation yielding pairs of  $\tilde{b}$  candidates with the closest masses, as measured by the absolute value of the logarithm of the ratio of the two masses, to reconstruct two  $\tilde{b}$  candidates per event. The average of the candidates' masses, denoted  $M_{t,\text{jet}}$ , is used to approximate the mass of the resonance. It is bounded below by the top quark mass.

The resampling procedure increases the number of events with at least one real solution to the quartic equation, and hence the event selection efficiency, by approximately 40% in both simulated signal and SM background events. The

---

<sup>2</sup>The  $E_T^{\text{miss}}$  is defined in Section 3.5.2 as the negative vector sum over all objects of object momenta in the transverse plane.

increase in efficiency is dependent upon the number of samplings: if we had the necessary resources to run an infinite number of toys, the procedure would be 100% efficient and yield the overall closest solution, using the above distance measure, to the reconstructed jets; in practice this is impossible. The number of samplings per event (1000) was chosen because it allows a reasonable trade-off between increase in efficiency and computational time, and we have verified that the potential gains in sensitivity are negligible. We investigate a different reconstruction method, one that would yield a 100% reconstruction efficiency, in Appendix A.

In Table 4.3 we present the efficiency of reconstructing the neutrino four-momenta, and hence the  $\tilde{b}$  candidates, in simulation for different  $\tilde{b}$  signal masses as well as  $t\bar{t}$  for comparison. A summary can be found in Fig. 4.11.

We compare in Fig. 4.12 the reconstructed mass distributions in events where a real solution to the quartic equation exists and in events where it was necessary to use the resampling method in order to successfully reconstruct  $\tilde{b}$  candidates, in simulated signal and  $t\bar{t}$  background events. We conclude that the sampling procedure does not bias the reconstructed resonance mass spectrum.

Finally, we detail below the parameterizations chosen to model the reconstructed resonance mass distributions in signal and background.

#### 4.4.2.3 Background model

Since SM backgrounds do not contain a mass resonance, we expect the reconstructed mass spectrum to be steeply falling. However, the selection requirements on jet and lepton  $p_T$ s introduce a turn-on in the shape that is accompa-

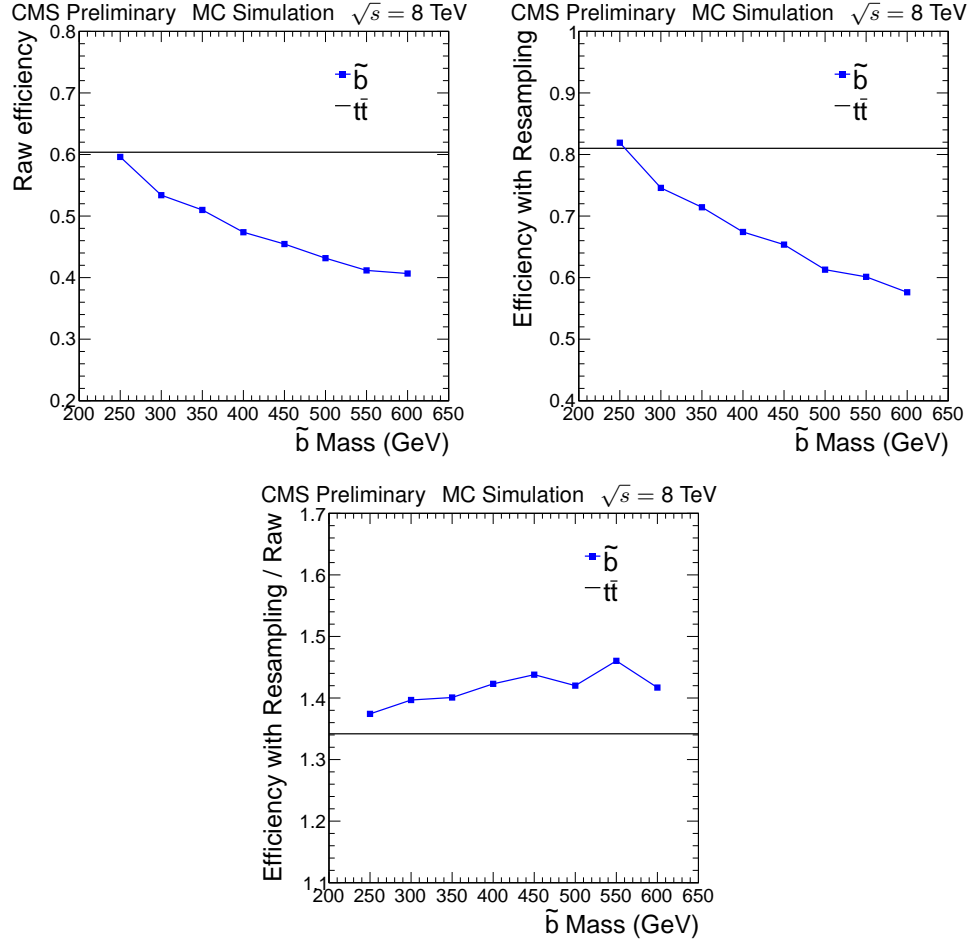


Figure 4.11: Efficiency, after all kinematic selections defined in Section 4.3.2 have been applied, of reconstructing  $\tilde{b}$  pair candidates. Top row: before (left) and after (right) the jet resampling technique has been applied. Bottom row: ratio of efficiencies with and without jet resampling.

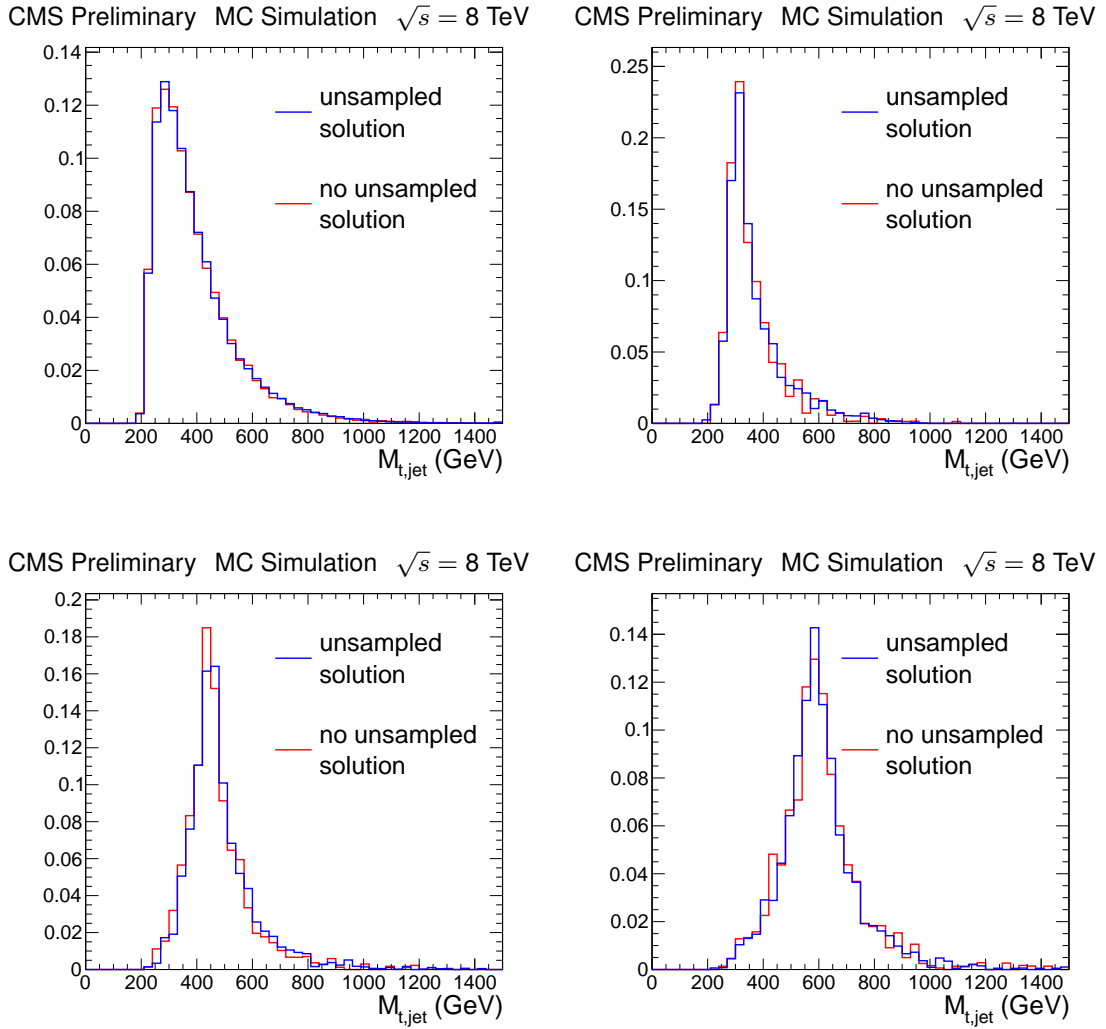


Figure 4.12: Reconstructed resonance mass spectrum after full event selection in simulated  $t\bar{t}$  (top left) and signal events for  $\tilde{b}$  particle masses of 300 GeV (top right), 450 GeV (bottom left), and 600 GeV (bottom right). The blue histogram corresponds to events for which a real neutrino solution exists without having to sample over jet resolutions, and the red histogram represents events for which the sampling method was applied. Both histograms are normalized to unit area.

Table 4.3: Efficiency of the mass reconstruction method, with and without integration over jet resolution (resampling procedure), and ratio of efficiencies, in signal simulation for different mass points. The efficiency in  $t\bar{t}$  simulation is given for comparison.

$\tilde{b}$ Mass (GeV)	Raw Efficiency	Efficiency with Resampling	Ratio Resampled/Raw
250	59.6%	81.9%	1.37
300	53.4%	74.6%	1.40
350	51.0%	71.4%	1.40
400	47.4%	67.4%	1.42
450	45.5%	65.4%	1.44
500	43.2%	61.3%	1.42
550	41.2%	60.1%	1.46
600	40.7%	57.6%	1.42
$t\bar{t}$	60.4%	81.0%	1.34

nied as predicted by a falling tail. The distribution is bounded below by the top quark mass.

We model this spectrum as the sum of a gamma distribution and a log-normal distribution, and require both functions to peak at the same value. This produces the desired turn-on, peak, and steeply falling tail. Following the classification of events depending on the second leading light jet  $p_T$ , we define four independent copies of the function, one for each region defined in Section 4.4.1. The distribution modeling the background mass spectrum is denoted  $\rho_{\text{mass}}^{\text{SM}}(m | p_T^{(2)})$ , emphasizing that the distribution is defined conditionally upon the value of the second leading light jet  $p_T$ . We present results of the fit to data

of the reconstructed invariant mass distribution in each of the four light jet  $p_T$  regions, for the background-only hypothesis, in Fig. 4.13. In this fit the parameters of the gamma and log-normal distributions, and their relative fractions, are allowed to vary.

The parameters of the two distributions and their relative fractions are determined from a maximum likelihood fit to the data, using the likelihood defined in Section 4.6.

#### 4.4.2.4 Signal model

Signal events display a characteristic peak in the reconstructed mass spectrum, due to the presence of two resonant decays. Since there is a two-fold ambiguity in pairing the leptons and b-tagged jets, and again in pairing the top quark candidates and light flavor jets, there are actually two categories of events entering into the mass distribution: one corresponds to events where all the different objects have been correctly paired, while the other includes events in which there is an incorrect pairing.

These two categories contribute differently to the overall mass spectrum. When objects are correctly paired, the resulting peak has a narrower width than when objects are incorrectly paired. In addition, incorrect pairings result in longer tails. Figure 4.14 illustrates these features in simulated signal events, for low-mass and high-mass  $\tilde{b}$  particles, in the three signal regions defined above. It follows that the regions are populated differently depending on the  $\tilde{b}$  particle mass. This aspect plays an important role in the increased sensitivity.

In order to model the two separate categories, we parameterize the recon-

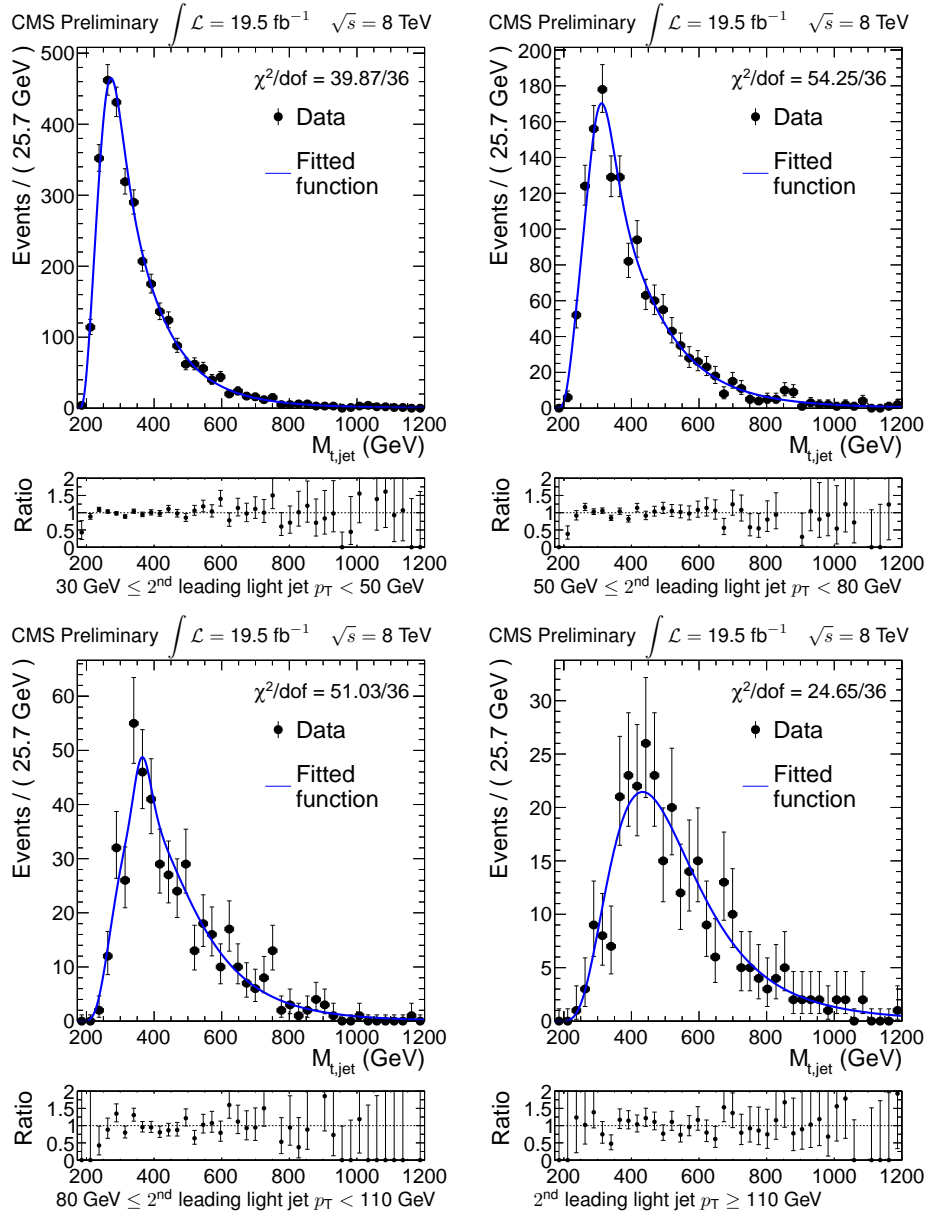


Figure 4.13: Reconstructed invariant mass  $M_{t,jet}$  distribution in data with results of the background-only fit to data overlaid. The fitted function is the sum of a gamma distribution and a log-normal distribution that are forced to peak at the same value. The line represents this fitted function and the points represent the data. The ratio of the data to the fitted function is also shown. Top left: second leading jet  $p_T$  between 30 GeV and 50 GeV. Top right: second leading jet  $p_T$  between 50 GeV and 80 GeV. Bottom left: second leading jet  $p_T$  between 80 GeV and 110 GeV. Bottom right: second leading jet  $p_T$  greater than 110 GeV.

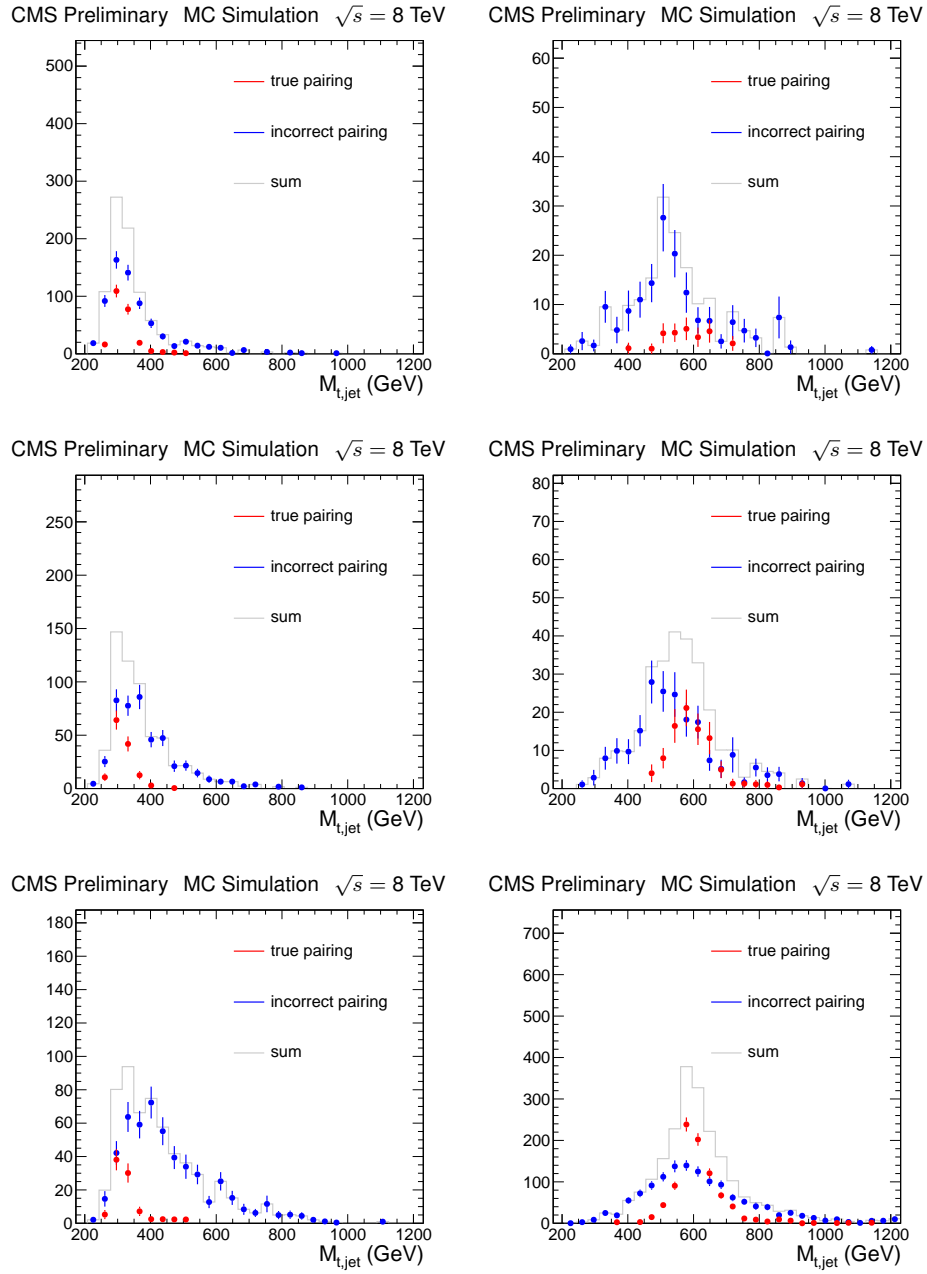


Figure 4.14: Reconstructed invariant mass  $M_{t,\text{jet}}$  distribution in simulated signal events with  $\tilde{b}$  squark mass of 300 GeV (right) and 600 GeV (left). Events are categorized using Monte Carlo truth to determine whether the  $b$ -quark jets and leptons have been correctly (red) or incorrectly (blue) paired in reconstructing the top quark candidates. Uncertainties are statistical only. Top: second leading light jet  $p_T$  between 50 and 80 GeV (SR1). Middle: second leading light jet  $p_T$  between 80 and 110 GeV (SR2). Bottom: second leading light jet  $p_T$  above 110 GeV (SR3).

structed resonant mass spectrum in signal as the sum of two gamma distributions. Again we use four independent functions to model the spectrum in each signal region. The parameters of the distributions are determined by a maximum likelihood fit to the signal simulation. We denote the signal mass distribution  $\rho_{\text{mass}}^{\text{signal}}(m | p_T^{(2)})$ .

## 4.5 Systematic uncertainties

Measurements of a physical observable must account for systematic uncertainties, i.e., uncertainties arising from the dependence of this observable on other quantities, which are either unknown or imperfectly known. For example, the measurement of the energy of a jet depends on the jet energy resolution, itself a function of the detector performance, and the jet energy calibration, which is dependent on how well the detector response is understood. Systematic effects are taken into account by estimating the consequence of a variation due to these effects, e.g. a shift in the jet energy scale, on the result of the measurement.

### 4.5.1 Background

The background model is parameterized using the shapes described in Sections 4.4.1.1 and 4.4.2.3. Although we rely on the SM simulation to test various pdfs, the parameters for the light jet  $p_T$  and resonant mass distributions are determined entirely from a fit to the data. Therefore we do not consider simulation uncertainties on the background shape estimate.

The flexibility of the background shape was studied in SM simulation by fitting toy datasets. Results are presented in Section 4.4.1.1. We find that the chosen distribution is sufficiently general, with any differences between the assumed and true shapes negligible in comparison with statistical uncertainties.

### 4.5.2 Signal

We use MC simulation to model the signal, and consider a range of systematic effects that may affect the light jet  $p_{\text{T}}$  spectrum, the resonance reconstruction procedure, and the distribution of the mass of the reconstructed heavy resonances. We discuss below the sources of systematic uncertainty considered and the methods used to evaluate their effect on the parameters of the signal model and the signal selection efficiency.

We account for the uncertainty in the jet energy scale measurement by varying jet four-momenta upwards and downwards using standard CMS  $p_{\text{T}}$ - and  $\eta$ -dependent correction factors in data and simulation [71]. The different jet energy resolutions in simulation and data are corrected for by scaling the difference between reconstructed jet  $p_{\text{T}}$  and matched generator jet  $p_{\text{T}}$  by an  $\eta$ -dependent data-to-simulation resolution ratio. These scale factors are varied within their uncertainties. Finally we account for any remaining discrepancy in  $E_{\text{T}}^{\text{miss}}$  due to unclustered objects between simulation and data following the method described in Ref. [72]. We recalculate the  $E_{\text{T}}^{\text{miss}}$  separately after each of these corrections have been applied.

Differences in energy scale for lepton objects in simulation and data are corrected using energy scale factors [42,61]. The four-momenta of electrons passing the selection requirements described in Section 4.3.1 within the range  $|\eta| < 1.5$  is varied by 0.6%, while that of electrons with  $1.5 < |\eta| < 2.5$  is varied by 1.5%. We vary the four-momenta of muons passing the selection requirements described in Section 4.3.1 by 0.2%. We neglect uncertainties on the scale factors, which are smaller than 0.1%. The  $E_{\text{T}}^{\text{miss}}$  is recalculated after varying each lepton four-momentum. We account for uncertainties originating from lepton reconstruc-

tion and isolation effects by assigning a 0.5% uncertainty to the signal selection efficiency in each lepton flavor category ( $ee$ ,  $e\mu$  and  $\mu\mu$ ). These three uncertainties are 100% correlated between each category. We account for the uncertainty in the trigger efficiency by applying a 1% systematic on the signal selection efficiency in each lepton flavor category ( $ee$ ,  $e\mu$  and  $\mu\mu$ ), as measured in Ref. [73].

We separately vary the b, c and light flavor tagging efficiencies within their statistical uncertainties. To account for differences in tagging efficiencies between simulation and data, we vary the standard CMS data-to-simulation scale factors within their measured uncertainties [49, 50]. The b and c scale factors are treated as correlated, while the light flavor scale factors are treated as uncorrelated with the heavy flavor scale factors.

We follow the prescription of the PDF4LHC Working Group [74] to account for uncertainties on the PDFs. The luminosity is assigned its measured uncertainty of 2.6% [75]. We vary the measured distribution of the number of pile-up interactions in data by 5% to account for uncertainties due to pile-up. Finally we take into account uncertainties on the signal selection efficiency due to the limited size of the signal simulation samples using Poisson statistics.

The method used to incorporate these systematics into the statistical model is described in Section 4.6.3.

Figure 4.15 presents the overall signal selection efficiency in each lepton flavor category after the event selection described in Section 4.3.2 has been applied, and including the above systematic uncertainties, as a function of  $\tilde{b}$  squark mass. Here we have incorporated the 9.4% branching fraction of top quarks to leptonic final states [14]. Correlations between the efficiencies or changes to

the relative efficiency in each of the light jet  $p_T$  bins defined in Section 4.4.1.1 are not included here, but are taken into account in the full statistical model.

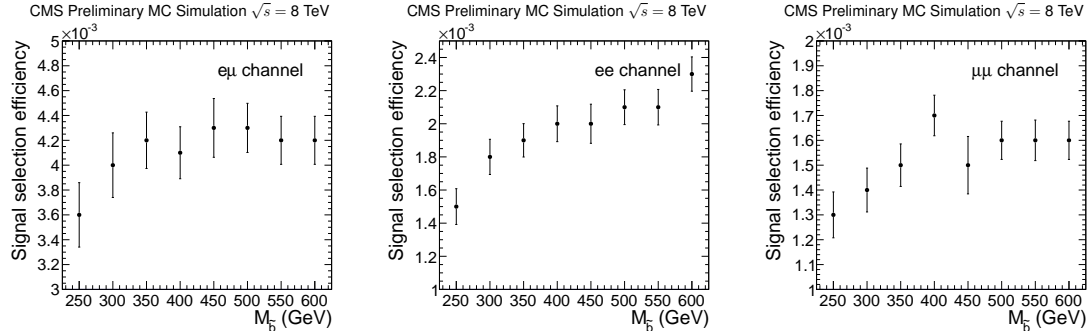


Figure 4.15: Signal selection efficiency and relative systematic uncertainty in the efficiency in each lepton flavor channel for the  $\tilde{b}$  signal model, as a function of  $\tilde{b}$  mass. This neglects correlations between the efficiencies, which are taken into account in the full analysis. Left:  $e\mu$  channel, center:  $ee$  channel, right:  $\mu\mu$  channel.

We present the uncertainty in the signal selection efficiency due to each of the above systematic effects in Table 4.4 for a  $\tilde{b}$  squark of mass 350 GeV. We find that the combined systematic uncertainties change the calculated value of the upper limit on the signal cross section by between 1% and 10%, depending on the  $\tilde{b}$  mass, in comparison to the upper limit calculated with statistical uncertainties only. Across the considered range of  $\tilde{b}$  squark masses, variations to the jet energy scale constitute the dominant systematic effect .

## 4.6 Statistical model

We combine the parameterizations of the light jet  $p_T$  and resonance mass distributions defined in Section 4.4 to build a three-dimensional pdf, and use this

Table 4.4: Relative systematic uncertainty on the signal selection efficiency broken down by source of signal systematic uncertainty in the signal simulation of a 350 GeV  $\tilde{b}$  squark.

Simulation uncertainty	350 GeV $\tilde{b}$
Heavy flavor scale factor for b-tagging	4.9%
Light flavor scale factor for b-tagging	4.7%
Jet Energy Scale	4.6%
Signal MC Statistics	2.1%
Jet Energy Resolution	1.8%
Pile up	1.5%
Parton density function	1.0%
MC b-tagging efficiency for b-jets	0.43%
MC b-tagging efficiency for c-jets	0.25%
MC b-tagging efficiency for light jets	0.52%
Electron Energy Scale	0.19%
Muon Energy Scale	0.04%

pdf to create a likelihood function. We fit this likelihood to the data in order to determine the amount of signal allowed in the observed dataset, which is controlled by the signal cross section.

#### 4.6.1 Background probability density function

The background shape is defined as a three-dimensional distribution in the invariant mass, leading, and second leading light jet  $p_T$  variables, and is written

as the product of the background light jet shape and the invariant mass shapes that are defined in Eq. 4.1 and Section 4.4.2.3, respectively:

$$\rho_{3D}^{SM}(m, p_T^{(1)}, p_T^{(2)}) = \rho_{mass}^{SM}(m|p_T^{(2)}) \rho_{2D}^{SM}(p_T^{(1)}, p_T^{(2)}). \quad (4.7)$$

The relative normalizations of the invariant mass distributions in the four regions (CR and SR1–3) are determined by the integral of the two-dimensional light jet distribution in the corresponding region.

### 4.6.2 Signal probability density function

Just as in the background parameterization, we take the product of the two-dimensional light jet signal shape with the signal invariant mass shape, defined in Sections 4.4.1.2 and 4.4.2.4, respectively, to construct a three-dimensional signal distribution:

$$\rho_{3D}^{signal}(m, p_T^{(1)}, p_T^{(2)}) = \rho_{mass}^{signal}(m|p_T^{(2)}) \rho_{2D}^{signal}(p_T^{(1)}, p_T^{(2)}). \quad (4.8)$$

Again the relative normalizations of the mass shapes in the different signal regions are controlled by the light jet shape.

### 4.6.3 Incorporating systematic uncertainties

We include uncertainties due to the systematic effects described in Section 4.5.2 into the likelihood through the use of external constraint functions, following the method described below.

The signal simulation is reweighted to account for a  $\pm 1$  standard deviation variation in a particular source of systematic uncertainty. We then perform a

maximum likelihood fit to the re-weighted simulation of the signal distribution, and determine how the parameters of the signal model vary. In addition we find how the signal selection efficiency changes with the  $\pm 1$  standard deviation variation.

We incorporate this information into a covariance matrix, and add the covariance matrices for each source of systematic uncertainty. Finally we construct a multi-variate normal distribution from the summed covariance matrices and the central values of the signal model parameters, which are taken from the simulation. This distribution, denoted  $\rho_{\text{syst}}$ , is used to constrain the signal model parameters.

We find that allowing the signal invariant mass parameters to vary within their uncertainties in the constraint function has a negligible effect on the signal sensitivity, but speeds the calculation of toy limits by a large factor. Therefore we set the signal mass parameters in the constraint function to their maximum likelihood values in simulation, and do not allow them to vary. However, in the final constraint function the signal light jet parameters and selection efficiencies are allowed to vary within their uncertainties. Along with the background shape parameters these constitute the set of nuisance parameters.

#### 4.6.4 Signal plus background model

We construct a complete distribution from the sum of the background and signal distributions, defined in Eqs. 4.7 and 4.8, respectively, accounting for the signal cross section  $\sigma_{\text{signal}}$  and the signal selection efficiency  $\mathcal{E}$ :

$$\rho_{3D}^{\text{total}} = (\mu^{\text{SM}} \rho_{3D}^{\text{SM}} + \mathcal{E} \sigma_{\text{signal}} \rho_{3D}^{\text{signal}}) / (\mu^{\text{SM}} + \mathcal{E} \sigma_{\text{signal}}), \quad (4.9)$$

where  $\mu^{\text{SM}}$  is the SM yield. The distribution constraining the signal parameters, defined in Section 4.6.3, is  $\rho_{\text{syst}}$ .

We use the above distributions and the data to build an extended unbinned likelihood function, which is written as:

$$\mathcal{L}(\sigma_{\text{signal}}, \theta) = \rho_{\text{syst}} \frac{(\mu^{\text{SM}} + \mathcal{E}\sigma_{\text{signal}})^N \exp(-\mu^{\text{SM}} - \mathcal{E}\sigma_{\text{signal}})}{N!} \prod_{i=0}^N \rho_{\text{3D}}^{\text{total}}(m_i, p_{T_i}^{(1)}, p_{T_i}^{(2)}), \quad (4.10)$$

where  $N$  is the number of events in the data sample;  $m_i$ ,  $p_{T_i}^{(1)}$ , and  $p_{T_i}^{(2)}$  are, respectively, the reconstructed resonance mass, leading light jet  $p_T$ , and second leading light jet  $p_T$  of the  $i^{\text{th}}$  event;  $\sigma_{\text{signal}}$  is the cross section of the signal model; and  $\theta$  is the set of all nuisance parameters, namely the signal light jet, background invariant mass, and background light jet parameters, and the selection efficiencies. The parameter of interest is the signal cross section.

#### 4.6.5 Constructing confidence intervals

We perform hypothesis tests on the signal model for different  $\tilde{b}$  squark masses, applying the unified approach described in Ref. [76] to the parameter of interest, i.e., the signal cross section. The test statistic is the profile likelihood ratio, which is defined as

$$\lambda_p(\sigma) = \frac{\mathcal{L}(\sigma, \hat{\hat{\theta}}(\sigma))}{\mathcal{L}(\hat{\sigma}, \hat{\theta})}, \quad (4.11)$$

where  $\sigma$  is a test value of the cross section and  $\theta$  is the set of nuisance parameters as defined above. The numerator is the profile likelihood function of  $\sigma$ , with  $\hat{\hat{\theta}}(\sigma)$  the values of the nuisance parameters that conditionally maximize  $\mathcal{L}$  given a particular value of  $\sigma$ . The denominator corresponds to the global maximum of the likelihood, where  $\{\hat{\sigma}, \hat{\theta}\}$  are the parameter values that maximize  $\mathcal{L}$ , with

only the requirement that  $\hat{\sigma}$  be non-negative.

We evaluate the profile likelihood ratio in data and in pseudo-data toy experiments. The pseudo-experiments are generated following the frequentist approach outlined in Ref. [77]. Given a particular signal cross section hypothesis, we first determine the values of the nuisance parameters  $\hat{\theta}(\sigma)$  that conditionally maximize the likelihood function of the observed data, with the constraint that the signal cross section is fixed to the test value. We refer to this as the signal-plus-background model. These values  $\hat{\theta}(\sigma)$  are used to generate pseudo-data from the distribution  $\rho_{3D}^{\text{total}}$ , and we evaluate the test statistic defined in Eq. 4.11 for each toy experiment. We repeat this procedure over a finely binned range of values for  $\sigma$ , thus constructing the distribution of  $\lambda_p(\sigma)$ .

Using the distribution of  $\lambda_p(\sigma)$  we test a signal cross section hypothesis by determining the critical value  $\lambda_p^{\text{Cr}}$  for which 95% of the toys satisfy  $\lambda_p(\sigma) > \lambda_p^{\text{Cr}}$ . We reject the cross section hypothesis at 95% confidence level (CL) if the profile likelihood ratio evaluated in data is less than  $\lambda_p^{\text{Cr}}$ . Finally we construct unified intervals from the union of cross sections that are not rejected under this procedure. This treatment of the nuisance parameters was found to have good coverage [78]. If an interval has a lower edge of zero we conclude that we do not see evidence of signal, and use the upper edge as an upper limit on the signal cross section. If on the other hand an interval has a positive lower edge we claim a discovery.

## 4.7 Results and interpretation

We perform a scan of the  $\tilde{b}$  squark simulation over the range of generated masses and construct confidence intervals for each mass point following the procedure outlined above. We observe consistency with the SM-only expectation, i.e., all intervals have a lower edge of zero, and thus set upper limits on the signal cross section. The expected limit distribution is constructed in a similar manner from pseudo-experiments generated using the background-only model, meaning the signal cross section is set to zero in Eq. 4.9.

The observed and expected 95% CL upper limits on the production cross section of  $\tilde{b}$  squark pairs are presented in Table 4.5 and compared to theoretical predictions in Fig. 4.16. Using the intersection of the cross section upper limit and the cross section predicted by the model minus its theoretical uncertainty, we find the median expected limit is 298 GeV, with 68% of the limits falling in the range [283 GeV, 347 GeV], and the observed limit is 326 GeV.

We find that the limits at large  $\tilde{b}$  masses are always greater than the median expected limit. This is due to the bulk of the signal distributions being located in the SR3 region at high mass, and overlaps between the reconstructed invariant mass spectra for the different mass points. The data on the other hand clusters at low mass and in the CR and SR1 regions. An upwards fluctuation in the data therefore easily accommodates a larger amount of signal at high  $\tilde{b}$  mass, thus creating a correlated difference between observed and expected limits.

Figures 4.17 to 4.19 present the results of maximizing the likelihood on the data with the signal cross section set to the observed 350 GeV  $\tilde{b}$  upper limit. These show the reconstructed invariant mass, leading light jet  $p_T$ , and second

Table 4.5: Expected and observed 95% CL upper limits on the pair production cross section of  $\tilde{b}$  squarks decaying to a top quark and light quark, as a function of the squark mass.

$\tilde{b}$ Mass (GeV)	95% CL obs. limit (pb)	95% CL exp. limit (pb)		
		Median	68% CL band	95% CL band
250	2.1	2.2	[1.0,3.1]	[0.50,4.1]
300	1.0	1.8	[1.1,2.5]	[0.35,3.3]
350	1.3	1.5	[0.73,2.0]	[0.25,2.6]
400	0.92	0.76	[0.47,1.2]	[0.18,1.6]
450	0.68	0.48	[0.27,0.72]	[0.067,0.94]
500	0.53	0.37	[0.22,0.56]	[0.051,0.77]
550	0.37	0.27	[0.15,0.41]	[0.043,0.55]
600	0.30	0.21	[0.11,0.32]	[0.031,0.43]

leading light jet  $p_T$  distributions, respectively. In this fit all nuisance parameters, i.e., the signal light jet, background invariant mass, and background light jet parameters, and selection efficiencies, are allowed to vary, while the parameter of interest, the signal cross section, is fixed.

In Figs. 4.20, 4.21, and 4.22 we present the results of scanning over signal cross section hypotheses for the 350 GeV  $\tilde{b}$  mass point. The distribution of p-values, or fraction of pseudo-experiments with a value of the test statistic greater than that observed in data, is shown in Fig. 4.20 as a function of the signal cross section hypothesis. The distribution of observed p-values is determined from the global maximum of the likelihood evaluated on toys generated using the signal-plus-background hypothesis, while the distribution of expected

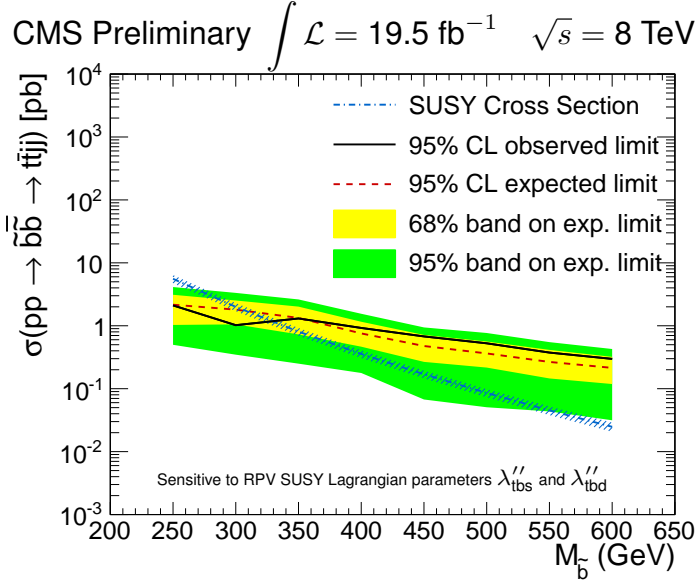


Figure 4.16: Observed and expected 95% CL upper limits on the production cross section of  $\tilde{b}$  squark pairs as a function of squark mass.

p-values is computed from toys generated using the background-only hypothesis. The 68% (95%) CL bands on the expected limit is calculated from the histogram in Fig. 4.21 by determining the values of the best-fit signal cross section at which the fraction of toys above and below the median value corresponds to  $\pm 1$  (2) standard deviations. Distributions of the profile likelihood ratio test statistic obtained from the toy experiments for each tested signal cross section hypothesis are presented in Fig. 4.22.

We note that Figs. 4.20 and 4.21 may not be interpreted in the familiar framework of  $CL_s$  [79, 80], since the unified approach produces confidence intervals that may be one-sided (with a lower edge of zero) or two-sided (with a strictly positive lower edge), while  $CL_s$  intervals are one-sided by construction. The intervals we observe with the unified approach happen to all be one-sided.

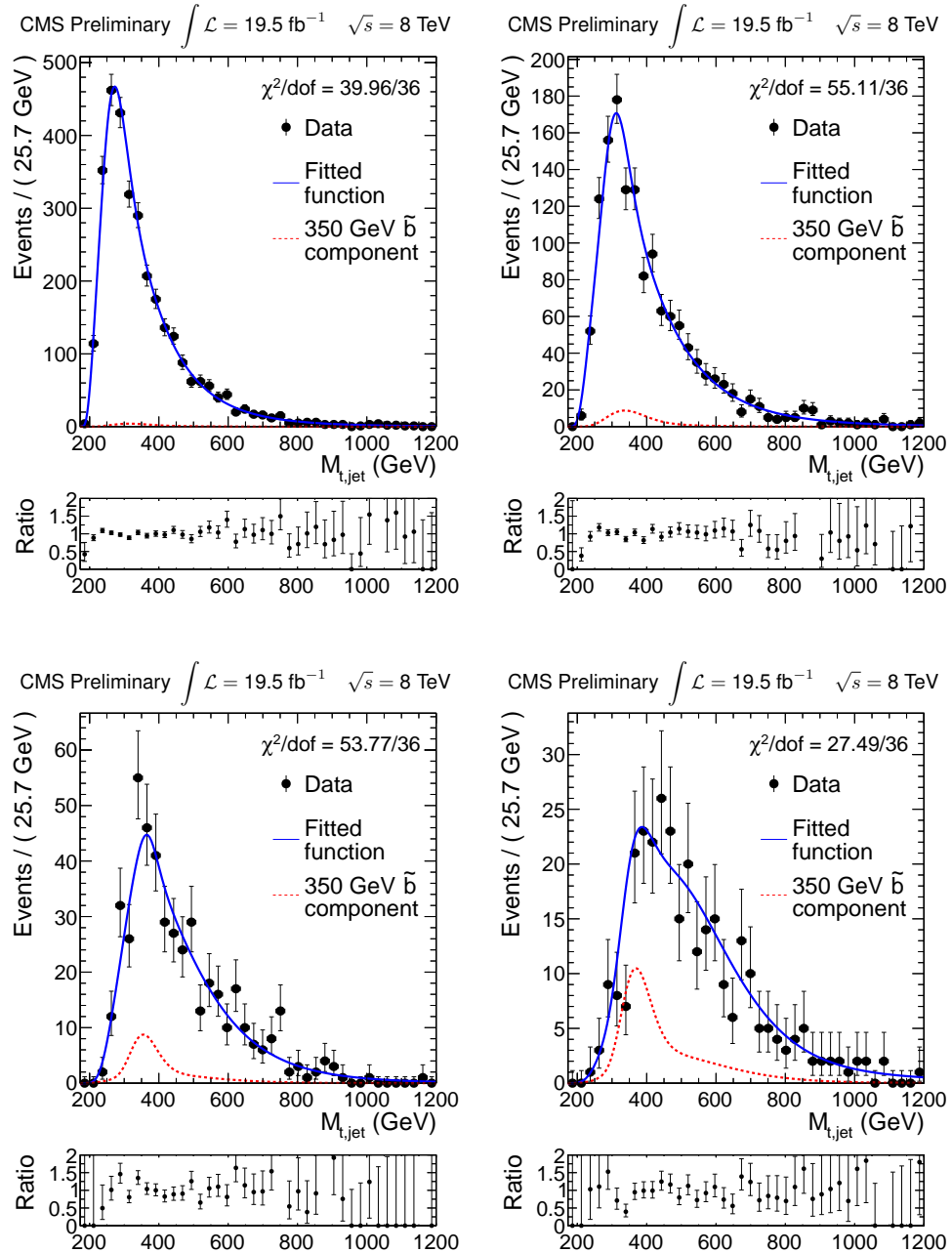


Figure 4.17: Reconstructed invariant mass distributions for results of the likelihood maximization with signal cross section set to the 350 GeV  $\tilde{b}$  upper limit. The solid line shows the fitted function, the dashed line shows the signal component, and the points show the data. From left to right, these are for the CR, SR1, SR2, and SR3 regions.

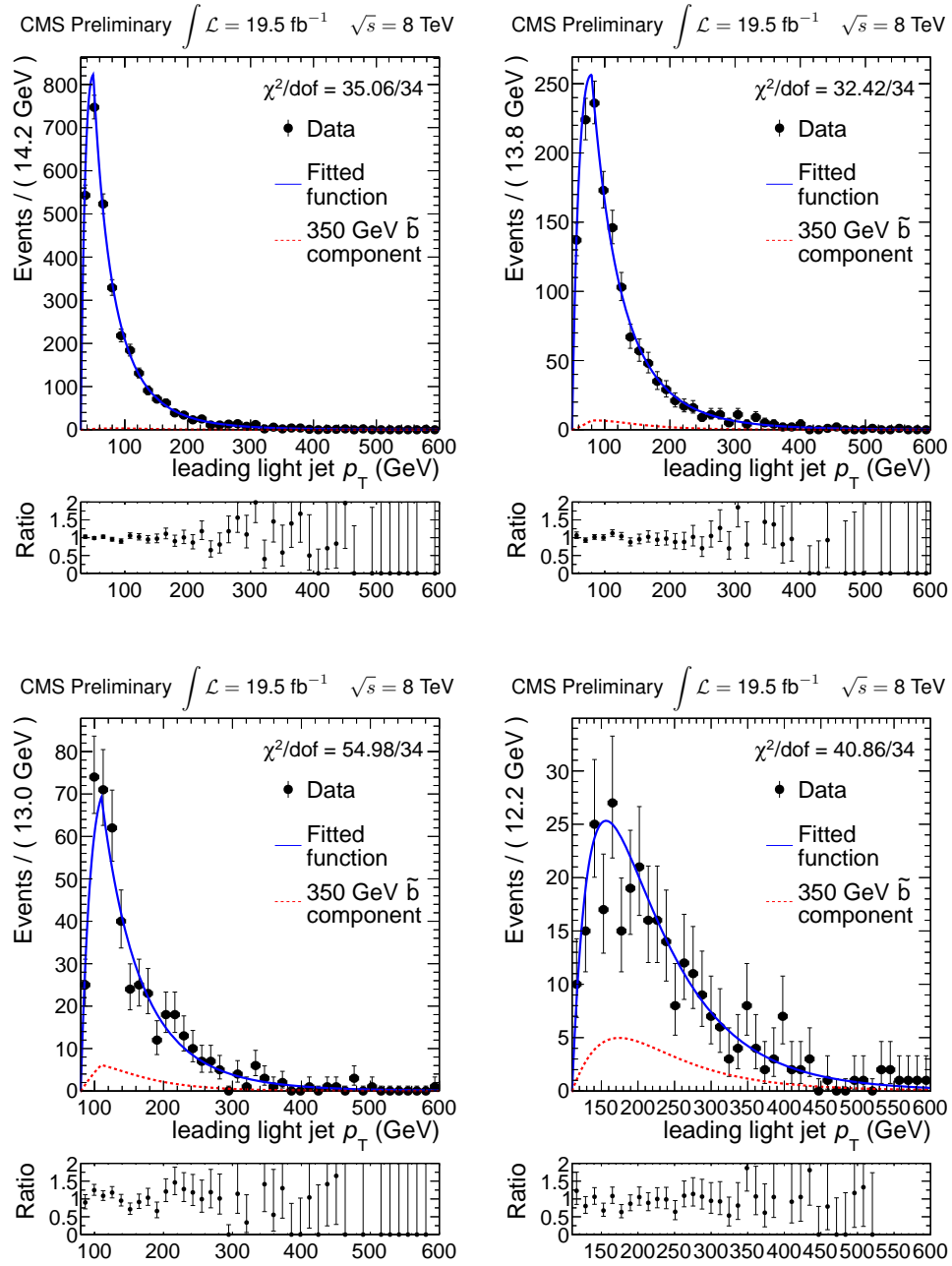


Figure 4.18: Leading light jet  $p_T$  distributions for results of the likelihood maximization with signal cross section set to the 350 GeV  $\tilde{b}$  upper limit. The solid line shows the fitted function, the dashed line shows the signal component, and the points show the data. From left to right, these are for the CR, SR1, SR2, and SR3 regions.

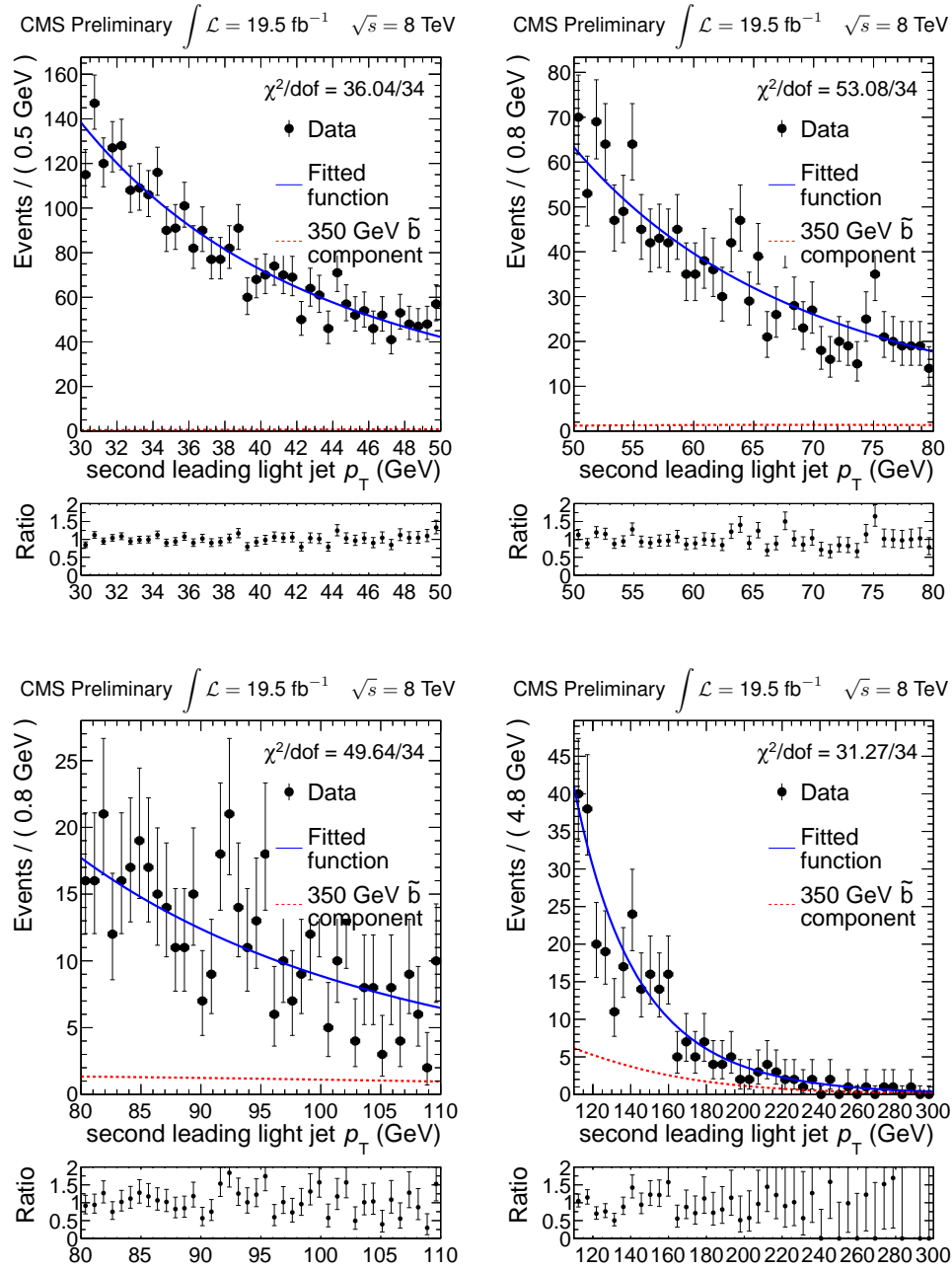


Figure 4.19: Second leading light jet  $p_T$  distributions for results of the likelihood maximization with signal cross section set to the  $350 \text{ GeV } b\tilde{b}$  upper limit. The solid line shows the fitted function, the dashed line shows the signal component, and the points show the data. From left to right, these are for the CR, SR1, SR2, and SR3 regions.

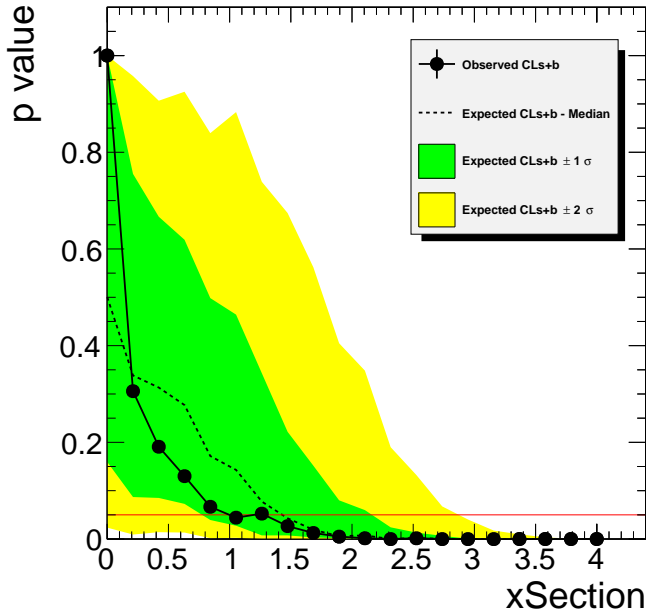


Figure 4.20: Distribution of p-values from the results of the scan over signal cross section hypotheses for the pair production of 350 GeV  $\tilde{b}$  squarks. The vertical axis shows the fraction of toys with a test statistic (the profile likelihood ratio) value greater than that observed in data, as a function of the cross section hypothesis. Black points show the results for toys generated with the signal-plus-background hypothesis, while the dashed line shows results for toys generated using the background-only hypothesis. The green (yellow) band represents the fraction of background-only toys with a best-fit signal cross section within  $\pm 1$  ( $\pm 2$ ) standard deviations of the median value of the cross section corresponding to the global maximum of the likelihood, evaluated on the set of toys generated with the background-only hypothesis. The observed (expected) upper limit on the cross section for this mass point is found as the intersection of the observed (expected) curve with the red horizontal line at 5%, corresponding to a 95% CL.

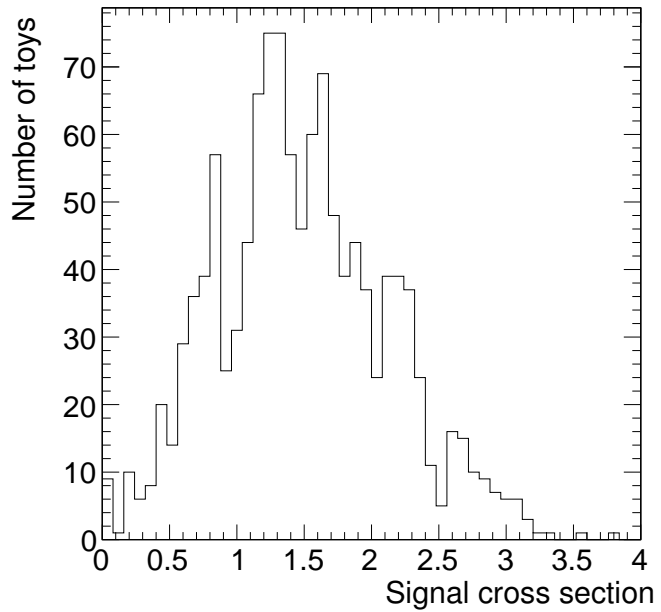


Figure 4.21: Histogram of the signal cross section for the pair production of 350 GeV  $\tilde{b}$  squarks corresponding to the global maximum of the likelihood evaluated on the set of toys generated with the background-only hypothesis. The horizontal axis corresponds to the signal cross section and the vertical axis shows the number of toys. The expected upper limit for this mass point is the median value in the histogram. The 68% (95%) CL band on the expected limit is determined by calculating the values of the best-fit signal cross section at which the fraction of toys below and above the median value corresponds to  $\pm 1$  (2) standard deviations.

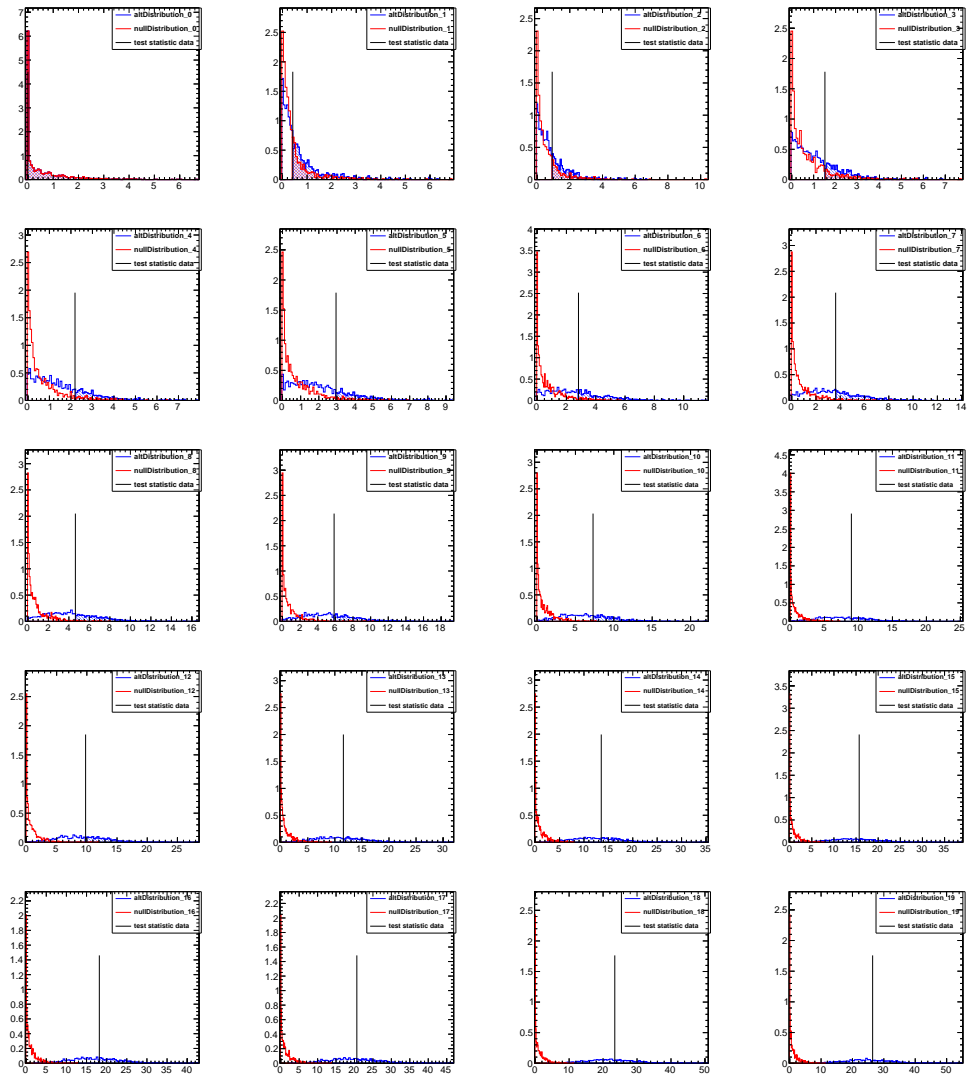


Figure 4.22: Profile likelihood ratio distributions for pseudo-data toy experiments in each signal strength scan point for the 350 GeV  $b$  squark model. Top left scan point corresponds to a cross section of zero and increases from left to right and top to bottom, with the bottom right being the maximum cross section. In red is the test statistic distribution constructed from toys generated using the signal-plus-background hypothesis and in blue is the distribution from toys generated with the background-only hypothesis. The vertical black line marks the value of the profile likelihood ratio evaluated in data for the particular signal strength hypothesis.

## CHAPTER 5

## CONCLUSION

We presented a search for pair-produced new physics resonances decaying into a top quark and light parton, in final states with two leptons. We used  $19.5\text{ fb}^{-1}$  of data collected by the CMS experiment at the LHC during proton-proton collisions at 8 TeV. We selected events with at least two leptons ( $e$  or  $\mu$ ), two b-tagged jets and two non-b-tagged jets. We employed a kinematic method to reconstruct pairs of potential resonant decays. We performed an extended unbinned maximum likelihood fit to the shapes of the reconstructed resonance mass and the leading and second leading light jet transverse momenta in data, and observed results consistent with the standard model. We set upper limits on the pair production cross section of  $R$ -parity violating bottom squarks for masses between 250 and 600 GeV. We excluded  $R$ -parity violating bottom squarks at the 95% confidence level between 250 and 326 GeV.

This constitutes the first LHC result on bottom squarks in the context of the  $R$ -parity violating minimal supersymmetric model constrained to have minimal flavor violation. While other searches inspired by this model have been carried out at the LHC, they have generally focused on different particles and decay modes, such as  $\tilde{g} \rightarrow \tilde{t}\bar{b}\bar{s}$  or  $\tilde{t} \rightarrow \bar{b}\bar{s}$ . The results of the CMS searches are expected to be combined with the above  $\tilde{b}$  results and published in one legacy paper on  $R$ -parity violating supersymmetry searches at CMS with Run I data. There is currently one ongoing search in CMS for  $\tilde{b}$  squarks in the context of a different  $R$ -parity violating supersymmetric model, in which baryon number violation is assumed [81].

We found that our result is limited by statistics and therefore look forward

to Run II of the LHC, during which a minimum of  $100\text{ fb}^{-1}$  of data are expected to be collected at a center-of-mass energy of 13 TeV. In addition to performing the analysis on a larger dataset, we expect that a significant improvement will come from employing a different strategy to reconstruct neutrinos in top quark decays. We investigated a promising method that is applicable to this analysis, as well as different types of measurements in events containing top quarks, such as  $W^\pm$  helicity from top quark decay,  $t\bar{t}$  charge asymmetry, or  $t\bar{t}$  production in association with a Higgs boson. This technique will be documented in a forthcoming publication in the Journal of Nuclear Instruments and Methods.

APPENDIX A  
**OBJECT RECONSTRUCTION IN COLLIDER EVENTS WITH TOP  
QUARKS**

## A.1 Introduction

### A.1.1 Motivation

We described in Section 4.4.2 a method to analytically reconstruct the four-momenta of neutrinos in fully leptonic top quark pair decays by solving a quartic equation, thus allowing for the reconstruction of the top quark four-momenta [67]. The inputs are the measured leptons and b-quark jets, the measured  $E_T^{\text{miss}}$ , and the top quark and  $W^\pm$  boson masses. In order to circumvent the issue of non-physical solutions, the remaining jets in the event are sampled within their resolutions and smeared in order to account for detector resolution effects.

This technique has been used previously within CMS [69]. It is approximately 80% efficient in  $t\bar{t}$  MC simulation. In the remaining fraction of events, jet sampling is not able to recover the “true” top quark pair system, and the method fails. Since the results presented in Section 4.7 are statistics-limited, we developed a method that guarantees solutions. It extends the tools described in Ref. [82] to include uncertainties on all objects in the event. The method will be useful for the analysis of collider events containing top quarks.

### A.1.2 Outline of the strategy

Top quarks overwhelmingly decay to a b quark and  $W^\pm$  boson. In the hadronic decay channel the  $W^\pm$  boson produces a quark-antiquark pair, while in the leptonic channel a lepton and neutrino are produced; in each case the final state contains three objects. Although we focus on the leptonic channel, the method is also applicable to hadronic top decays.

Neutrinos are extremely weakly interacting and escape the detector, resulting at a hadron collider in an observed momentum imbalance in the plane transverse to the beam direction. Conservation of momentum and energy constrain the momentum of a neutrino originating from a leptonic top quark decay to the intersection of two ellipsoids [82], i.e., an ellipse. The parameters of this ellipse are functions of the measured lepton and b-quark jet four-momenta, and the assumed top quark and  $W^\pm$  boson masses.

In the case of top quark pair production there are two neutrinos in the final state, each constrained to its own ellipse. Assuming the entire amount of  $E_T^{\text{miss}}$  is due to the pair of neutrinos, the neutrino momenta can be further constrained to the intersection points of the two neutrino ellipses. There can be zero, two, or four such intersections, at which points the summed neutrinos are exactly consistent with the observed  $E_T^{\text{miss}}$ . Thus we recover the solution multiplicity of the method described in Section 4.4.2, which is that of a quartic equation. In fact the solutions found by this method correspond to the solutions of the quartic equation. The intersection points of two ellipses can be calculated numerically.

If no intersections exist, we assume experimental mismeasurements are responsible. We extend the above framework to include uncertainties on all ob-

jects other than the leptons and b-quark jets. We allow the objects to vary within their uncertainties, and minimize a  $\chi^2$  variable that corresponds to an object configuration leading to intersecting neutrino ellipses. The minimum of the  $\chi^2$  can be solved analytically.

Finally we construct a per-event  $\chi^2$  variable as the sum of the above light jet  $\chi^2$  as well as a  $\chi^2$  combining uncertainties on the b-quark jets, the top quark mass, and the  $W^\pm$  mass. At CMS the uncertainties on leptons ( $e$  or  $\mu$ ) are small compared to uncertainties on jets. These are therefore neglected in our framework, but can be easily introduced. We minimize the per-event  $\chi^2$  numerically.

## A.2 Details of the algorithm

### A.2.1 Neutrino ellipse construction

The first step in the algorithm is to calculate the ellipse constraining the momentum of a neutrino. For this we rely on the solution provided in Ref. [82]. We reproduce here some key results.

#### A.2.1.1 Definitions

We consider the decay chain in which a top quark  $t$  decays to a  $b$  quark and  $W$  boson, and the  $W$  boson decays leptonically to a lepton  $\ell$  and a neutrino  $\nu$ . In the laboratory frame the four-momentum of particle  $i$  is written  $(\mathbf{p}_i, E_i)$ ;  $\phi_i$  and  $\theta_i$  denote the particle's azimuthal and polar angles, respectively. The world average measured values [14] for the top quark,  $b$  quark,  $W^\pm$  boson, lepton, and

neutrino masses are assumed. Conservation of four-momentum constrains  $\mathbf{p}_b$  and  $\mathbf{p}_\ell$  each to a surface that limits on an ellipsoid, the three-dimensional equivalent of an ellipse, in the relativistic limit for the each particle;  $\mathbf{p}_W$  is constrained to the intersection of these two surfaces.

In the laboratory frame, the coordinate system in momentum space  $F\{\tilde{x}, \tilde{y}, \tilde{z}\}$  ( $F'\{\tilde{x}', \tilde{y}', \tilde{z}'\}$ ) is defined as being oriented along  $\mathbf{p}_\ell$  ( $\mathbf{p}_b$ ), with  $F$  and  $F'$  sharing a common  $\tilde{z}$  axis. A transformation from  $F$  to  $F'$  corresponds to a rotation of angle  $\theta_{b\ell}$ , the angle between  $\mathbf{p}_\ell$  and  $\mathbf{p}_b$ , around the  $\tilde{z}$  axis.

### A.2.1.2 Neutrino solutions

Homogeneous coordinates  $\mathbf{r} = (x \ y \ z \ 1)^T$  may be used to calculate the extended ( $4 \times 4$ ) matrix representation of three-dimensional surfaces such as ellipsoids. In these coordinates, an ellipsoid may be represented by a  $4 \times 4$  symmetric matrix  $A$ , with  $\mathbf{r}^T A \mathbf{r} = 0$ . The ellipsoids for the b quark and lepton may be written as

$$\tilde{A}_b = \begin{pmatrix} 1 - (c\beta_b)^2 & -cs\beta_b^2 & 0 & c\tilde{x}_0'\beta_b \\ -cs\beta_b^2 & 1 - (s\beta_b)^2 & 0 & s\tilde{x}_0'\beta_b \\ 0 & 0 & 1 & 0 \\ c\tilde{x}_0'\beta_b & s\tilde{x}_0'\beta_b & 0 & m_W^2 - \tilde{x}_0'^2 \end{pmatrix}, \quad (\text{A.1a})$$

$$\tilde{A}_\mu = \begin{pmatrix} \gamma_\mu^{-2} & 0 & 0 & S_{\tilde{x}}\beta_\mu^2 \\ 0 & 1 & 0 & 0 \\ 0 & 0 & 1 & 0 \\ S_{\tilde{x}}\beta_\mu^2 & 0 & 0 & m_W^2 - \tilde{x}_0^2 - \epsilon^2 \end{pmatrix}, \quad (\text{A.1b})$$

where  $\beta_i$  and  $\gamma_i$  are, respectively, the relativistic speed and Lorentz factors for particle  $i$ ,

$$\beta_i \equiv \frac{p_i}{E_i}, \quad \gamma_i^{-1} \equiv \frac{m_i}{E_i} = \sqrt{1 - \beta_i^2},$$

and

$$\tilde{x}'_0 = -\frac{1}{2E_b} (m_t^2 - m_W^2 - m_b^2), \quad (\text{A.2})$$

$$\tilde{x}_0 = -\frac{1}{2E_\mu} (m_W^2 - m_\mu^2 - m_\nu^2), \quad (\text{A.3})$$

$$S_{\tilde{x}} = (\tilde{x}_0 \beta_\mu - p_\mu \gamma_\mu^{-2}) / \beta_\mu^2, \quad (\text{A.4})$$

$$\epsilon^2 = \gamma_\mu^{-2} (m_W^2 - m_\nu^2). \quad (\text{A.5})$$

The W boson momentum is constrained to the ellipse that is the intersection of the ellipsoids  $\tilde{A}_t$  and  $\tilde{A}_b$ . Similarly the neutrino momentum is constrained to an ellipse; in the  $F$  coordinate system it may be parameterized as  $\tilde{\mathbf{p}}_\nu = \tilde{H}\mathbf{t}$ , where

$$\tilde{H} = \begin{pmatrix} Z/\Omega & 0 & \tilde{x}_1 - p_\mu \\ \omega Z/\Omega & 0 & \tilde{y}_1 \\ 0 & Z & 0 \end{pmatrix}, \quad \mathbf{t} = \begin{pmatrix} \cos t \\ \sin t \\ 1 \end{pmatrix}, \quad (\text{A.6})$$

with

$$S_{\tilde{y}} = \frac{1}{s} (\tilde{x}'_0 / \beta_b - c S_{\tilde{x}}), \quad (\text{A.7})$$

$$\omega = \frac{1}{s} \left( \frac{\beta_\mu}{\beta_b} - c \right), \quad (\text{A.8})$$

$$\Omega^2 = \omega^2 + \gamma_\mu^{-2}, \quad (\text{A.9})$$

$$\tilde{x}_1 = S_{\tilde{x}} - (S_{\tilde{x}} + \omega S_{\tilde{y}}) / \Omega^2, \quad (\text{A.10})$$

$$\tilde{y}_1 = S_{\tilde{y}} - (S_{\tilde{x}} + \omega S_{\tilde{y}}) \omega / \Omega^2, \quad (\text{A.11})$$

$$Z^2 = \tilde{x}_1^2 \Omega^2 - (S_{\tilde{y}} - \omega S_{\tilde{x}})^2 - (m_W^2 - \tilde{x}_0^2 - \epsilon^2). \quad (\text{A.12})$$

When the parameter  $t$  varies between 0 and  $2\pi$ , the product  $\tilde{H}\mathbf{t}$  describes an ellipse. Points on this ellipse represent the set of allowed neutrino momenta

that are consistent with a leptonic top quark decay. A point on the ellipse is referred to as a solution.

Determining the allowed neutrino momenta in the laboratory frame necessitates a transformation from the  $F$  coordinate system back to the laboratory coordinate system. Transforming from the laboratory frame to  $F$  requires three successive rotations:

- a rotation of angle  $\phi_\ell$  around the  $z$ -axis in the laboratory frame, yielding  $\mathbf{p}_\ell$  in the  $x' - z'$  plane,
- a rotation of angle  $\theta_\ell - \frac{\pi}{2}$  around the  $y'$ -axis, so that  $\mathbf{p}_\ell$  is along the  $x''$ -axis,
- a rotation of angle  $\alpha = \arg(y_b'' + i z_b'')$  around the  $x''$ -axis, leaving  $\mathbf{p}_b$  in the  $\tilde{x} - \tilde{y}$  plane with  $\tilde{y}_b > 0$ .

Therefore the transformation from  $F$  to the laboratory coordinate system is given by the product of the rotation matrices corresponding to the above rotations,

$$R = R_z(\phi_\ell) R_{y'}\left(\theta_\ell - \frac{\pi}{2}\right) R_{x''}(\alpha). \quad (\text{A.13})$$

The ensemble of neutrino solutions in the laboratory frame is then parameterized as

$$\mathbf{p}_\nu = H \mathbf{t}, \quad H = R \tilde{H}. \quad (\text{A.14})$$

We present below the expressions for the neutrino ellipse in homogeneous coordinates,

$$H_\perp = \begin{pmatrix} H_{11} & H_{12} & H_{13} \\ H_{21} & H_{22} & H_{23} \\ 0 & 0 & 1 \end{pmatrix}, \quad (\text{A.15})$$

and the extended representation,

$$N_\perp = H_\perp^{-T} U H_\perp^{-1}, \quad (\text{A.16})$$

where  $U = \text{diag} \begin{pmatrix} 1 & 1 & -1 \end{pmatrix}$  is the matrix representation of the unit circle.

In homogeneous coordinates, components of the neutrino momentum in the transverse plane are parameterized as

$$\nu_\perp = H_\perp \mathbf{t}, \quad \nu_\perp = (x_\nu \quad y_\nu \quad 1)^T. \quad (\text{A.17})$$

For a given solution  $\nu_\perp$ , corresponding to a specific point on the solution ellipse, the neutrino momentum is

$$\mathbf{p}_\nu = H H_\perp^{-1} \nu_\perp. \quad (\text{A.18})$$

### A.2.1.3 Algorithm implementation

The construction of the solution ellipse for neutrino momenta is performed in a C++ class, `NeutrinoEllipseCalculator`. We implement methods to calculate the homogeneous and extended matrices of the solution ellipse. Note that the calculation fails when the parameter  $Z^2$  is non-positive. In the case of  $Z^2 = 0$ , the neutrino ellipse is trivially reduced to a point; the case  $Z^2 < 0$  is unphysical in the sense that there is no neutrino momentum consistent with the initial assumption of a top quark undergoing a leptonic decay.

We note that  $Z^2 = 0$  is quartic in  $E_b$ , demonstrating the equivalence between the reconstruction method presented in Ref. [82] and the one described in Section 4.4.2.1. In the latter method, the lack of physical solutions was ascribed to detector resolution effects. The jet resampling technique was introduced in order to circumvent these effects.

The same methodology can be applied here. We determine the b-quark jet four-momenta that yield  $Z^2 > 0$ . Since  $Z^2 = 0$  is quartic, the roots can be determined numerically. Given the possibility of multiple allowed ranges in  $E_b$  that yield  $Z^2 > 0$ , we select the one either containing the measured value, or closest to it as measured by the logarithm of the ratio of corrected energy to reconstructed energy.

Inputs for the `NeutrinoEllipseCalculator` constructor are simply the measured four-momenta of a b-quark jet and lepton, and the resolution on the jet. From these we are able to numerically determine solutions for the neutrino momentum under the assumption of a leptonic top quark decay, and the range of corrections to the b-quark jet  $p_T$  and energy that guarantee physical solutions for the neutrino momentum.

## A.2.2 Light jet minimization

### A.2.2.1 Missing transverse energy constraint

In a collider event containing a pair of top quarks that both decay leptonically,  $t \rightarrow b\ell^+\nu$  and  $\bar{t} \rightarrow \bar{b}\ell^-\bar{\nu}$ , assume the longitudinal momentum of the  $t\bar{t}$  system is unconstrained. This is the case at hadron colliders. We apply the above procedure to construct the ellipse of solutions for both neutrino momenta. In the extended matrix representation the transverse momenta of the neutrinos verify

$$\nu_\perp^T N_\perp \nu_\perp = 0, \quad \bar{\nu}_\perp^T \bar{N}_\perp \bar{\nu}_\perp = 0. \quad (\text{A.19})$$

Assuming that the entire amount of  $E_T^{\text{miss}}$  in the event is due to the pair of neutrinos, an additional constraint may be applied such that the sum of the neu-

trino components in the transverse plane equal the measured  $E_T^{\text{miss}}$  components ( $x$ ,  $y$ ). This constraint may be written in matrix form as

$$\bar{\nu}_\perp = \Gamma \nu_\perp, \quad \Gamma = \begin{pmatrix} -1 & 0 & x \\ 0 & -1 & y \\ 0 & 0 & 1 \end{pmatrix}, \quad (\text{A.20})$$

where  $\Gamma^{-1} = \Gamma$ .

Thus the extended representation  $\bar{\nu}_\perp$  may be expressed in terms of  $\nu_\perp$ ,

$$\nu_\perp^T \bar{N}'_\perp \nu_\perp = 0, \quad \bar{N}'_\perp = \Gamma^T \bar{N}_\perp \Gamma, \quad (\text{A.21})$$

meaning that the neutrino and anti-neutrino momenta that are consistent with a fully leptonic top quark pair decay, and whose sum in the transverse plane is constrained to the  $E_T^{\text{miss}}$ , correspond to the intersections of the two neutrino ellipses. Excluding tangencies there may be zero, two, or four such solutions, which may be calculated numerically. We have verified that these solutions are identical to those obtained following the quartic equation method described in Ref. [67].

We now focus on the case of non-intersecting ellipses. At this point in Section 4.4.2, sampling over jet resolutions was introduced. We extend the idea to this framework by requiring that objects in the event other than the top quark decay products account for the difference between the neutrino solution components and the measured  $E_T^{\text{miss}}$ . This means varying the corresponding objects within their uncertainties in order to shift the distance between the centers of the neutrino ellipses and thus force them to intersect.

### A.2.2.2 Per-object $\chi^2$

At hadron colliders such as the LHC the objects that are not associated with the top quark decays are typically light-flavor jets. The method described below can however be extended to any type of reconstructed object, given its four-momentum and assumed resolution. With this information, we can construct a per-object  $\chi^2$  representing the degree of belief in a true object hypothesis,

$$\chi^2 = \sum_i \left( \frac{\delta_i}{\sigma_i} \right)^2,$$

where  $\delta_i$  is the correction with respect to the measured object component in the  $i^{\text{th}}$  direction,  $\sigma_i$  is the corresponding resolution, and the sum runs over independent directions in a chosen basis. This assumes the uncertainties on are uncorrelated across directions in this basis.

It is possible to work in the two-dimensional transverse basis, or the full three-dimensional basis. We present below the calculation in the three-dimensional basis; the two-dimensional case is treated analogously. Although resolutions at hadron colliders are generally measured in radial coordinates  $p_{\text{T}}$ ,  $\eta$  and  $\phi$ , leading to

$$\chi^2_{\text{radial}} = \left( \frac{\delta_{p_{\text{T}}}}{\sigma_{p_{\text{T}}}} \right)^2 + \left( \frac{\delta_\eta}{\sigma_\eta} \right)^2 + \left( \frac{\delta_\phi}{\sigma_\phi} \right)^2,$$

we wish to work in the Cartesian basis, in which the  $E_{\text{T}}^{\text{miss}}$  constraint is most naturally written. Another advantage is that the minimum  $\chi^2$ , corresponding to the most likely true object, may be calculated analytically as we will soon show.

We define  $\boldsymbol{\delta} = (\delta_{p_x} \quad \delta_{p_y} \quad \delta_{p_z})$ , representing the vector of corrections to each

component of the three-momentum of an object, and the covariance matrix

$$\Sigma = \begin{pmatrix} \sigma_x^2 & \sigma_{xy} & \sigma_{xz} \\ \sigma_{xy} & \sigma_y^2 & \sigma_{yz} \\ \sigma_{xz} & \sigma_{yz} & \sigma_z^2 \end{pmatrix}.$$

The per-object  $\chi^2$  in the Cartesian basis is then written

$$\chi_{\text{cartesian}}^2 = (\boldsymbol{\delta}) \left( \Sigma^{-1} \right) (\boldsymbol{\delta})^T \quad (\text{A.22})$$

The elements of the covariance matrix may be calculated assuming the following forms for the corrections:

$$p_x = p_T \exp(\delta_{p_T}) \cos(\phi + \delta_\phi) \quad (\text{A.23})$$

$$p_y = p_T \exp(\delta_{p_T}) \sin(\phi + \delta_\phi) \quad (\text{A.24})$$

$$p_z = p_T \exp(\delta_{p_T}) \sinh(\eta + \delta_\eta), \quad (\text{A.25})$$

and assuming each resolution parameter follows a normal distribution,

$$\rho(\delta_{p_T}) = \frac{1}{\sigma_{p_T} \sqrt{2\pi}} \exp\left(-\frac{1}{2}\left(\frac{\delta_{p_T}}{\sigma_{p_T}}\right)^2\right), \quad (\text{A.26})$$

$$\rho(\delta_\phi) = \frac{1}{\sigma_\phi \sqrt{2\pi}} \exp\left(-\frac{1}{2}\left(\frac{\delta_\phi}{\sigma_\phi}\right)^2\right), \quad (\text{A.27})$$

$$\rho(\delta_\eta) = \frac{1}{\sigma_\eta \sqrt{2\pi}} \exp\left(-\frac{1}{2}\left(\frac{\delta_\eta}{\sigma_\eta}\right)^2\right). \quad (\text{A.28})$$

Thus

$$\begin{aligned} (\sigma_x)^2 &= \langle (p_x)^2 \rangle - \langle p_x \rangle^2 \\ (\sigma_x)^2 &= \int_{-\infty}^{\infty} \int_{-\infty}^{\infty} (p_T \exp(\delta_{p_T}) \cos(\phi + \delta_\phi))^2 \rho(\delta_{p_T}) d\delta_{p_T} \rho(\delta_\phi) d\delta_\phi \\ &\quad - \left( \int_{-\infty}^{\infty} \int_{-\infty}^{\infty} (p_T \exp(\delta_{p_T}) \cos(\phi + \delta_\phi)) \rho(\delta_{p_T}) d\delta_{p_T} \rho(\delta_\phi) d\delta_\phi \right)^2 \end{aligned}$$

$$\begin{aligned}
(\sigma_y)^2 &= \langle (p_y)^2 \rangle - \langle p_x \rangle^2 \\
(\sigma_y)^2 &= \int_{-\infty}^{\infty} \int_{-\infty}^{\infty} (p_T \exp(\delta_{p_T}) \sin(\phi + \delta_\phi))^2 \rho(\delta_{p_T}) d\delta_{p_T} \rho(\delta_\phi) d\delta_\phi \\
&\quad - \left( \int_{-\infty}^{\infty} \int_{-\infty}^{\infty} (p_T \exp(\delta_{p_T}) \sin(\phi + \delta_\phi)) \rho(\delta_{p_T}) d\delta_{p_T} \rho(\delta_\phi) d\delta_\phi \right)^2
\end{aligned}$$

$$\begin{aligned}
(\sigma_z)^2 &= \langle (p_z)^2 \rangle - \langle p_z \rangle^2 \\
(\sigma_z)^2 &= \int_{-\infty}^{\infty} \int_{-\infty}^{\infty} (p_T \exp(\delta_{p_T}) \sinh(\eta + \delta_\eta))^2 \rho(\delta_{p_T}) d\delta_{p_T} \rho(\delta_\eta) d\delta_\eta \\
&\quad - \left( \int_{-\infty}^{\infty} \int_{-\infty}^{\infty} p_T \exp(\delta_{p_T}) \sinh(\eta + \delta_\eta) \rho(\delta_{p_T}) d\delta_{p_T} \rho(\delta_\eta) d\delta_\eta \right)^2
\end{aligned}$$

$$\begin{aligned}
\sigma_{xy} &= \langle p_x p_y \rangle - \langle p_x \rangle \langle p_y \rangle \\
\sigma_{xy} &= \int_{-\infty}^{\infty} \int_{-\infty}^{\infty} (p_T \exp(\delta_{p_T}))^2 \cos(\phi + \delta_\phi) \sin(\phi + \delta_\phi) \rho(\delta_{p_T}) d\delta_{p_T} \rho(\delta_\phi) d\delta_\phi \\
&\quad - \left( \int_{-\infty}^{\infty} \int_{-\infty}^{\infty} (p_T \exp(\delta_{p_T}) \cos(\phi + \delta_\phi)) \rho(\delta_{p_T}) d\delta_{p_T} \rho(\delta_\phi) d\delta_\phi \right) \\
&\quad \times \left( \int_{-\infty}^{\infty} \int_{-\infty}^{\infty} (p_T \exp(\delta_{p_T}) \sin(\phi + \delta_\phi)) \rho(\delta_{p_T}) d\delta_{p_T} \rho(\delta_\phi) d\delta_\phi \right)
\end{aligned}$$

$$\begin{aligned}
\sigma_{xz} &= \langle p_x p_z \rangle - \langle p_x \rangle \langle p_z \rangle \\
\sigma_{xz} &= \int_{-\infty}^{\infty} \int_{-\infty}^{\infty} \int_{-\infty}^{\infty} (p_T \exp(\delta_{p_T}))^2 \cos(\phi + \delta_\phi) \sinh(\eta + \delta_\eta) \rho(\delta_{p_T}) d\delta_{p_T} \rho(\delta_\phi) d\delta_\phi \rho(\delta_\eta) d\delta_\eta \\
&\quad - \left( \int_{-\infty}^{\infty} \int_{-\infty}^{\infty} (p_T \exp(\delta_{p_T}) \cos(\phi + \delta_\phi)) \rho(\delta_{p_T}) d\delta_{p_T} \rho(\delta_\phi) d\delta_\phi \right) \\
&\quad \times \left( \int_{-\infty}^{\infty} \int_{-\infty}^{\infty} p_T \exp(\delta_{p_T}) \sinh(\eta + \delta_\eta) \rho(\delta_{p_T}) d\delta_{p_T} \rho(\delta_\eta) d\delta_\eta \right)
\end{aligned}$$

$$\sigma_{yz} = \langle p_y p_z \rangle - \langle p_y \rangle \langle p_z \rangle$$

$$\begin{aligned}\sigma_{yz} &= \int_{-\infty}^{\infty} \int_{-\infty}^{\infty} \int_{-\infty}^{\infty} (p_T \exp(\delta_{p_T}))^2 \sin(\phi + \delta_\phi) \sinh(\eta + \delta_\eta) \rho(\delta_{p_T}) d\delta_{p_T} \rho(\delta_\phi) d\delta_\phi \rho(\delta_\eta) d\delta_\eta \\ &\quad - \left( \int_{-\infty}^{\infty} \int_{-\infty}^{\infty} (p_T \exp(\delta_{p_T}) \sin(\phi + \delta_\phi)) \rho(\delta_{p_T}) d\delta_{p_T} \rho(\delta_\phi) d\delta_\phi \right) \\ &\quad \times \left( \int_{-\infty}^{\infty} \int_{-\infty}^{\infty} p_T \exp(\delta_{p_T}) \sinh(\eta + \delta_\eta) \rho(\delta_{p_T}) d\delta_{p_T} \rho(\delta_\eta) d\delta_\eta \right)\end{aligned}$$

Finally, computing the integrals leads to

$$\begin{aligned}(\sigma_x)^2 &= \frac{p_T^2 \exp(2\sigma_{p_T}^2)}{2} (1 + \cos(2\phi)(\exp(-2\sigma_\phi^2))) \\ &\quad - \frac{p_T^2 \exp(\sigma_{p_T}^2)}{2} (1 + \cos(2\phi))(\exp(-\sigma_\phi^2))\end{aligned}\tag{A.29}$$

$$\begin{aligned}(\sigma_y)^2 &= \frac{p_T^2 \exp(2\sigma_{p_T}^2)}{2} (1 - \cos(2\phi) \exp(-2\sigma_\phi^2)) \\ &\quad - \frac{p_T^2 \exp(\sigma_{p_T}^2)}{2} (1 - \cos(2\phi))(\exp(-\sigma_\phi^2))\end{aligned}\tag{A.30}$$

$$\begin{aligned}(\sigma_z)^2 &= \frac{p_T^2 \exp(2\sigma_{p_T}^2)}{2} (\exp(-2\sigma_\eta) \cosh(2\eta) - 1) \\ &\quad - p_T^2 \exp(\sigma_{p_T}^2) \sinh^2(\eta) \exp(\sigma_\eta^2)\end{aligned}\tag{A.31}$$

$$\begin{aligned}\sigma_{xy} &= \frac{p_T^2 \exp(2\sigma_{p_T}^2)}{2} \sin(2\phi) \exp(-2\sigma_\phi^2) \\ &\quad - \frac{p_T^2 \exp(\sigma_{p_T}^2)}{2} \sin(2\phi) \exp(-\sigma_\phi^2)\end{aligned}\tag{A.32}$$

$$\begin{aligned}\sigma_{xz} &= p_T^2 \exp(2\sigma_{p_T}^2) \cos(\phi) \sinh(\eta) \exp\left(\frac{\sigma_\eta - \sigma_\phi}{2}\right) \\ &\quad - p_T^2 \exp(\sigma_{p_T}^2) \cos(\phi) \sinh(\eta) \exp\left(\frac{\sigma_\eta^2 - \sigma_\phi^2}{2}\right)\end{aligned}\tag{A.33}$$

$$\begin{aligned}\sigma_{yz} &= p_T^2 \exp(2\sigma_{p_T}^2) \sin(\phi) \sinh(\eta) \exp\left(\frac{\sigma_\eta - \sigma_\phi}{2}\right) \\ &\quad - p_T^2 \exp(\sigma_{p_T}^2) \sin(\phi) \sinh(\eta) \exp\left(\frac{\sigma_\eta^2 - \sigma_\phi^2}{2}\right)\end{aligned}\tag{A.34}$$

### A.2.2.3 Inverting the global covariance matrix with the momentum conservation constraint

Having expressed a per-object  $\chi^2$ , we may now write a per-event  $\chi^2$  that sums the per-object  $\chi^2$  over the objects we wish to correct in order to create intersecting neutrino ellipses. We denote by

$$\boldsymbol{\delta}_i = \begin{pmatrix} \delta_{x,i} & \delta_{y,i} & \delta_{z,i} \end{pmatrix}, \quad \Sigma_i = \begin{pmatrix} \sigma_{x,i}^2 & \sigma_{xy,i} & \sigma_{xz,i} \\ \sigma_{xy,i} & \sigma_{y,i}^2 & \sigma_{yz,i} \\ \sigma_{xz,i} & \sigma_{yz,i} & \sigma_{z,i}^2 \end{pmatrix},$$

the difference between a hypothesized true object and the  $i^{\text{th}}$  reconstructed object, and the covariance matrix for the  $i^{\text{th}}$  object. In this notation the per-object  $\chi^2$  is  $\chi_i^2 = \boldsymbol{\delta}_i \Sigma_i^{-1} \boldsymbol{\delta}_i$ .

Let  $n$  be the number of objects in the event that we wish to correct. We define the vector  $\Delta = (\boldsymbol{\delta}_1 \quad \boldsymbol{\delta}_2 \quad \dots \quad \boldsymbol{\delta}_n)$  and the matrix

$$X = \begin{pmatrix} \Sigma_1^{-1} & 0 & \dots & 0 \\ 0 & \Sigma_2^{-1} & \dots & 0 \\ \vdots & \vdots & \ddots & \vdots \\ 0 & 0 & \dots & \Sigma_n^{-1} \end{pmatrix}. \quad (\text{A.35})$$

The per-event  $\chi^2$  is then given by

$$\chi^2 = \Delta X \Delta^T. \quad (\text{A.36})$$

We now apply the constraint that momentum be conserved. We wish to determine the set of hypothetical true objects that have a sum at some distance  $\mathbf{d} = (d_x \quad d_y \quad d_z)$  from the sum of reconstructed objects that minimizes the total  $\chi^2$ . This requirement may be written in matrix form as  $C\Delta^T = \mathbf{d}$ , having defined the constraint matrix  $C = (I \quad I \quad \dots \quad I)$ .

In order to minimize the  $\chi^2$  with the conservation of momentum constraint, we employ the technique of Lagrange multipliers. We define the Lagrange multipliers  $\lambda = (\lambda_x \ \ \lambda_y \ \ \lambda_z)$ . The minimum  $\chi^2$  corresponds to the stable points of the Lagrangian

$$L(\Delta, \lambda) = \Delta X \Delta^T + \lambda(C \Delta^T - \mathbf{d})^T, \quad (\text{A.37})$$

which may be found by setting its partial derivatives to zero. This may be written as a system of equations that is linear in the  $\delta_i$  parameters,

$$\begin{pmatrix} X & C^T \\ C & 0 \end{pmatrix} \begin{pmatrix} \Delta^T \\ \lambda^T \end{pmatrix} = \begin{pmatrix} \mathbf{0}^T \\ \mathbf{d}^T \end{pmatrix}, \quad (\text{A.38})$$

where  $\mathbf{0}^T$  is the zero vector in three dimensions<sup>1</sup>.

In order to find the solution to the above system of linear equations we must invert the (symmetric) matrix

$$\begin{pmatrix} X & C^T \\ C & 0 \end{pmatrix} = \begin{pmatrix} \Sigma_1^{-1} & 0 & \dots & 0 & I \\ 0 & \Sigma_2^{-1} & \dots & 0 & I \\ \vdots & \vdots & \ddots & \vdots & \vdots \\ 0 & 0 & \dots & \Sigma_n^{-1} & I \\ I & I & \dots & I & 0 \end{pmatrix}.$$

The solution to the system of linear equations defined in Eq. A.38 may then be determined by solving for the matrix such that

$$\begin{pmatrix} A_{1,1} & A_{1,2} & \dots & A_{1,n} & B_1 \\ A_{2,1} & A_{2,2} & \dots & A_{2,n} & B_2 \\ \vdots & \vdots & \ddots & \vdots & \vdots \\ A_{n,1} & A_{n,2} & \dots & A_{n,n} & B_n \\ B_1^T & B_2^T & \dots & B_n^T & D \end{pmatrix} \begin{pmatrix} \Sigma_1^{-1} & 0 & \dots & 0 & I \\ 0 & \Sigma_2^{-1} & \dots & 0 & I \\ \vdots & \vdots & \ddots & \vdots & \vdots \\ 0 & 0 & \dots & \Sigma_n^{-1} & I \\ I & I & \dots & I & 0 \end{pmatrix} = \begin{pmatrix} I & 0 & \dots & 0 & 0 \\ 0 & I & \dots & 0 & 0 \\ \vdots & \vdots & \ddots & \vdots & \vdots \\ 0 & 0 & \dots & I & 0 \\ 0 & 0 & \dots & 0 & I \end{pmatrix}, \quad (\text{A.39})$$

---

<sup>1</sup>Had we carried out the calculation of the  $\chi^2$  in two dimensions, the zero vector would have been scaled appropriately.

The solution to the above system of linear equations is then

$$\begin{pmatrix} A_{1,1} & A_{1,2} & \dots & A_{1,n} & B_1 \\ A_{2,1} & A_{2,2} & \dots & A_{2,n} & B_2 \\ \vdots & \vdots & \ddots & \vdots & \vdots \\ A_{n,1} & A_{n,2} & \dots & A_{n,n} & B_n \\ B_1^T & B_2^T & \dots & B_n^T & D \end{pmatrix} \begin{pmatrix} \mathbf{0}^T \\ \mathbf{0}^T \\ \vdots \\ \mathbf{0}^T \\ \mathbf{d}^T \end{pmatrix} = \begin{pmatrix} B_1 \mathbf{d}^T \\ B_2 \mathbf{d}^T \\ \vdots \\ B_n \mathbf{d}^T \\ D \mathbf{d}^T \end{pmatrix} = \begin{pmatrix} \delta_1^T \\ \delta_2^T \\ \vdots \\ \delta_n^T \\ \lambda^T \end{pmatrix} \quad (\text{A.40})$$

In this form, solutions to this system are determined solely by the  $B_i$  matrices.

We now solve for the  $A_i$ ,  $B_i$ , and  $D$  matrices. We note that due to the symmetric nature of  $\begin{pmatrix} X & C^T \\ C & 0 \end{pmatrix}$ ,  $A_{i,j}^T = A_{j,i}$ . We also have

$$\sum_{i=1}^n B_i^T = I = \sum_{i=1}^n B_i \quad (\text{A.41})$$

$$B_i^T \Sigma_i^{-1} + D = 0 \quad (\text{A.42})$$

And thus

$$B_i^T = -D \Sigma_i \quad (\text{A.43})$$

$$\sum_{i=1}^n B_i^T = \sum_{i=1}^n -D \Sigma_i \quad (\text{A.44})$$

$$I = -D \sum_{i=1}^n \Sigma_i \quad (\text{A.45})$$

$$D = -\left( \sum_{i=1}^n \Sigma_i \right)^{-1} \quad (\text{A.46})$$

$$B_i^T = \left( \sum_{j=1}^n \Sigma_j \right)^{-1} \Sigma_i \quad (\text{A.47})$$

$$B_i = \Sigma_i \left( \sum_{j=1}^n \Sigma_j \right)^{-1} \quad (\text{A.48})$$

As noted earlier, this is all that is needed in order to calculate the minimum value of the per-event  $\chi^2$ . However we also present the solution for the  $A_{i,j}$

matrices below. We have

$$\sum_{i=1}^n B_i^T = I = \sum_{i=1}^n B_i \quad (\text{A.49})$$

$$B_i^T \Sigma_i^{-1} + D = 0. \quad (\text{A.50})$$

Introducing the solutions for the  $B_i$  matrices leads to

$$A_{i,j} = \begin{cases} \Sigma_i - B_i \Sigma_i & \text{if } i = j, \\ -B_j \Sigma_i & \text{if } i \neq j. \end{cases} \quad (\text{A.51})$$

$$A_{i,j} = \begin{cases} \Sigma_i - \Sigma_i (\sum_{k=1}^n \Sigma_k)^{-1} \Sigma_i & \text{if } i = j, \\ -\Sigma_j (\sum_{k=1}^n \Sigma_k)^{-1} \Sigma_i & \text{if } i \neq j. \end{cases} \quad (\text{A.52})$$

Returning to the minimum of the  $\chi^2$ , which corresponds to the solution in Eq. A.40, we find

$$\begin{pmatrix} \mathbf{d}B_1^T & \mathbf{d}B_2^T & \dots & \mathbf{d}B_n^T \end{pmatrix} \begin{pmatrix} \Sigma_1^{-1} & 0 & \dots & 0 \\ 0 & \Sigma_2^{-1} & \dots & 0 \\ \vdots & \vdots & \ddots & \vdots \\ 0 & 0 & \dots & \Sigma_n^{-1} \end{pmatrix} \begin{pmatrix} B_1 \mathbf{d}^T \\ B_2^T \mathbf{d}^T \\ \vdots \\ B_n \mathbf{d}^T \end{pmatrix} = \mathbf{d} \sum_{i=1}^n \left( \left( \sum_{j=1}^n \Sigma_j \right)^{-1} \Sigma_i \left( \sum_{k=1}^n \Sigma_k \right)^{-1} \right) \mathbf{d}^T \quad (\text{A.53})$$

$$\mathbf{d} \sum_{i=1}^n \left( \left( \sum_{j=1}^n \Sigma_j \right)^{-1} \Sigma_i \left( \sum_{k=1}^n \Sigma_k \right)^{-1} \right) \mathbf{d}^T = \mathbf{d} \left( \sum_{j=1}^n \Sigma_j \right)^{-1} \mathbf{d}^T \quad (\text{A.54})$$

The minimum per-event  $\chi^2$  is therefore determined solely by the inverse of the covariance matrix of the sum of all objects, as expected in the approximation of normal resolutions. The corresponding corrections to the different objects are determined in Eq. A.40, using the  $B_i$  matrices found in Eq. A.48.

#### A.2.2.4 Algorithm implementation

We write a `lightJetChiSquareMinimumSolver` class that computes the necessary corrections to the four-momenta of objects other than the decay products of the top quark pairs in order to balance the summed neutrino momenta and the  $E_T^{\text{miss}}$ . The inversion of the covariance matrix is performed using the ROOT class `TDecompBase`.

We focus on corrections to the objects in the two-dimensional transverse plane, since at a hadron collider the momentum constraint is on the two-dimensional  $E_T^{\text{miss}}$  object. The necessary inputs are therefore the  $p_T$  and  $\phi$  coordinates of the light jets, the corresponding per-jet resolutions  $\sigma_{p_T}$  and  $\sigma_\phi$ , and the components of the vector  $\mathbf{d}$ . In practice the latter are set to the difference between the observed  $E_T^{\text{miss}}$  and the sum of the neutrino momenta in the  $x$  and  $y$  directions.

### A.2.3 Per-event $\chi^2$ minimization

Finally we wish to incorporate uncertainties on the b-quark jets, the masses of the top quarks, and the masses of the  $W^\pm$  bosons<sup>2</sup>. We construct a global per-event  $\chi^2$  variable and search for the  $\delta$  values on all the different objects that minimize this  $\chi^2$ . We assume Breit–Wigner widths of 2.0 GeV and 2.09 GeV for the top quark and W boson masses, respectively. An associated error is defined by computing the point on a normal distribution at which the cumulative distribution function has the same value as that of the Breit–Wigner at a given mass. We write the corresponding  $\chi^2$  term  $\chi_{\text{mass}}^2(E_{\text{CM}} | m, \Gamma)$ .

---

<sup>2</sup>Recall that we are neglecting uncertainties on the leptons.

Finally the global  $\chi^2$  is written as

$$\begin{aligned} \chi^2 = & \left( \frac{\delta_{p_T}^b}{\sigma_{p_T}^b} \right)^2 + \left( \frac{\delta_\eta^b}{\sigma_\eta^b} \right)^2 + \left( \frac{\delta_\phi^b}{\sigma_\phi^b} \right)^2 + \left( \frac{\delta_{p_T}^{\bar{b}}}{\sigma_{p_T}^{\bar{b}}} \right)^2 + \left( \frac{\delta_\eta^{\bar{b}}}{\sigma_\eta^{\bar{b}}} \right)^2 + \left( \frac{\delta_\phi^{\bar{b}}}{\sigma_\phi^{\bar{b}}} \right)^2 + \chi_{\text{mass}}^2(E_{\text{CM}}^t | m_t, \Gamma_t) + \\ & \chi_{\text{mass}}^2(E_{\text{CM}}^{W^+} | m_{W^+}, \Gamma_W) + \chi_{\text{mass}}^2(E_{\text{CM}}^{\bar{t}} | m_{\bar{t}}, \Gamma_t) + \chi_{\text{mass}}^2(E_{\text{CM}}^{W^-} | m_{W^-}, \Gamma_W) + \chi_{\text{light jet}}^2. \quad (\text{A.55}) \end{aligned}$$

We take into account the ambiguity in pairing the b-quark jets and leptons to reconstruct the top quark pair by minimizing the  $\chi^2$  for both pairings and selecting the one yielding the lowest minimum  $\chi^2$ . The minimization, implemented in a `topSystemChiSquare` class, proceeds in multiple minimization steps in order to guarantee convergence.

First we find a good starting point for the minimizer by determining the corrections to the b-jet momentum, top quark mass, and W boson mass that yield physical neutrino solutions, for each top quark in the event. This is implemented as a minimization within a minimization. The inner minimization governs the correction to the top quark mass. It considers the  $Z^2$  variable defined in Section A.2.1.2 as quadratic in the top quark mass squared and solves for the ranges in which the top quark mass will yield a physical solution. The outer minimizer runs over corrections to the b-quark jet  $p_T$ ,  $\eta$ , and  $\phi$  coordinates and the W boson mass.

After initializing the  $\delta$  values for the b-quark jet momenta and the masses of the top quarks and  $W^\pm$  bosons using those found by minimizing the above  $\chi^2$ , we turn to minimizing the per-event  $\chi^2$ . This procedure is separated into four nested minimizations. The outermost minimizer has eight variables corresponding to the  $\delta$  parameters on the  $\phi$  and  $\eta$  of the two b-quark jets, the masses of the top quarks, and the masses of the  $W^\pm$  bosons. Nested in this minimizer we perform a minimization over the b-quark jet  $p_T$  parameters. Within this

minimizer is a minimization that serves to define a starting point for the light jet  $\chi^2$  minimization. The innermost minimizer corresponds to the light jet  $\chi^2$  minimization.

The nested minimizations function as follows. Given a set of corrections for the  $\eta$  and  $\phi$  of the b-quark jets, the top quark masses, and the  $W^\pm$  boson masses, we can compute the neutrino ellipses using the corrected values as input. Varying the above parameters and the b-quark jets causes the shapes of the neutrino ellipses to change. Assuming in turn a given set of corrections for the  $p_T$  of the b-quark jets fixes the ellipse parameters and therefore the ellipses themselves. First we check whether these ellipses intersect. If they do the light jet  $\chi^2$  is set to zero and the per-event  $\chi^2$  may be directly computed; otherwise we proceed to determine the corrections to the remaining objects, i.e., the light jets, that force the neutrino ellipses to intersect.

Thus the minimum of the per-event  $\chi^2$  may be written as nested minima. The outer minimization is performed over the unconstrained parameters, i.e., the  $\eta$  and  $\phi$  coordinates of the two b-quark jets, the masses of the top quarks, and the masses of the  $W^\pm$  bosons. For each iteration in this minimization, we determine the allowed ranges for the parameters correcting the  $p_T$  (and the energy) of the b-quark jets that yield physical neutrino solutions. We then use these parameters to minimize the  $\chi^2$  over all objects in the event not associated with the top quark decays. We write this as

$$\chi^2_{\text{minimum}} = \underset{\text{Unconstrained}}{\text{Minimum}} \left( \chi^2_{\text{unconstrained}} + \underset{\text{Constrained}}{\text{Minimum}} \left( \chi^2_{\text{constrained}} + \underset{\text{Light jets}}{\text{Minimum}} (\chi^2_{\text{light jets}}) \right) \right) \quad (\text{A.56})$$

Finally we retrieve the values of the parameters that minimize the total  $\chi^2$ . We use these to correct the four-momenta of all the objects in the event, thus

allowing us to determine the momenta of the assumed neutrinos. The four-momenta of the top quarks may then be computed by combining the neutrinos with the b-quark jets and leptons, in the same manner as in the reconstruction technique described in Section 4.4.2.

### A.3 Results in simulation

The algorithm described in Section A.2 is tested in a sample of top quark pair events generated with MADGRAPH. The exact process generated is  $t\bar{t} + 2$  partons. In order to simulate detector effects we smear jets at the LHE level assuming a 10% resolution in  $p_T$  and a 1% angular resolution. We study the events in which the measured b-quark jets, leptons, and  $E_T^{\text{miss}}$  yield non-intersecting neutrino solution ellipses. In this case the above minimization algorithm is applied in order to find physical neutrino solutions.

We find that the pairing of b-quark jets and leptons that yields the minimum per-event  $\chi^2$  corresponds to the truth-level pairing in approximately 90% of events. Figure A.1 presents the minimum  $\chi^2$  distribution for events in which the correct pairing is used, and when the incorrect pairing is used. We note that in the latter case the distribution is wider and has a longer tail. The minimum  $\chi^2$  variable may therefore be used to correctly identify the b-quark jet and lepton pairing with a high efficiency and low misidentification rate.

Excluding leptons, for each of the generated objects, i.e., the top quarks, b quarks,  $W^\pm$  bosons, and neutrinos, we compare the four-momenta of the generated objects to that of the corrected objects. The corrections are determined by the minimization procedure and define the most likely true object from which

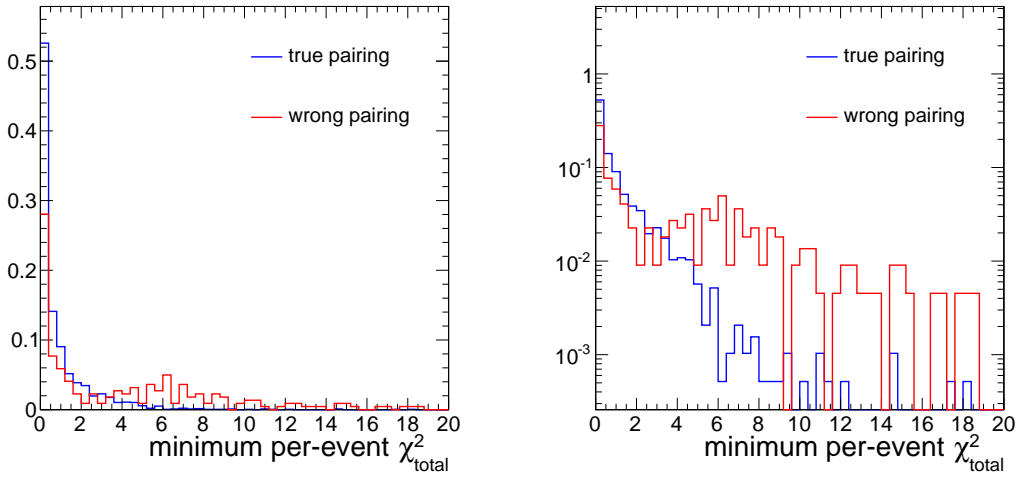


Figure A.1: Minimum per-event  $\chi^2$  distribution in simulated top quark pair events. The blue (red) line corresponds to events in which the b-quark jets and leptons are correctly (incorrectly) paired. Left: linear scale. Right: logarithmic scale.

each reconstructed object may have originated.

We present distributions of the  $p_T$  resolution, defined as the difference between the corrected and generated object  $p_T$  divided by the generated object  $p_T$ , for the neutrinos,  $W^\pm$  bosons, top quarks, and bottom quarks in Figs. A.2, A.4, A.7, and A.10, respectively. The light jet minimization procedure corrects jets in the transverse plane only. Thus we show the distributions of the  $p_x$  and  $p_y$  resolutions for the two light partons in Figs. A.12 and A.13. These distributions are all sharply peaked at zero and steeply falling, demonstrating that the minimization procedure successfully reconstructs objects, with a momentum close to that of the generated object momentum.

Distributions of the angular distance  $\Delta R$  between generated and corrected objects are shown in Figs. A.3, A.6, A.9, and A.11 for neutrinos,  $W^\pm$  bosons, top quarks, and bottom quarks, respectively. The bulk of these distributions

is found to be within  $\Delta R$  of 0.5. We therefore conclude that the minimization procedure achieves excellent angular resolution.

Finally we present in Figs. A.5 and A.8 the resolution on the masses of the top quarks and  $W^\pm$  bosons. We find that the minimization produces corrections resulting in reasonable masses for the top quarks and  $W^\pm$  bosons.

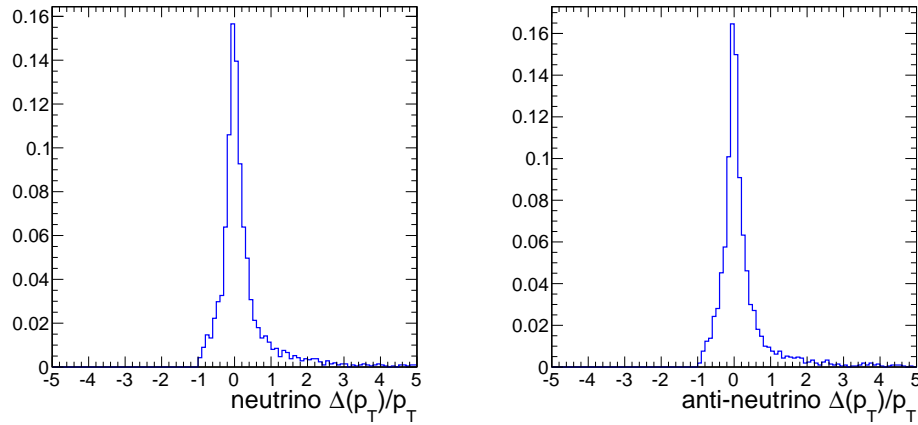


Figure A.2: Distribution of the difference between the corrected and generated neutrino  $p_T$ , normalized to the generated neutrino  $p_T$ . Left: neutrinos; right: anti-neutrinos.

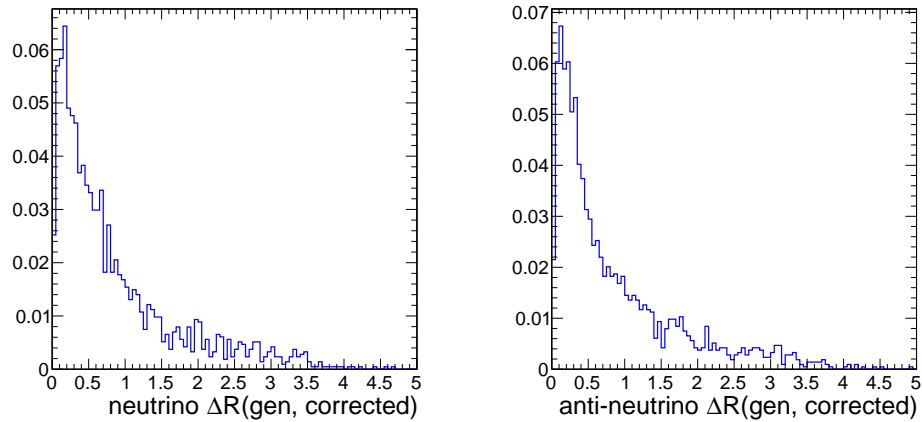


Figure A.3: Distribution of the angular distance between the corrected and generated neutrinos. Left: neutrinos; right: anti-neutrinos.

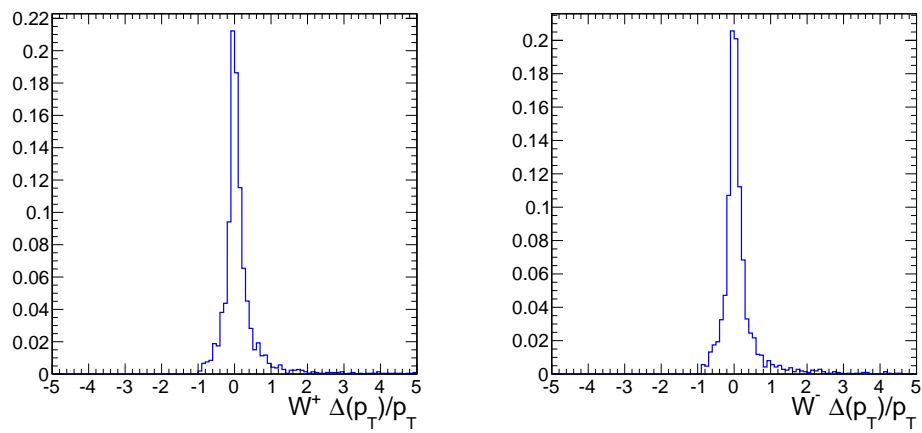


Figure A.4: Distribution of the difference between the corrected and generated  $W^\pm$  boson  $p_T$ , normalized to the generated  $W^\pm$  boson  $p_T$ . Left:  $W^+$  bosons; right:  $W^-$  bosons.

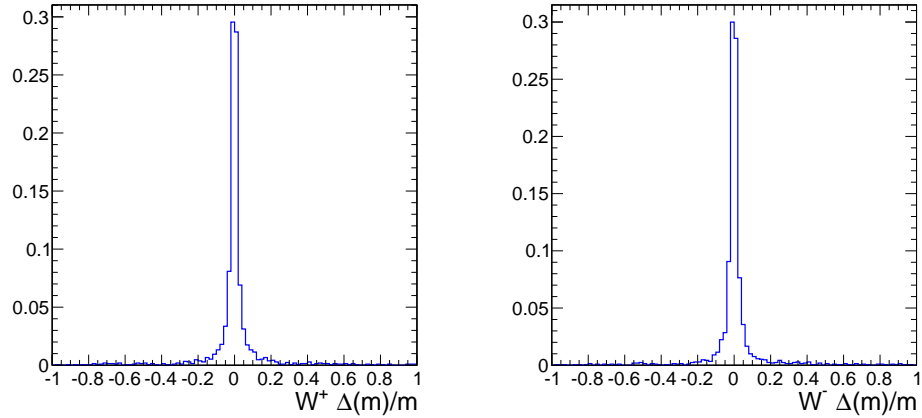


Figure A.5: Distribution of the difference between the corrected and generated  $W^\pm$  boson masses, normalized to the generated  $W^\pm$  boson mass. Left:  $W^+$  bosons; right:  $W^-$  bosons.

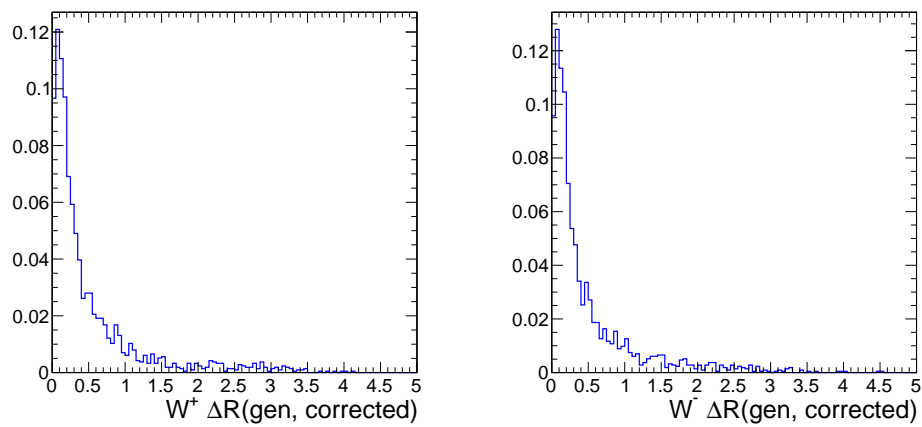


Figure A.6: Distribution of the angular distance between the corrected and generated  $W^\pm$  bosons. Left:  $W^+$  bosons; right:  $W^-$  bosons.

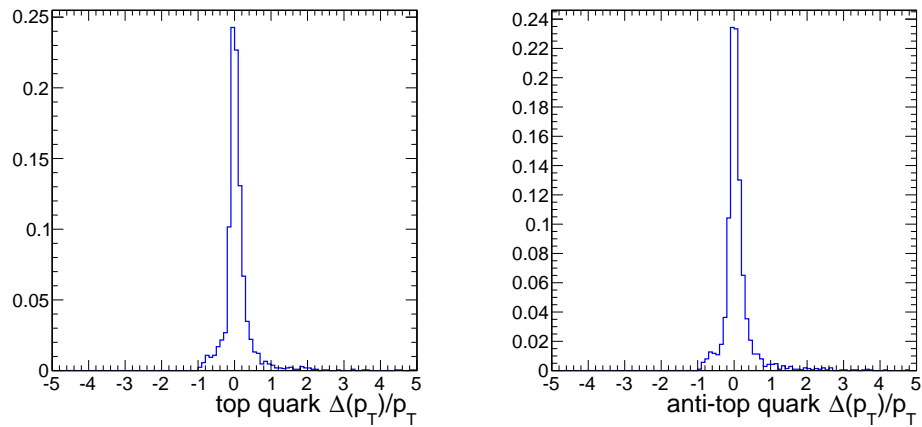


Figure A.7: Distribution of the difference between the corrected and generated top quark  $p_T$ , normalized to the generated top quark  $p_T$ . Left: top quarks; right: anti-top quarks.

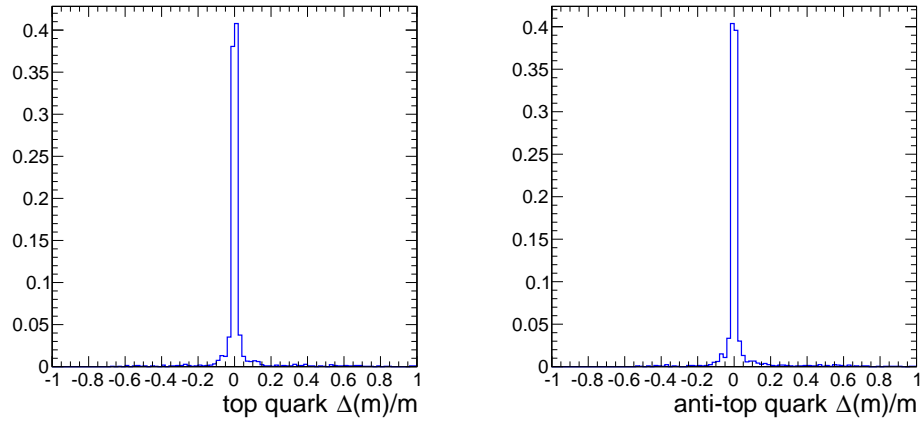


Figure A.8: Distribution of the difference between the corrected and generated top quark masses, normalized to the generated top quark mass. Left: top quarks; right: anti-top quarks.

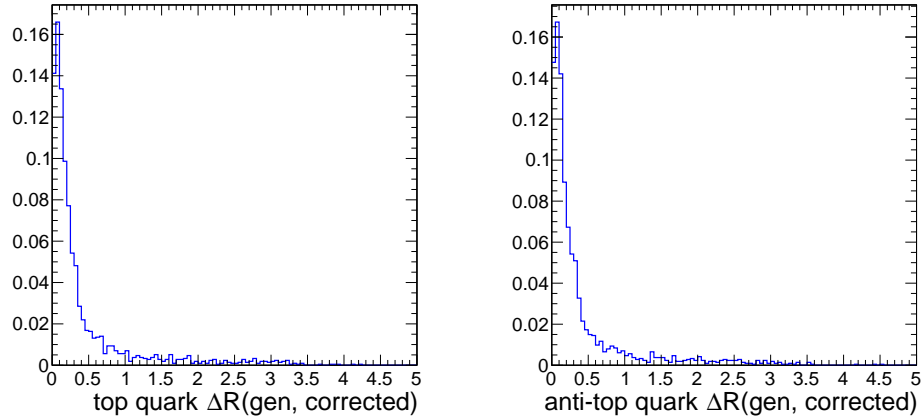


Figure A.9: Distribution of the angular distance between the corrected and generated top quarks. Left: top quarks; right: anti-top quarks.

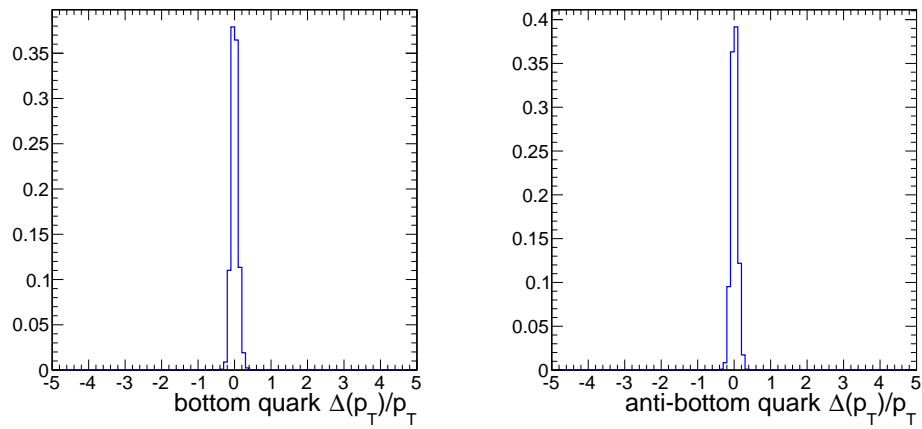


Figure A.10: Distribution of the difference between the corrected and generated bottom quark  $p_T$ , normalized to the generated bottom quark  $p_T$ . Left: bottom quarks; right: anti-bottom quarks.

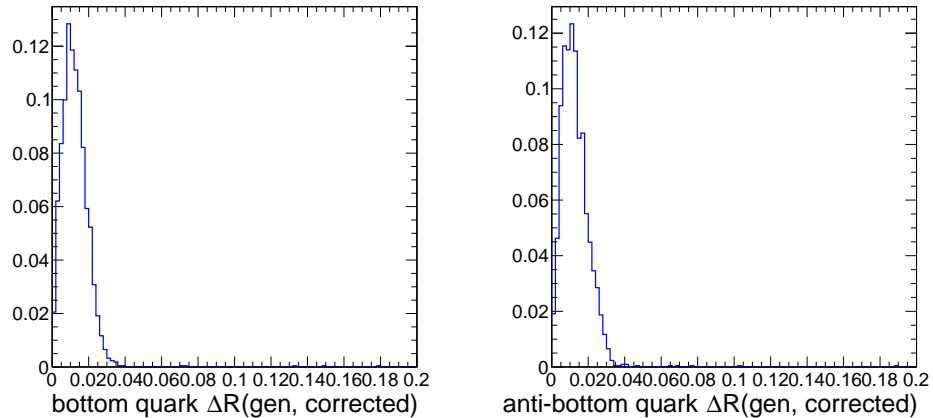


Figure A.11: Distribution of the angular distance between the corrected and generated bottom quarks. Left: bottom quarks; right: anti-bottom quarks.

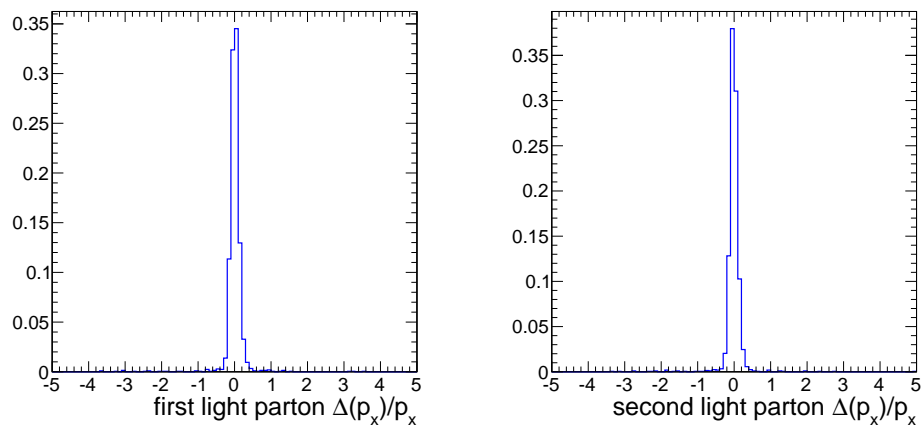


Figure A.12: Distribution of the difference between the corrected and generated light parton  $p_x$ , normalized to the generated light parton  $p_x$ . Left: first generated light partons; right: second generated light partons.

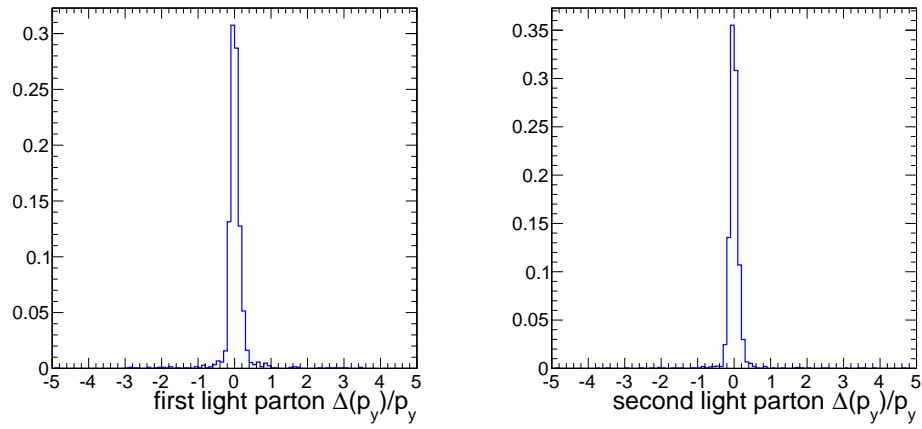


Figure A.13: Distribution of the difference between the corrected and generated light parton  $p_y$ , normalized to the generated light parton  $p_y$ . Left: first generated light partons; right: second generated light partons.

## A.4 Conclusions and outlook

We have presented a method to reconstruct collider events containing top quarks. The method incorporates uncertainties on all objects in the event and performs a  $\chi^2$  minimization in order to determine the most likely hypothetical true objects from which the measured objects may have originated. The algorithm was written in C++ and has been successfully tested on simulated top quark pair events. This method, although originally developed for the purpose of the analysis that is the subject of this thesis, is widely applicable and may be particularly useful to measurements of top quark properties.

## BIBLIOGRAPHY

- [1] **CMS** Collaboration, “Search for pair production of resonances decaying to a top quark plus a jet in final states with two leptons,” Tech. Rep. CMS-PAS-B2G-12-008, CERN, 2013.  
<http://cds.cern.ch/record/1630845>.
- [2] G. Nicolas Kaufman, L. Winstrom, and J. Thom, “Search for pair production of top quark + jet resonances in the dilepton decay channel,” Tech. Rep. CMS-AN-12-280, 2013.
- [3] S. P. Martin, “A Supersymmetry Primer,” arXiv:970935 [hep-ph].
- [4] S. L. Glashow, “Partial-symmetries of weak interactions,” *Nucl. Phys.* **22** (1961) 579.
- [5] S. Weinberg, “A Model of Leptons,” *Phys. Rev. Lett.* **19** (1967) 1264.
- [6] A. Salam, “Weak and electromagnetic interactions,” in *Elementary particle physics: relativistic groups and analyticity*, N. Svartholm, ed., p. 367. Almqvist & Wiksell, 1968. Proceedings of the eighth Nobel symposium.
- [7] C. Csaki, Y. Grossman, and B. Heidenreich, “MFV SUSY: A Natural Theory for R-Parity Violation,” *Phys. Rev. D* **85** (2012) 095009, arXiv:1111.1239 [hep-ph].
- [8] M. Schmaltz, “Electroweak interactions and Higgs phenomenology.”  
<https://indico.cern.ch/event/226365/other-view?view=standard>. Lectures at the 2013 CERN-Fermilab Hadron Collider Physics Summer School.
- [9] H. Logan, “Higgs Bosons Within and Beyond the Standard Model.”  
[http://physicslearning.colorado.edu/tasi/tasi\\_2013/tasi\\_2013.htm](http://physicslearning.colorado.edu/tasi/tasi_2013/tasi_2013.htm). Lectures at the 2013 Theoretical Advanced Study Institute in Elementary Particle Physics.
- [10] **ATLAS** Collaboration, “Observation of a new particle in the search for the Standard Model Higgs boson with the ATLAS detector at the LHC,” *Phys. Lett. B* **716** (2012) 1, arXiv:1207.7214 [hep-exp].

- [11] **CMS** Collaboration, “Observation of a new boson at a mass of 125 GeV with the CMS experiment at the LHC,” *Phys. Lett. B* **716** (2012) 30, arXiv:1207.7235 [hep-exp].
- [12] **ATLAS** Collaboration, “Measurements of Higgs boson production and couplings in diboson final states with the ATLAS detector at the LHC,” *Phys. Lett. B* **726** (2013) 88–119.
- [13] **CMS** Collaboration, “SM Higgs properties using the diphoton channel,” Tech. Rep. CMS-PAS-HIG-13-016, 2013.  
<http://cds.cern.ch/record/1558930>.
- [14] **Particle Data Group** Collaboration, J. Beringer *et al.*, “Review of Particle Physics (RPP),” *Phys. Rev. D* **86** (2012) 010001. And 2013 partial update for the 2014 edition.
- [15] **Super-Kamiokande** Collaboration, “Evidence for oscillations of atmospheric neutrinos,” *Phys. Rev. Lett.* **81** (1998) 1562–1567.
- [16] **SNO** Collaboration, “Measurement of the rate of  $\nu_e + d \rightarrow p + p + e^-$  interactions produced by  $^8\text{B}$  solar neutrinos at the Sudbury Neutrino Observatory,” *Phys. Rev. Lett.* **87** (2001) 071301.
- [17] **KamLAND** Collaboration, “First Results from KamLAND: Evidence for Reactor Antineutrino Disappearance,” *Phys. Rev. Lett.* **90** (2003) 021802.
- [18] M. Papucci, J. T. Ruderman, and A. Weiler, “Natural SUSY endures,” *JHEP* **09** (2012) 035.
- [19] T. Yamanaka, “Third Generation SUSY Searches at the LHC.”  
<http://moriond.in2p3.fr/QCD/2014/WednesdayMorning/Yamanaka.pdf>. Moriond QCD and High Energy Interactions, March 22-29, 2014.
- [20] S. Sekmen, “Inclusive SUSY Searches at the LHC.” <http://moriond.in2p3.fr/QCD/2014/WednesdayMorning/Sekmen.pdf>. Moriond QCD and High Energy Interactions, March 22-29, 2014.
- [21] P. Bargassa, “Strong SUSY production searches at ATLAS and CMS.”  
<https://indico.in2p3.fr/getFile.py/access?contribId=189&sessionId=0&resId=1&materialId=slides&confId=9116>.

Moriond Electroweak Interactions and Unified Theories, March 15-22, 2014.

- [22] M. Flowerdew, “EW SUSY production searches at ATLAS and CMS.” <https://indico.in2p3.fr/getFile.py/access?contribId=169&sessionId=0&resId=0&materialId=slides&confId=9116>. Moriond Electroweak Interactions and Unified Theories, March 15-22, 2014.
- [23] C. Petersson, “Multilepton and Multiphoton signatures of SUSY at the LHC.” <https://indico.in2p3.fr/getFile.py/access?contribId=155&sessionId=0&resId=0&materialId=slides&confId=9116>. Moriond Electroweak Interactions and Unified Theories, March 15-22, 2014.
- [24] R. Barbier, C. Berat, M. Besançon, M. Chemtob, A. Deandrea, *et al.*, “*R*-parity violating supersymmetry,” *Phys. Rept.* **420** (2002) 1–195, arXiv:0406039 [hep-ph].
- [25] M. Lamont, “The LHC machine – present and future.” <https://indico.cern.ch/event/226365/other-view?view=standard>. Lectures at the 2013 CERN-Fermilab Hadron Collider Physics Summer School.
- [26] L. Evans and P. Bryant, “LHC machine,” *JINST* **3** (2008) S08001.
- [27] Forthommel, <http://upload.wikimedia.org/wikipedia/commons/b/ba/Cern-\accelerator-complex.svg>. Used under Creative Commons Attribution-Share Alike 3.0 Unported license.
- [28] CMS Collaboration, “The CMS experiment at the CERN LHC,” *JINST* **3** (2008) S08004.
- [29] CMS Collaboration, “CMS technical design report, volume I: Detector Performance and Software,” Tech. Rep. CERN-LHCC-2006-001, CERN, 2006. [http://cmsdoc.cern.ch/cms/cpt/tdr/ptdr1\\_final\\_colour.pdf](http://cmsdoc.cern.ch/cms/cpt/tdr/ptdr1_final_colour.pdf).
- [30] D. Sprenger *et al.*, “Validation of Kalman Filter alignment algorithm with cosmic-ray data using a CMS silicon strip tracker endcap,” *JINST* **05** (2010) 06007.

- [31] P. Adzicet *et al.*, “Energy resolution of the barrel of the CMS Electromagnetic Calorimeter,” *JINST* **2** (2007) P04004.
- [32] **CMS** Collaboration, “Performance of CMS Hadron Calorimeter Timing and Synchronization using Test Beam, Cosmic Ray, and LHC Beam Data,” *JINST* **5** (2010) T03013.
- [33] S. Abdullin *et al.*, “Design, performance, and calibration of CMS hadron-barrel calorimeter wedges,” *Eur. Phys. J. C* **53** (2008) 139.
- [34] S. Abdullin *et al.*, “Design, performance, and calibration of CMS forward calorimeter wedges,” *Eur. Phys. J. C* **55** (2008) 159.
- [35] **CMS** Collaboration, “The TriDAS Project Technical Design Report, Volume 2: Data Acquisition and High-Level Trigger,” Tech. Rep. CERN-LHCC-2002-026, CERN, 2006.  
<http://cds.cern.ch/record/578006/>.
- [36] **CMS** Collaboration, “Particle-flow event reconstruction in CMS and performance for jets, taus, and  $E_T^{\text{miss}}$ ,” Tech. Rep. CMS-PAS-PFT-09-001, CERN, 2009. <http://cdsweb.cern.ch/record/1194487>.
- [37] **CMS** Collaboration, “Commissioning of the particle-flow event reconstruction with the first LHC collisions recorded in the CMS detector,” Tech. Rep. CMS-PAS-PFT-10-001, CERN, 2010.  
<http://cdsweb.cern.ch/record/1247373>.
- [38] R. Frühwirth, “Application of Kalman filtering to track and vertex fitting,” *Nucl. Instrum. Meth. A* **262** (1987) 444–450.
- [39] Frühwirth, R. and Waltenberger, W. and Vanlaer, P., “Adaptive Vertex Fitting,” *J. Phys. G: Nucl. Part. Phys.* **34** (2007) 343.
- [40] Adam, W. and Frühwirth, R. and Strandlie, A. and Todorov, T., “Reconstruction of electrons with the Gaussian-sum filter in the CMS tracker at the LHC,” *J. Phys. G: Nucl. Part. Phys.* **31** (2005) N9.
- [41] **CMS** Collaboration, “Performance of electron reconstruction and selection with the CMS detector at  $\sqrt{s} = 8 \text{ TeV}$ ,” Tech. Rep. AN-13-399, CERN, Geneva, 2013.

- [42] CMS Collaboration, “Performance of CMS muon reconstruction in pp collisions at  $\sqrt{s} = 7$  TeV,” *JINST* **07** (2012) P10002.
- [43] CMS Collaboration, “Measurements of differential dijet cross section in proton-proton collisions at  $\sqrt{s} = 8$  TeV with the CMS detector,” Tech. Rep. CMS-PAS-SMP-14-002, CERN, 2014.  
<http://cds.cern.ch/record/1709826>.
- [44] CMS Collaboration, CMS Collaboration, “Measurement of the  $t\bar{t}$  production cross section in the dilepton channel in pp collisions at  $\sqrt{s} = 8$  TeV,” *JHEP* **02** (2014) 024, arXiv:1312.7582 [hep-exp].
- [45] M. Cacciari, G. P. Salam, and G. Soyez, “The anti- $k_t$  jet clustering algorithm,” *JHEP* **04** (2008) 063, arXiv:0802.1189 [hep-ex].
- [46] CMS Collaboration, “Determination of jet energy calibration and transverse momentum resolution in CMS,” *JINST* **6** (2011) P11002.
- [47] CMS Collaboration, CMS Collaboration, “Jet energy resolution in cms at  $\sqrt{s} = 7$  TeV,” Tech. Rep. CMS-PAS-JME-10-014, 2010.  
<http://cdsweb.cern.ch/record/1339945>.
- [48] CMS Collaboration, “Missing transverse energy performance of the CMS detector,” *JINST* **6** (2011) P09001.
- [49] CMS Collaboration, S. Chatrchyan *et al.*, “Identification of b-quark jets with the CMS experiment,” *JINST* **8** (2013) P04013, arXiv:1211.4462 [hep-ex].
- [50] CMS Collaboration, “Performance of b-tagging at  $\sqrt{s} = 8$  TeV in multijet,  $t\bar{t}$  and boosted topology events,” Tech. Rep. CMS-PAS-BTV-13-001, CERN, 2013. <http://cds.cern.ch/record/1581306>.
- [51] C. Weiser, “A Combined Secondary Vertex Based B-Tagging Algorithm,” Tech. Rep. CMS-NOTE-06-014, 2006.
- [52] J. Alwall, M. Herquet, F. Maltoni, O. Mattelaer, and T. Stelzer, “MadGraph 5 : Going Beyond,” *JHEP* **1106** (2011) 128, arXiv:1106.0522 [hep-ph].
- [53] S. Frixione, P. Nason, and C. Oleari, “Matching NLO QCD computations

- with Parton Shower simulations: the POWHEG method," *JHEP* **11** (2007) 070.
- [54] A. Was, "TAUOLA the library for  $\tau$  lepton decay, and KKMC/KORALB/KORALZ/... status report," *Nucl. Phys. B – Proceedings Supplements* **98** (2002) 96–102.
- [55] T. Sjöstrand, S. Mrenna, and P. Z. Skands, "PYTHIA 6.4 Physics and Manual," *JHEP* **0605** (2006) 026, arXiv:hep-ph/0603175 [hep-ph].
- [56] <http://feynrules.irmp.ucl.ac.be/wiki/RPVMSM>.
- [57] T. Sjöstrand, S. Mrenna, and P. Z. Skands, "A Brief Introduction to PYTHIA 8.1," *Comput. Phys. Commun.* **178** (2008) 852–867, arXiv:0710.3820 [hep-ph].
- [58] R. Corke and T. Sjöstrand, "Interleaved parton showers and tuning prospects," *JHEP* **03** (2011) 032, arXiv:1011.1759 [hep-ph].
- [59] J. Allison *et al.*, "Geant4 developments and applications," *IEEE Transactions on Nuclear Science* **53** (Feb., 2006) 270–278.
- [60] J. Pumplin *et al.*, "New generation of parton distributions with uncertainties from global QCD analysis," *JHEP* **07** (2002) 012.
- [61] CMS Collaboration, "Properties of the Higgs-like boson in the decay  $H \rightarrow ZZ \rightarrow 4\ell$ ," Tech. Rep. CMS-PAS-HIG-13-002, CERN, 2013. <http://cds.cern.ch/record/1523767>.
- [62] CMS Collaboration, "Performance of muon identification in pp collisions at  $\sqrt{s} = 7$  TeV," Tech. Rep. CMS-PAS-MUO-10-002, CERN, 2010. <http://cdsweb.cern.ch/record/1279140>.
- [63] CMS Collaboration, "Performance of CMS muon reconstruction in pp collision events at  $\sqrt{s} = 7$  TeV." Submitted to *J. Inst.*, 2012.
- [64] CMS Collaboration, "Electron Efficiency Measurements for Top Quark Physics at  $\sqrt{s} = 8$  TeV," Tech. Rep. AN-12-429, CERN, Geneva, 2012.
- [65] Muon reconstruction and isolation scale factors in 2012 data at CMS, <https://twiki.cern.ch/twiki/bin/view/CMS/MuonReferenceEffs>.

- [66] Tools for pile-up reweighting of simulation in 2012 at CMS,  
[https://twiki.cern.ch/twiki/bin/view/CMS/PileupJSONFileforData#Calculating\\_Your\\_Pileup\\_Distribution](https://twiki.cern.ch/twiki/bin/view/CMS/PileupJSONFileforData#Calculating_Your_Pileup_Distribution) and <https://twiki.cern.ch/twiki/bin/viewauth/CMS/PileupMCReweightingUtilities>.
- [67] L. Sonnenschein, “Analytical solution of  $t\bar{t}$  dilepton equations,” *Phys.Rev.* **D73** (2006) 054015, arXiv:hep-ph/0603011 [hep-ph].
- [68] H.-C. Cheng, J. F. Gunion, Z. Han, G. Marandella, and B. McElrath, “Mass determination in SUSY-like events with missing energy,” *JHEP* **0712** (2007) 076, arXiv:0707.0030 [hep-ph].
- [69] **CMS** Collaboration, S. Chatrchyan *et al.*, “Measurement of the top-quark mass in  $t\bar{t}$  events with dilepton final states in  $pp$  collisions at  $\sqrt{s} = 7$  TeV,” *Eur. Phys. J. C* **72** (2012) 2202, arXiv:1209.2393 [hep-ex].
- [70] <https://twiki.cern.ch/twiki/bin/view/CMSPublic/SWGuideJetResolution>.
- [71] **CMS** Collaboration, “Determination of jet energy calibration and transverse momentum resolution in CMS,” *JINST* **06** (Nov., 2011) 11002, arXiv:1107.4277 [physics.ins-det].
- [72] **CMS** Collaboration, “Commissioning of the particle-flow reconstruction in minimum-bias and jet events from  $pp$  collisions at 7 TeV,” Tech. Rep. CMS-PAS-PFT-10-002, 2010.  
<http://cdsweb.cern.ch/record/1279341>.
- [73] **CMS** Collaboration, “Measurement of the top dilepton cross section using b-tagging at  $\sqrt{s} = 7$  TeV with  $882 \text{ pb}^{-1}$  in  $pp$  collisions,” Tech. Rep. CMS-PAS-TOP-12-007, CERN, 2012.  
<http://cdsweb.cern.ch/record/1462235>.
- [74] M. Botje, J. Butterworth, A. Cooper-Sarkar, A. de Roeck, J. Feltesse, *et al.*, “The PDF4LHC Working Group Interim Recommendations,” arXiv:1101.0538 [hep-ph].
- [75] **CMS** Collaboration, “CMS Luminosity Based on Pixel Cluster Counting – Summer 2013 Update,” Tech. Rep. CMS-PAS-LUM-13-001, CERN, Geneva, 2013.

- [76] G. J. Feldman and R. D. Cousins, “Unified approach to the classical statistical analysis of small signals,” *Phys. Rev. D* **57** (Apr., 1998) 3873–3889, [physics/9711021](https://arxiv.org/abs/physics/9711021).
- [77] The LHC Higgs Combination Group, the ATLAS Collaboration, and the CMS Collaboration, “Procedure for the LHC Higgs boson search combination in Summer 2011,” Tech. Rep. ATL-PHYS-PUB-2011-11, CMS-NOTE-2011-005, CERN, Geneva, 2011.  
<http://cds.cern.ch/record/1379837>.
- [78] K. Cranmer, “Statistical Challenges for Searches for New Physics at the LHC,” in *Statistical Problems in Particle Physics, Astrophysics And Cosmology: Proceedings of Phystat05*, L. Lyons, ed., pp. 112–124. Oxford, UK, September 12-15, 2005.
- [79] T. Junk, “Confidence level computation for combining searches with small statistics,” *Nucl. Instrum. Meth. A* **434** (1999) 435–443, [arXiv:hep-ex/9902006](https://arxiv.org/abs/hep-ex/9902006) [hep-ex].
- [80] A. L. Read, “Presentation of search results: the  $CL_s$  technique,” *J Phys. G* **28** (2002) 2693.
- [81] C. Brust, A. Katz, and R. Sundrum, “SUSY stops at a bump,” *JHEP* **08** (2012) 059.
- [82] B. A. Betchart, R. Demina, and A. Harel, “Analytic solutions for neutrino momenta in decay of top quarks,” [arXiv:1305.1878](https://arxiv.org/abs/1305.1878) [hep-ph].